Available online at www.sciencedirect.com

ScienceDirect

Advances in Space Research xxx (xxxx) xxx

ADVANCES IN SPACE RESEARCH (a COSPAR publication)

www.elsevier.com/locate/asr

Recent progress on understanding coronal mass ejection/flare onset by a NASA living with a star focused science team

Mark G. Linton [a,*], Spiro K. Antiochos [b], Graham Barnes [c], Yuhong Fan [d], Yang Liu [e], Benjamin J. Lynch [f], Andrey N. Afanasyev [g,h,i,j], C. Nick Arge [b], Joan Burkepile [d], Mark C.M. Cheung [k], Joel T. Dahlin [l], Marc L. DeRosa [m], Giuliana de Toma [d] C. Richard DeVore [b], George H. Fisher [f], Carl J. Henney [n], Shaela I. Jones [b], Judith T. Karpen [b], Maria D. Kazachenko [h,o], James E. Leake [b], Tibor Török [p], Brian T. Welsch [q]

[a] US Naval Research Laboratory, 4555 Overlook Ave, SW, Washington, DC 20375, USA
[b] Heliophysics Science Division, NASA Goddard Space Flight Center, Greenbelt, MD 20771, USA
[c] NorthWest Research Associates, 3380 Mitchell Ln, Boulder, CO 80301, USA
[d] High Altitude Observatory, National Center for Atmospheric Research, 3080 Center Green Drive, Boulder, CO 80301, USA
[e] Hansen Experimental Physics Laboratory, Stanford University, Stanford, CA 94305-4085, USA
[f] Space Sciences Laboratory, University of California–Berkeley, 7 Gauss Way, Berkeley, CA 94720, USA
[g] Laboratory for Atmospheric and Space Physics, University of Colorado Boulder, 1234 Innovation Drive, Boulder, CO 80303, USA
[h] National Solar Observatory, University of Colorado Boulder, 3665 Discovery Drive, Boulder, CO 80303, USA
[i] Institute of Solar-Terrestrial Physics of SB RAS, Irkutsk, Russia
[j] DKIST Ambassador, USA
[k] CSIRO, Space & Astronomy, PO Box 76, Epping, NSW 1710, Australia
[l] Astronomy Department, University of Maryland, College Park, MD 20742, USA
[m] Lockheed Martin Solar and Astrophysics Laboratory, 3251 Hanover St. B/252, Palo Alto, CA 94304, USA
[n] Air Force Research Laboratory, Space Vehicles Directorate, Kirtland AFB, NM, USA
[o] Department of Astrophysical and Planetary Sciences, University of Colorado Boulder, Boulder, CO 80303, USA
[p] Predictive Science Inc., San Diego, CA 92121, USA
[q] Natural & Applied Sciences, University of Wisconsin–Green Bay, 2420 Nicolet Drive, Green Bay, WI 54311, USA

Received 2 February 2023; received in revised form 24 June 2023; accepted 26 June 2023

Abstract

We present a report of recent progress on the topic of understanding solar coronal mass ejection (CME) onset from both modeling and observational viewpoints, as carried out from 2019 to the present by the NASA Living with a Star Focused Science Topic team on "Understanding the Onset of Major Solar Eruptions." Following the typical Focused Science Topic paradigm, a number of research groups were selected and joined together to tackle this problem. The work being carried out by this team explores the role of topology and of helicity transport in creating an environment favorable to CME eruption and in then providing the energy required for CME onset. The team investigated CME energization and initiation via photospheric shearing, via flux rope formation, and via magnetic flux emergence. This article will highlight recent progress made by six American research groups working in these areas. We do not intend to present an exhaustive review of these topics, but rather summarize the ideas from these research groups regarding ongoing and upcoming challenges to the questions of how, when, and why coronal mass ejections erupt from the sun.

* Corresponding author.
E-mail address: mark.linton@nrl.navy.mil (M.G. Linton).

https://doi.org/10.1016/j.asr.2023.06.045
0273-1177/Published by Elsevier B.V. on behalf of COSPAR.

Please cite this article as: M. G. Linton, S. K. Antiochos, G. Barnes et al., Recent progress on understanding coronal mass ejection/flare onset by a NASA living with a star focused science team, Advances in Space Research, https://doi.org/10.1016/j.asr.2023.06.045

Keywords: Solar corona; Coronal mass ejection; Solar flare

1. Introduction

Understanding the onset of coronal mass ejections is a critical aspect of research necessary for understanding the Sun's effect on Earth's space weather. To tackle this challenging problem, NASA's Living with a Star program put together a Focused Science Topic (FST) team on "Understanding the Onset of Major Solar Eruptions" for the years 2019–2022. The observational expertise of this FST team covered photospheric magnetic field observations and analyses (Liu team), the use of these analyses to infer coronal magnetic topology (Barnes team), and the use of remote sensing analyses to infer properties of erupting CMEs (Lynch team). These teams were paired with modeling teams who studied the energization of the corona via photospheric data driving (Fan team), dynamical flux emergence (Linton team), and imposed photospheric shearing (Antiochos team and Lynch team) to investigate CME onset mechanisms. This article presents the research context in which these CME initiation investigations were undertaken by the team, presents highlights of the research performed on these topics by this team, and concludes with a brief discussion of the outstanding questions which remain for CME research, and recommendations the team offers for advancing this research. This article does not attempt to provide a complete review of the work of the community leading up to this project, as several excellent reviews of the state-of-the-art have recently been published on the topics of CME and flare onset, for example: (Chen, 2011; Green et al., 2018; Patsourakos et al., 2020).

This article is meant to contribute to a series of COSPAR Space Weather Roadmap special issues. The goal of first of these special issues, "Tier 1: Science Research and Applications," is to assess and increase modeling capabilities in space weather. The goal of the second of these special issues, "Tier 2: Achievements and Goals," is to present overviews of the state-of-the-art, advancements, and gaps in understanding of space weather. This article is intended to contribute to the Tier 2 special issue. For reviews of the state of the art and of outlooks for future progress in CME eruption forecasting and in understanding CME propagation through the heliosphere, the reader is pointed to the companion articles in Tier 2: (Georgoulis et al., 2023 and Temmer et al., 2023), respectively.

1.1. Summary of team research results

In Section 2, the Liu team describes a method to improve the vector magnetic field data and an analysis to understand change of magnetic field from major flares in active regions. An intrinsic problem in observed vector magnetic field, the direction (180°) ambiguity in the transverse field, is proposed to be solved with several model-dependent algorithms (e.g., Metcalf et al., 2006). While successful, sometimes the solution of the disambiguation is inconsistent with time, leading to sudden change of the field direction in certain areas from one frame to the next, which is likely incorrect. A new technique is discussed in this section that has been developed to solve this direction flip problem. The section also reports an analysis of 15 CME-associated X-class flares that reveals decreases in helicity and energy fluxes after the flares occur. The decreases are linked to changes of magnetic and velocity fields from the eruptions. Characterizing the changes and the process of buildup of the helicity and energy in these flares provide useful data that help understand solar eruptions.

In Section 3, the Barnes team describes the impact on coronal models of the choice of surface flux transport model used to generate the global photospheric magnetic field map used as a boundary condition. The section demonstrates that the model assumptions and implementation can make a significant difference in the predicted locations of the footpoints of open magnetic flux, in the speed and polarity of the background solar wind, and in what null points are present in the coronal magnetic field. The sensitivity of each of these measures varies with the solar cycle, largely due to the way in which each is impacted by the polar fields, although large, transient differences also result from the assimilation of a new active region. This demonstrates the importance of how the global boundary map is constructed when modeling coronal mass ejections.

In Section 4, the Fan team describes a boundary data-driven magnetohydrodynamic (MHD) simulation of the 2011–02-15 CME event of Active Region 11158. The simulation is driven at the lower boundary with an electric field derived based on the normal magnetic field and the vertical electric current measured from the HMI vector magnetograms. The simulation shows the build-up of a pre-eruption coronal magnetic field with free magnetic energy close to that obtained from the nonlinear force-free field extrapolation just before the onset of the observed X-class flare, and the development of multiple eruptions. The sheared/twisted field lines show morphology in good qualitative agreement with the brightening loops of the SDO/AIA hot channel images. These agreements suggest that the derived electric field is a promising way to drive MHD simulations to establish the force-free pre-eruption coronal field based on the observed vertical electric current and to model its subsequent dynamic loss of equilibrium.

In Section 5, the Linton team reviews the role of flux emergence in energizing and initiating coronal mass ejec-

tions, from both an observational and a numerical point of view. This section then focuses on numerical investigations performed by the team of CME initiation due to the emergence of magnetic flux into the corona. The first series of experiments focuses on convection zone to corona simulations wherein a buoyant convection zone flux rope emerges into a pre-existing coronal potential magnetic arcade. Depending on the relative orientations of the two flux systems, the interaction either generates an erupting breakout flux rope which rises high into the simulation domain, or it generates a stable flux rope which settles into an equilibrium low in the domain. The second series of experiments focuses on the emergence of flux, imposed at the photosphere via electric field boundary driving conditions, into an energized flux rope and arcade system in the corona. In this case, both the relative orientation of the two flux systems and the horizontal distance between the two were investigated. The results showed that both the orientation and distance are critical factors in determining whether an eruption will occur for this setup. Both series of experiments therefore elucidate the key factors which dictate eruptive behavior, and give key insights into what types of observed solar flux emergence configurations should be monitored for their potential eruptive behavior.

The Antiochos team (Section 6) focused on the role of magnetic reconnection in the onset of solar eruptions. Reconnection is widely believed to be the fundamental process underlying a large fraction of solar activity (e.g. Pontin and Priest, 2022). Eruptions exhibit multiple phases, and both observational evidence and theoretical considerations indicate that reconnection may play a key role in each of them. The Antiochos team investigated how reconnection across ubiquitous small-scale coronal current sheets transports magnetic twist toward large-scale polarity inversion lines via the process of *helicity condensation*, and implemented a subgrid-scale physical model called STITCH that streamlines this process in computational studies (Section 6.1). The efficient STITCH model was fully validated against far more intensive, first-principles numerical simulations of helicity condensation (Section 6.2). This new approach was used to calculate and understand the detailed evolution of the large-scale shear field (also known as the reconnection guide field) in a simulation of filament-channel life cycle from formation through eruption (Section 6.3). In addition, the Antiochos team collaborated with the Lynch team (Section 7) on a separate study of an observed mid-latitude filament eruption (Section 7.1). The conclusions of the team's efforts are summarized in Section 6.4.

In Section 7, the Lynch team presents several observational and numerical modeling studies of the larger-scale magnetic reconnection processes associated with CMEs' initiation in the solar corona and their evolution through the inner heliosphere. Magnetic reconnection plays a fundamental role in the physical processes responsible for the origin and evolution of CMEs. Because magnetic flux and magnetic helicity are conserved—even during reconnection—these quantities are of vital importance to the study of CMEs in the corona and heliosphere (e.g. Heyvaerts and Priest, 1984; Berger, 1984; Démoulin et al., 2016). First, Section 7.1 summarizes the Lynch et al., 2021 simulation and analysis of the development of eruptive flare reconnection responsible for the eruption of a mid-latitude filament and the resulting CME. Second, Section 7.2 presents the (Palmerio et al., 2021a and Pal et al., 2022) observational studies of the eruption and evolution of a streamer blowout CME seen by Parker Solar Probe, where magnetic reconnection facilitates a multi-stage, sympathetic eruption sequence and is also responsible for the subsequent erosion of the CME's magnetic flux content during its interaction with the heliospheric current sheet and surrounding solar wind structures. And finally, Section 7.3 reviews the (Lynch et al., 2022) analysis of the application of in situ cylindrical flux rope models for CMEs' coherent magnetic structure to an MHD simulation of a global, streamer-blowout CME in order to evaluate their suitability for quantitative analysis of CME magnetic flux content in current and future Parker Solar Probe observation of CMEs in the $r \lesssim 30 R_{\odot}$ extended corona.

In Section 8, outstanding questions in the field of CME/flare onset are discussed and several recommendations for advancing research into this topic going forward are made. In particular, the questions "Why is understanding eruption onset important?", "What key information are we still missing?", and "How do we make progress?" are discussed.

2. Observed magnetic evolution and X-class flares (Liu team)

Vector magnetograms — maps of the magnetic field vector at the solar photosphere — provide crucial information for understanding many aspects of solar activity, including flares and CMEs, the structure of filaments/prominences that can erupt to form CMEs, mechanisms of coronal heating, and dynamo processes. Magnetic forces ($\mathbf{J} \times \mathbf{B}$) drive flares and CMEs, in the process releasing energy stored in coronal electric currents. Because vector field measurements can be used to identify areas with significant electric currents (by applying Ampère's law or Gauss's separation method [see, e.g., Gauß, 1839; Olsen et al., 2010; Schuck et al., 2022]), magnetograms are key inputs for both observational studies and modeling of the eruption process. Applications include coronal magnetic field extrapolations, discussed in Section 2.2 below, and estimation of photospheric velocity and electric fields, derived from observed magnetic evolution (e.g., Schuck, 2008; Kazachenko et al., 2015). These velocity fields can be used to estimate the flux of magnetic energy (the Poynting flux) and magnetic helicity across the photosphere, which is critical to understand the development of eruptive structures and the energy they store. Data-driven coronal models, like those discussed in Section 4, depend on these magnetic inputs for both coronal initial conditions (inferred by extrapolation) and time-dependent boundary conditions (velocity or electric fields; e.g., Lumme et al., 2019).

For these purposes, high-duty-cycle polarimetric observations by the *Helioseismic and Magnetic Imager* (HMI; Scherrer et al., 2012; Schou et al., 2012 aboard the *Solar Dynamics Observatory* (SDO; Pesnell et al., 2012) are used to produce vector magnetograms at a regular cadence. For details about HMI's vector magnetogram reduction pipeline, see Hoeksema et al. (2014) and Bobra et al. (2014).

This section focuses on two topics related to sequences of observed photospheric vector magnetic fields: Section 2.1 focuses on improving the accuracy of inferred vector magnetic fields by reducing temporal inconsistencies in fields' directions; and Section 2.2 focuses on exploring the evolution in the fluxes of magnetic energy and helicity around the times of solar eruptions.

2.1. Fluctuations in transverse-field azimuths

Polarimetric measurements, by themselves, only determine the line along which the field transverse to the observer's line of sight runs, but not this transverse field's direction. The transverse-field vector, $\mathbf{B}_{\rm trs}$, is therefore subject to a fundamental, 180° ambiguity in direction. Several techniques for resolving this ambiguity have been developed, and the HMI pipeline uses a "simulated annealing" algorithm that minimizes a functional involving the electric current density (see Section 5 of Hoeksema et al., 2014 for details). As of this writing, the pipeline resolves 180° ambiguities separately for each map, independent of the resolution for maps that are adjacent in time. As shown in the top-left panel of Fig. 1, however, there is evidence that ambiguities between some frames are inconsistent – i.e., there is an excess of changes in azimuth near 180° in strong-field pixels, defined here to have $|B_{\rm LOS}|$ >250 G, where $B_{\rm LOS}$ denotes the component of magnetic field along the observer's line of sight. The data shown are from a 32-h series of SHARP magnetograms (Hoeksema et al., 2014; Bobra et al., 2014) for AR 11158, between 2011–02-13 12:00 UT and 2011–02-15 08:00 UT.

Three facts about large-angle azimuth changes should be noted. First (and foremost!), the integrated excess population in the near-180° wings (about 20 kpix) is less than 1% of pixels with $|B_{\rm LOS}|$ >250 G (about 4 $\times 10^6$ pix) – that is, the ambiguity resolution algorithm is consistent in time in more than 99% of cases. Occasionally, however, azimuths within areas of order (10 × 10) pixels can exhibit spurious, frame-to-frame flips (see, e.g., Figure 5 in Welsch et al., 2013 and related discussion). Second, these frequently spurious large-angle flips can occur in strong-field pixels: as shown in the top-right panel of Fig. 1, the population of pixels with $|B_{\rm LOS}|$ >250 G (blue line) has transverse field strengths well separated from the noise in $|B_{\rm trs}|$. As shown in the bottom-left panel of Fig. 1, the bulk of the population of pixels with both $|B_{\rm LOS}|$ >250 G and large frame-to-frame flips ($|\Delta\phi| > 120^\circ$) have field strengths over 150 G (dashed vertical line). Third, in lower-confidence pixels, HMI's vector-field pipeline can *intentionally* randomize the choice of azimuth derived from different methods, which could produce the observed excess in large-angle azimuth changes. Details about ambiguity determination are discussed by Bobra et al. (2014), particularly in tables A.5 and A.6 of their Appendices. However, the criteria for intentional randomization, which mostly deal with weak-field pixels, are irrelevant for almost all of the strong-field pixels analyzed here.

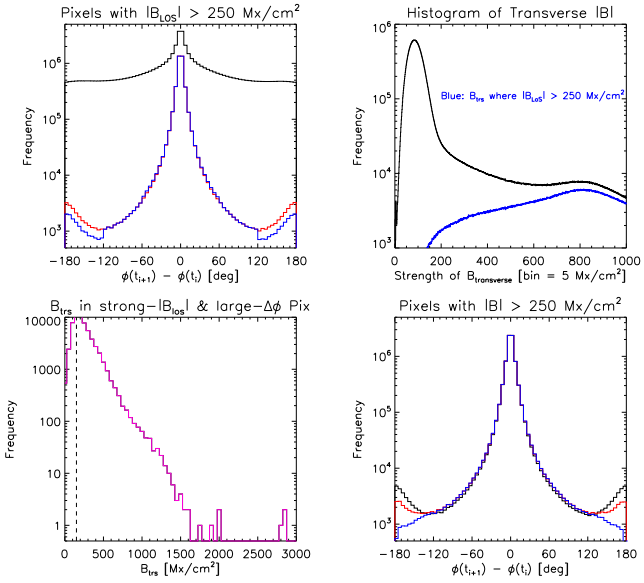

Fig. 1. Top left: Histograms of changes in azimuth between pairs of successive magnetograms from AR 11158 for all pixels (black), strong-field pixels ($|B_{\rm LOS}|$ >250 G) from the HMI pipeline (red), and strong-field pixels after applying a "filtering" approach (blue, Welsch et al., 2013). In strong-field pixels, a clear excess of near-180° fluctuations can be seen, which is partly ameliorated by the filtering. The 120° threshold above which the filtering was applied can also clearly be seen. Top right: Distributions of $|B_{\rm trs}|$ in all pixels (black) and pixels for which $|B_{\rm LOS}|$ >250 G (blue). Bottom left: Distributions of $|B_{\rm trs}|$ in pixels with $|B_{\rm LOS}|$ >250 G that exhibited large changes ($|\Delta\phi| > 120^\circ$) in azimuth. Bottom right: Histograms of azimuth changes in: pixels with $|B| > 250G$ (black); pixels with $|B| > 250G$ after filtering with a linear-weight threshold to reduce the jump at 120° (red); and in pixels with $|B| > 250G$ with filtering applied twice, which removes jumps in azimuth larger than 120° with extreme prejudice (blue).

Resolving inconsistent inferences of azimuth is crucial for employing vector magnetic field observations for the applications described at the start of this section. Spurious changes in transverse fields undermine the accuracy of inferred physical quantities derived from a given measurement of $\left(B_r, B_\theta, B_\phi\right)$, such as the electric currents used in extrapolations and the apparent magnetic evolution used to infer photospheric velocities and electric fields. Even when measurements in some pixels are rated as low-confidence (i.e., in weak-field regions), care must still be taken in assigning transverse-field directions, because random variations in their directions can impact the performance of large-scale models, which require input information at all points at their boundaries.

Observations suggest that fields in many strongly magnetized regions exhibit persistence: they tend to be stable on timescales longer than HMI's nominal, 12-min vector

magnetogram cadence. Also, because any ambiguity resolution algorithm is imperfect, at least some variations in transverse-field directions between successive maps will be unphysical. These considerations motivate incorporating persistence into resolution of 180° ambiguities.

Welsch et al. (2013) implemented a sequential procedure that changes large-angle, transient (back-and-forth) flips in azimuth to minimize azimuth variations in time. Steps used were: (1) identify each pixel with "large" change in azimuth, $\Delta\phi$, from the previous frame; (2) for each large-$|\Delta\phi|$ pixel, compute the average of changes in azimuths with and without flipping each pixel's azimuth, $\overline{\Delta\phi}_{\rm flip}$ and $\overline{\Delta\phi}_{\rm noflip}$ (respectively), taken over the following and preceding two steps (so four intervals total), and (3) flip those pixels for which

$$|\overline{\Delta\phi}_{\rm flip}| < |\overline{\Delta\phi}_{\rm noflip}|. \quad (1)$$

For the "filtered" azimuth changes shown in the top-left panel of Fig. 1, a threshold of $|\Delta\phi| > 120^\circ$ was used to define large flips. To improve upon the approach from Welsch et al. (2013), we have implemented two changes. First, to reduce the "turn-on" jump due to the threshold at 120°, we applied a linear weighting coefficient, $w(\Delta\phi)$, to the right-hand side of the inequality in Eq. (1) above, with

$$w(\Delta\phi) \equiv \frac{|\Delta\phi| - 120^\circ}{180^\circ - 120^\circ}. \quad (2)$$

This weighting smoothly "turns on" the azimuth flipping, increasing the likelihood that a pixel's azimuth will be flipped as $|\Delta\phi|$ approaches 180°. The effect of using this weighting is shown in the red curve in the lower-right panel of Fig. 1, which lacks any jump at 120°. Second, we determined that the azimuth filtering procedure was not idempotent – that is, applying it a second time yields a different result than applying it just once. The blue curve in the lower-right panel of Fig. 1 shows the result of applying it twice. This second application eliminates the excess in azimuth changes beyond 120°. Defining "strong fields" in terms of $|\mathbf{B}|$ instead of $|B_{\rm LOS}|$ did not qualitatively change our results, nor did basing the definition of large changes in direction in terms of $\Delta\hat{\mathbf{B}}$, where $\hat{\mathbf{B}}$ is the local unit vector along $\mathbf{B}$, instead of $\Delta\phi$.

Further characterization of this and related methods to reduce unrealistic changes in azimuths is underway. One promising approach, still being developed and tested, is iterative: azimuths are flipped to optimize temporal consistency throughout fixed-length data series. In contrast with the *sequential* approach to impose persistence developed by Welsch et al. (2013) and updated as above, the iterative technique is a *simultaneous* optimization.

2.2. Changes in magnetic helicity & energy in X-class flares

Flares and CMEs are powered by the release of free magnetic energy that is stored in the corona, in the form of electric currents. This energy is injected into the corona from the solar interior, both via emergence of current-carrying magnetic flux and near-surface flows acting on already emerged fields (e.g., shearing and twisting motions). The nature of energy input that is most relevant for flare/ CME onset, however, is unclear, as are the relative timings of energy input and release. The presence of magnetic helicity in the corona is associated with the build up of free magnetic energy there (see, e.g., Heyvaerts and Priest, 1984; Berger, 1984), but its role in the genesis of CMEs remains unclear (but see, e.g., Low, 2001; Low, 2002 for related discussion).

Recently these questions have been intensively investigated and discussed (e.g., Valori et al., 2016; Thalmann et al., 2021; Green et al., 2022). We have systematically analyzed photospheric magnetic evolution around the time of 15 X-class flares, produced by 11 active regions (ARs), each of which produced a CME. Here, we focus on the photospheric fluxes of magnetic energy and helicity. A comprehensive analysis on evolution of helicity and energy in the ARs during flares is reported in Liu et al. (2023).

2.2.1. Sample & data

From the set of all X-class flares from 2010 to 2017 with available HMI observations, we chose to study 11 ARs that produced X-class flares associated with CMEs (eruptive flares). These ARs and associated flares are listed in Table 1. We exclude confined flares (with which no CMEs have been associated) from the analysis here, because helicity changes from such flares might not be substantial. A study including both eruptive and confined flares is presented in Liu et al. (20230. We analyzed HMI vector magnetograms with 720-s cadence and 1" resolution (pixel width $\simeq$ 350 km at disk center).

2.2.2. Calculation of helicity and energy fluxes

The flux of relative magnetic helicity across a surface S is expressed by Berger (1984),

$$\left.\frac{dH}{dt}\right|_S = 2\int_S (\mathbf{A}_p \cdot \mathbf{B}_t) V_{\perp n} dS - 2\int_S (\mathbf{A}_p \cdot \mathbf{V}_{\perp t}) B_n dS, \quad (3)$$

where: $\mathbf{A}_p$ is the vector potential of the potential field $\mathbf{B}_p$; $\mathbf{B}_t$ and B_n denote the observed tangential and normal magnetic fields, respectively; and $\mathbf{V}_{\perp t}$ and $\mathrm{V}_{\perp n}$ are the tangential and normal components of velocity $\mathbf{V}_\perp$, the velocity perpendicular to the magnetic field. The integral runs over the surface imaged in the magnetogram. Assuming the Coulomb gauge, the vector potential $\mathbf{A}_p$ for the potential field on the photosphere is uniquely determined by the observed photospheric normal magnetic field via Berger (1997) and Berger and Ruzmaikin (2000):

$$\nabla \times \mathbf{A}_p \cdot \hat{\mathbf{n}} = B_n, \quad \nabla \cdot \mathbf{A}_p = 0, \quad \mathbf{A}_p \cdot \hat{\mathbf{n}} = 0. \quad (4)$$

Similarly, the magnetic energy (Poynting) flux can be calculated by

Table 1
CME-producing X-class flares studied, from ARs within 50° of central meridian from May 2010 through 2017.

FLARE Start	Peak	End	Flare	AR	Position
2011-02-15T01:44:00	2011-02-15T01:56:00	2011-02-15T02:06:00	X2.2	11158	S21W28
2011-09-06T22:12:00	2011-09-06T22:20:00	2011-09-06T22:24:00	X2.1	11283	N14W18
2011-09-07T22:32:00	2011-09-07T22:38:00	2011-09-07T22:44:00	X1.8	11283	N14W18
2012-03-07T00:02:00	2012-03-07T00:24:00	2012-03-07T00:40:00	X5.4	11429	N17E27
2012-03-07T01:05:00	2012-03-07T01:14:00	2012-03-07T01:23:00	X1.3	11429	N17E26
2012-07-12T15:37:00	2012-07-12T16:49:00	2012-07-12T17:30:00	X1.4	11520	S15W01
2013-11-05T22:07:00	2013-11-05T22:12:00	2013-11-05T22:15:00	X3.3	11890	S09E36
2013-11-08T04:20:00	2013-11-08T04:26:00	2013-11-08T04:29:00	X1.1	11890	S09W20
2013-11-10T05:08:00	2013-11-10T05:14:00	2013-11-10T05:18:00	X1.1	11890	S09W30
2014-03-29T17:35:00	2014-03-29T17:48:00	2014-03-29T17:54:00	X1.0	12017	N11W32
2014-09-10T17:21:00	2014-09-10T17:45:00	2014-09-10T18:20:00	X1.6	12158	N12E29
2014-11-07T16:53:00	2014-11-07T17:26:00	2014-11-07T17:34:00	X1.6	12205	N15E33
2014-12-20T00:11:00	2014-12-20T00:28:00	2014-12-20T00:55:00	X1.8	12242	S18W29
2015-03-11T16:11:00	2015-03-11T16:22:00	2015-03-11T16:29:00	X2.1	12297	S16E13
2017-09-06T11:53:00	2017-09-06T12:02:00	2017-09-06T12:10:00	X9.3	12673	S09W38

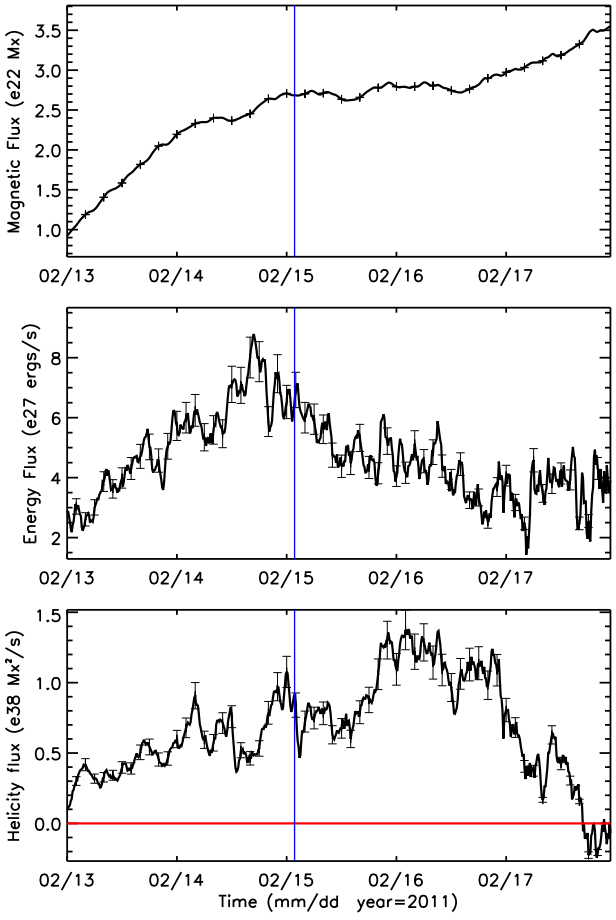

Fig. 2. Temporal profiles of unsigned magnetic flux (top), energy flux (middle), and helicity flux (bottom) in AR 11158 from 2011 February 13–17, smoothed with one-hour running average. Vertical blue lines denote the start time of an X-class flare at 01:56 UT, 2011 February 15. 1σ errors are shown at representative data points.

$$\left.\frac{dE}{dt}\right|_S = \frac{1}{4\pi}\int_s B_t^2 V_{\perp n}\, dS - \frac{1}{4\pi}\int_S (\mathbf{B}_t \cdot \mathbf{V}_{\perp t}) B_n\, dS. \qquad (5)$$

The vector velocity field in the photosphere is derived from the Differential Affine Velocity Estimator for Vector Magnetograms (DAVE4VM; Schuck, 2008) which is applied to the time-series deprojected, registered vector magnetic field data. The window size used in DAVE4VM is 19 pixels, and velocities are inferred from ΔB_n from differencing magnetograms ± 720s from the measurement of $\mathbf{B}$, i.e., $\Delta t = 1440\text{s} = 24$ min.

2.2.3. Change of helicity and energy fluxes in X-class flares

To illustrate the nature of the energy and helicity fluxes that we typically find, we show some example time series from NOAA AR 11158 from February 13 to 17, 2011 in Fig. 2, which shows temporal profiles of unsigned magnetic flux (top), energy flux (middle), and helicity flux (bottom) during this interval. A one-hour running average was applied to the helicity and energy fluxes. The blue vertical lines denote the start time of an X2.2 flare that was associated with a CME. The increase of magnetic flux in the top panel indicates that flux emergence was ongoing in AR 11158 during this interval. The injection rates of helicity and energy through the photosphere appear to be lower in the hours after the flare than in the several hours preceding it. Also, there appears to be a significant decrease in the helicity injection rate associated with the flare, although other large and sudden changes in helicity flux can be seen in the series.

The energy and helicity fluxes for AR 11158 exhibit large fluctuations, a property common among ARs in our sample. To discover evolutionary patterns typical in events in our sample, we employ superposed epoch (SPE) analysis: we first shift each AR's sequence of flux estimates in time to a common epoch, with all flare start times aligned to $t = 0$, the "key time." We then superpose all ARs' fluxes by averaging them. Fig. 3 shows the shifted-and-averaged unsigned helicity flux (top) and energy flux (bottom). Both helicity and energy fluxes decrease substantially after the events, followed by a recovery.

The decreases in helicity and energy fluxes after eruptive X-class flares must be related to changes in the magnetic

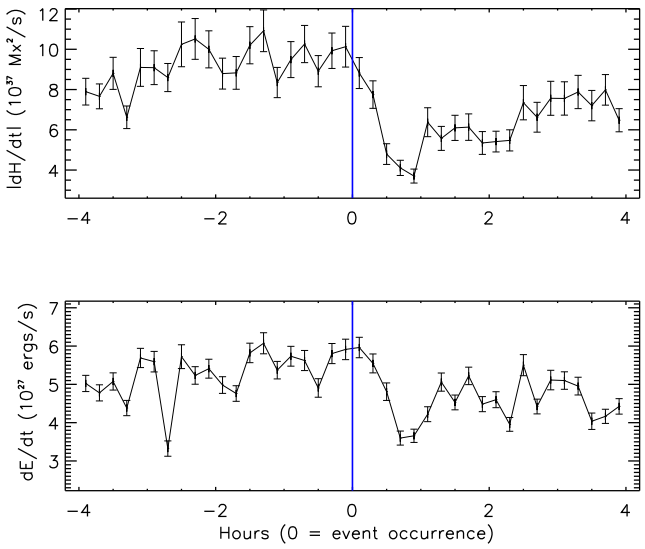

Fig. 3. Superposed Epoch analysis (SPE) plots for unsigned helicity flux (top) and energy flux (bottom) for all the events listed in Table 1 (15 eruptive X-class flares): each black curve is an average for all events in our sample, with each event's time series shifted to move its flare start time to zero (the "key time"), denoted by the vertical blue line on each plot. No running averaging has been applied to the fluxes. 1σ errors are shown.

and velocity fields upon which these fluxes depend. Indeed, it has been shown that the horizontal field in flare areas increases substantially after major flares (e.g. Wang and Liu, 2010; Sun et al., 2012a). Changes in velocities associated with large flares have also been reported (Deng et al., 2006). To understand how these changes impact helicity and energy fluxes, we analyzed the histograms of pixel counts in the 2-variable phase space of magnetic field strength and total velocity that participated in eruptive flares.

As a first step, we produced a so-called flare mask for each event, to isolate areas associated with the flare. Eruptive ARs, especially complex ones, often contain substantial flux that does not erupt, and connects to other polarities within the AR, to neighboring ARs, or to remote areas on the Sun. Because random changes from such irrelevant flux systems could conceal the variations associated with flares that interest us, we restrict our study of changes in **B** and **v** as much as possible to areas of flaring fields. To do so, we selected areas to include in our flare masks by visual inspection of both maps of the squashing factor Q (Titov, 2007; Titov et al., 2011) and the observed locations of flare arcades and ribbons. Details about procedures used to generate flare masks are discussed by Liu et al. (2017). In most cases, this provides a good proxy for the area containing erupting flux. In each flare mask, we set the selected area to unity and remaining areas to zero.

We then applied each flare mask to maps of the pre- and post-flare magnetic and velocity fields for all events. In the left panel of Fig. 4, we show the pre-flare histograms of the log of pixel counts in the 2-variable phase space of magnetic field strength and total velocity before the flares. In

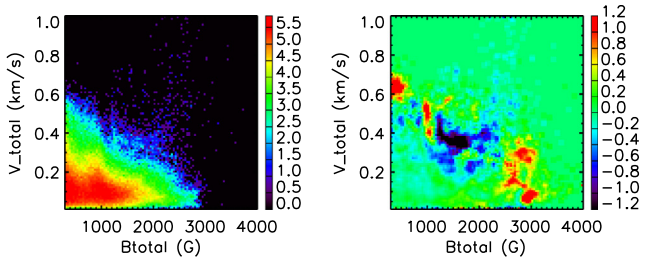

Fig. 4. Left: Two-dimensional histogram of pixel counts (in log) in the two-variable phase space of magnetic field strength and total velocity before the flares; Right: difference of histograms of the log of pixel counts before and after flares (difference = log(pixel count)$_{after}$ - log(pixel count)$_{before}$.) for all the erupted events. Only the pixels in the flare masks are included.

the right, we show histograms of *differences* in pixel counts, i.e., log(post-flare counts) - log(pre-flare counts), in the same, 2-variable space. In the right panel, red indicates that more pixels occupy a given part of this space, blue indicates that fewer do. These distributions show that, after flares, we see clear increases in strong-field pixels with relatively low $|\mathbf{V}|$ (red features near 3000 G and 0.2 km s^{-1}) and decreases in moderate-strength pixels with moderate speeds (blue features near 2000 G and 0.4 km s^{-1}). An increase in weak-field pixels with large $|\mathbf{V}|$ can also be seen. Because stronger fields suppress convection more effectively than weaker ones (e.g., Berger et al., 1998; Welsch et al., 2012), it is plausible that the increases in horizontal field strengths that occur in strong flares shifted pixels from the central blue patches to the strong-field red patches. This change in magnetic fields and velocity fields could be responsible for the decreases in the fluxes of helicity and energy that we observe after eruptive X-class flares.

2.3. Summary of improvements in photospheric magnetic vector estimation & characterization of CME-related magnetic evolution

Disambiguation of the transverse magnetic field vector's direction is a key step in producing reliable photospheric magnetic field data for studies of solar eruptions. Such studies rely upon accurate determination of horizontal and radial magnetic field components, both to study the structure and evolution of the photospheric field itself and to model the structure of the coronal magnetic field and its evolution. By incorporating the assumption of persistence into inference of transverse-field azimuths, we can improve the robustness of inputs for such studies.

Time series of photospheric vector magnetic field measurements enable estimation of the fluxes of magnetic energy and helicity across the photosphere. Superposed epoch analysis of these fluxes around the times of 15 CME-productive, X-class flares reveal eruption-induced decreases in helicity and energy fluxes after eruptive flares occur. These decreases are linked to changes in photospheric magnetic and velocity fields associated with flares. We continue to investigate the nature of these changes.

3. The implications of different surface flux transport models for CME modeling (Barnes Team)

Modeling of CMEs, particularly their propagation through the heliosphere, typically requires at least a global map of the photospheric or low coronal radial magnetic field. For example, Wang et al. (2022), published in Tier 1 of this special issue, makes extensive use of potential field source surface models of the corona and heliosphere, which are based on such radial field maps, to investigate how this global field deflects the trajectory of erupting CMEs. A wide variety of other models (see Mackay and Yeates, 2012 for an overview), ranging from nonlinear force-free field approaches (e.g., Wiegelmann, 2007; Amari et al., 2013) through magnetofrictional methods (e.g., Cheung and DeRosa, 2012) to full MHD simulations (e.g., Mikić et al., 1999; Gombosi et al., 2018; Perri et al., 2022) also rely on these global maps, or in some cases integrate the generation of the global map into the coronal model (van Ballegooijen et al., 2000; Mackay and van Ballegooijen, 2006), making them critical for understanding and predicting space weather phenomena.

Observations of the photospheric field are only routinely available for the Earth-facing hemisphere of the Sun, and can be less reliable towards the solar limb. Thus, it is generally necessary to model the evolution of the photospheric magnetic field on the areas of the Sun where no reliable observations are made. A variety of surface flux transport (SFT) models have been developed for this purpose, including the Air Force Data Assimilative Photospheric Flux Transport (ADAPT; Arge et al., 2010; Arge et al., 2013; Hickmann et al., 2015) model and the SFT model distributed with the `pfss` package available through SolarSoft (SSW-PFSS; Schrijver, 2001). These models differ in the meridional flow profiles used to advect flux, and in the treatment of how supergranulation/convection disperses the flux. The ADAPT model typically produces twelve realizations, corresponding to different possible evolution of the field due to the supergranulation. These realizations differ in the random selection of the supergranule locations. These different realizations make it possible to evaluate the impact of differences in the SFT model assumptions and implementation from the selection of a particular realization of the small scale processes.

To evaluate the impact of the different SFT models, predictions from the Wang-Sheeley-Arge (WSA; Arge and Pizzo, 2000; Arge et al., 2003; Arge et al., 2004; McGregor et al., 2008) model are used. The WSA model is a combined empirical and physics based model of the corona and solar wind. It is an improved version of the original Wang and Sheeley model (Wang et al., 1995). In the WSA model, the output of a Potential Field Source Surface (PFSS) model at 2.5 R_s serves as input to the Schatten Current Sheet (SCS) model, which provides a more realistic magnetic field topology of the upper corona than a simple radial expansion. An empirical relationship, based on a flux tube expansion factor and the minimum angular separation at the photosphere between an open field footpoint and the nearest closed field footpoint, is used to determine the solar wind speed at the outer boundary.

In Barnes et al. (2023), we evaluate a larger range of predictions; here, we highlight results focusing on sector boundaries, solar wind speed, and coronal magnetic null points for 2012 April. Null points (i.e., locations where the magnetic field vector vanishes) may be an important topological feature in the initiation of CMEs, while the location of the sector boundaries and the background solar wind speed can be important in the propagation of a CME.

Fig. 5 shows the sector structure in different models for 2012 April 1. The sector boundary is morphologically similar, but does not exactly track between either the different

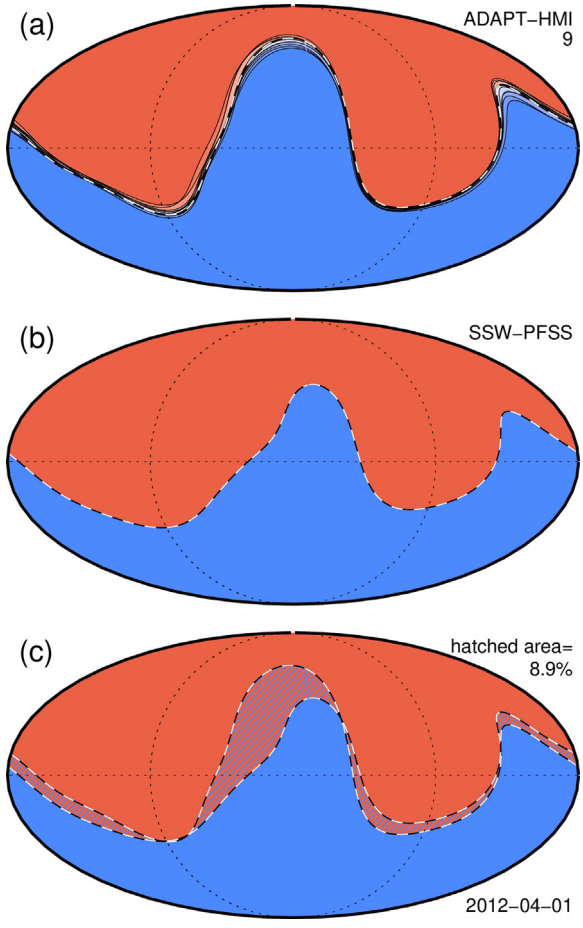

Fig. 5. Sector structure at a radius of 2.5$R_\odot$ for 2012 Apr 1 for (a) the set of 12 ADAPT-HMI models, and (b) the SSW-PFSS model. Mollweide projections are used and the sectors are shaded red (negative) or blue (positive), depending on polarity. The horizontal dashed line marks the solar equator, and the dashed circle is at $\pm 90^\circ$ longitude from central meridian. In panel (a), the black-and-white dashed line represents the polarity inversion line corresponding to ADAPT map #9, which is deemed to best "represent" the set, i.e., has the least amount of disagreement with all of the others in the set. Panel (c) enables a comparison between the representative ADAPT map and the SSW-PFSS. The regions where the polarities of the sectors from both maps agree are colored red and blue based on the polarity; the hatched region indicates the areas where the polarity of one model differs from the other, and encompasses 8.9% of the total area.

realizations of ADAPT or between the SSW-PFSS model and ADAPT. The difference between the sectors from any pair of ADAPT realizations is much smaller than the difference between the sectors predicted from SSW-PFSS and any ADAPT map. To quantify the agreement between models, we compute the fraction of the area in which at least two models predict different polarity. For the date shown, the median percentage area of disagreement is 2% amongst predictions from the different realizations of the ADAPT model, compared with 9% between the predictions from the SSW-PFSS model and one representative realization of the ADAPT model. Even the largest area of disagreement amongst the predictions from the ADAPT realizations is only 4%. Thus, although there is overall good agreement in the sector structure on this date, the differences that do arise are predominantly due to the implementation and model assumptions.

Fig. 6 shows the difference in the solar wind speed predicted by the WSA model between a representative realization of the ADAPT model and the SSW-PFSS model on 2012 April 1. Over the vast majority of the area, the difference in wind speed between pairs of ADAPT realizations is less than 100 km s^{-1}. The differences are typically seen near the boundary between slow and fast wind, where different realizations predict slightly different extents of high speed wind. As is the case for the sector structure, the differences among predictions from pairs of ADAPT realizations are substantially smaller than the difference between predictions from SSW-PFSS and a representative ADAPT realization.

Fig. 7 shows the null points found in the PFSS region of the WSA model initialized from the twelve realizations of the ADAPT model and the SSW-PFSS model on 2012 April 1. The null points were located using the trilinear method described in Haynes and Parnell (2007). A cluster-

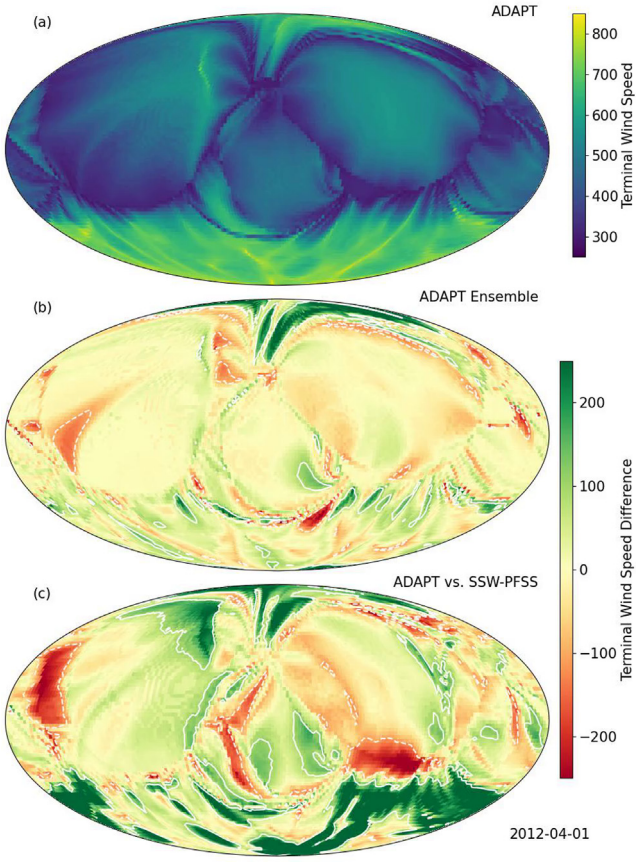

Fig. 6. Solar wind speed predictions from the WSA model at 5.0 $R_\odot$ for 2012 April 1, shown in a Mollweide projection. Panel (a) shows the wind speed predicted by a representative ADAPT-HMI realization. Panel (b) shows the median difference between the wind speed predicted from the representative ADAPT-HMI realization and all the other realizations. Panel (c) shows the difference between the wind speed predicted from the representative ADAPT-HMI realization and the SSW-PFSS model. In panels (b) and (c), the contour encloses differences of at least 100 km s^{-1}, indicating areas of reasonable agreement between wind speed predictions. The extent of the high speed wind area near the north pole [light green area near the top of panel (a)] generated from the ADAPT-HMI boundary condition varies between realizations, as shown by the area of dark green in panel (b), but overall there is relatively little variation in the wind speed predictions among the ADAPT-HMI boundary conditions. The predictions from the SSW-PFSS model show substantially more variations [large areas of dark green and red in panel (c)], due to differences in the south polar field.

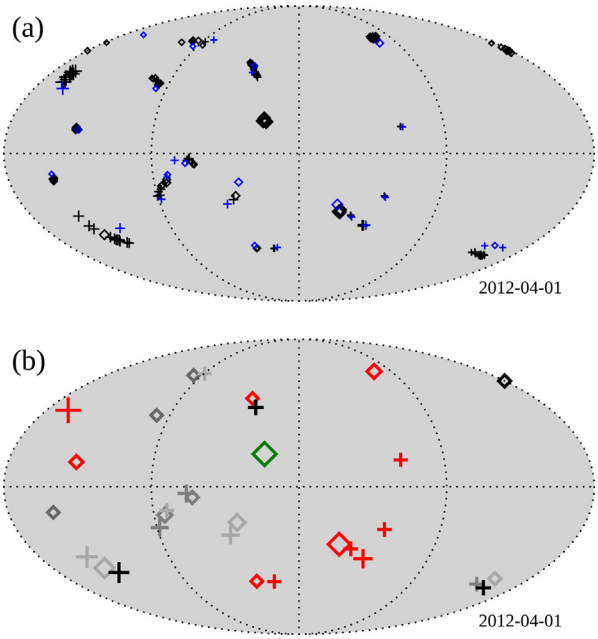

Fig. 7. Null points on 2012 April 1, shown in a Mollweide projection. Panel (a) shows all the null points found for the different models. Black symbols indicate null points that are present in the PFSS extrapolation for any realization of the ADAPT-HMI model; blue symbols indicate null points in the SSW-PFSS model. Positive and negative nulls are shown with pluses and diamonds respectively, while the symbol size is proportional to the radius of the null (i.e., large symbols indicate nulls that are at a large radius). Only null points assigned to a cluster with radius larger than 1.05$R_\odot$ are shown for clarity. Panel (b) shows the corresponding position of each cluster mean, with the symbol color determined by the number of nulls in the cluster. Red indicates a null that is present in the PFSS extrapolation for all 12 realizations of ADAPT-HMI plus SSW-PFSS, green indicates a null that is present in the PFSS extrapolation for all 12 realizations of ADAPT-HMI, but *not* SSW-PFSS, while shades of black to grey indicate decreasing numbers of nulls in the cluster.

ing algorithm, based on k-means (Feigelson and Babu, 2012), was used to identify which null points are present in different realizations (Barnes et al., 2023). In many cases, the same null point is found in all the realizations of the ADAPT model as well as the SSW-PFSS model, but there are also cases of null points being found in only the SSW-PFSS model, only in the ADAPT model, and in the SSW-PFSS model plus some but not all of the realizations of ADAPT.

To quantify this, we calculated the fraction of null points that are present in each pair of ADAPT realizations, and the fraction of null points that are found in the SSW-PFSS model and each ADAPT realization, that is, the Jaccard index for the sets of null points present in pairs of models. The results of this are shown for 2012 April in Fig. 8. Throughout this interval, null points are much more likely to be present in both the PFSS extrapolations from a pair of ADAPT-HMI maps than in both the PFSS extrapolation from the representative ADAPT-HMI map and the SSW-PFSS model.

Overall, we find that the predictions are more sensitive to the model assumptions than to the selection of a particular realization of the evolution of the small scale flows. In the cases of the sector structure and the wind speed, the degree of this sensitivity depends strongly on solar cycle. When strong polar fields are present, around solar minimum, the differences in the sector boundaries can largely be explained by variations in the treatment of the supergranulation. Around the time of the pole reversal, near solar maximum, the sector boundaries become highly uncertain, even when the underlying magnetic fields are not much different between the global maps.

The wind speed agreement exhibits a different solar cycle dependence, with the largest differences occurring near solar minimum. This is primarily a result of the mean polar field strength, in each hemisphere, being substantially larger in all the realizations of ADAPT than in the SSW-PFSS model, resulting in more high speed wind from polar coronal holes in the ADAPT model than in the SSW-PFSS model. In addition, the latitude of the greatest differences in wind speed depends on the solar cycle; when the poles are weak, the greatest differences are seen at high latitudes, while closer to solar minimum, the differences are at low latitudes.

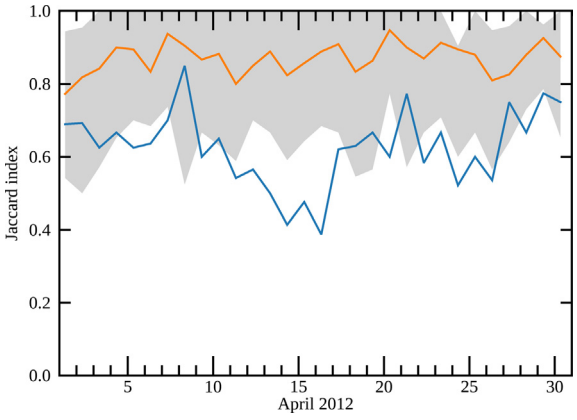

Fig. 8. The Jaccard index for the null points present in the PFSS extrapolation from a representative realization of the ADAPT-HMI model and the SSW-PFSS model (blue), and the median Jaccard index for null points in the PFSS model from the representative ADAPT-HMI realization and all the other realizations (orange) once per day for April 2012; the shaded band indicates the extent of the variations among the ADAPT-HMI realizations. The reference realization is the one with the maximum agreement with the other realizations. Only null points whose average radius is greater than $1.05\,R_{\odot}$ are included.

The null point agreement shows a weaker solar cycle dependence. Null points are much more likely to be present in both the PFSS extrapolations from a pair of ADAPT-HMI maps than in both the PFSS extrapolation from the representative ADAPT-HMI map and the SSW-PFSS model approaching solar maximum, but by solar minimum, the SSW-PFSS nulls points cannot be clearly distinguished from the null points in the PFSS model from an ADAPT-HMI realization. This is likely an indication of the importance of the small scale fields near solar minimum in determining the presence of null points.

Finally, large but transient changes can be seen in the model predictions when an active region is crossing the edge of the assimilation window. Specifically, during the time when there is substantial magnetic flux that has been assimilated by one model but not by another because of the different locations of the assimilation window, the sector boundaries are substantially different. These differences manifest not just in the vicinity of the active region being assimilated but can also substantially influence the sector boundary in the opposite hemisphere from the active region.

The investigation described here focused on characterizing the differences between predictions from two SFT models without trying to determine which resulted in the best predictions. The obvious next step is to compare the predicted properties to observations to determine which SFT model performs best, and perhaps more importantly, to understand why some predictions are better than others. To do this, the footpoints of open magnetic flux are typically compared to the locations of coronal holes, while predictions of solar wind properties are compared with in situ measurements. These comparisons present their own challenges, but new techniques, such as applying dynamic time warping to time series of in situ observations may provide more informative comparisons (Owens and Nichols, 2021; Samara et al., 2022), and it may also be possible to validate the presence and location of magnetic null points with observed structures in coronal image data (Freed et al., 2015).

4. Boundary data-driven MHD simulation of the eruptions of Active Region 11158 (Fan team)

Developing data-driven simulations to model the realistic, complex magnetic field evolution of the observed major solar eruptive events is necessary to distinguish among the

possible mechanisms at the origin of solar eruptions. This is a field of active research and has seen significant advancement in recent years. See a recent comprehensive review by Jiang et al. (2022) and the development of synthetic test beds by e.g. Chen et al. (2023). As part of our contribution to the NASA LWS FST team effort, we have devised a new formulation of the horizontal electric field for driving the lower boundary flux transport of data-driven simulations based on the observed evolution of the normal magnetic field B_r and the vertical electric current measured from photosphere vector magnetograms, and applied it in MHD simulations of a major solar eruptive event. NOAA Active Region 11158 was a well observed quadrupolar δ-sunspot group that produced an X2.2 flare and an associated halo CME on 2011–02-15 at about 01:44 UT (e.g. Schrijver et al., 2011; Sun et al., 2012b). Here we present initial results of a boundary data-driven MHD simulation of the magnetic field evolution of this eruptive event using the electric field inferred from the SDO/HMI vector magnetograms (given at a time cadence of 12 min and spatial resolution of 360 km) as the lower boundary driving conditions.

4.1. Simulation setup and the observationally inferred lower boundary driving electric field

For this simulation, we use the "Magnetic Flux Eruption" (MFE) code that solves the set of semi-relativistic MHD equations as described in Fan (2017). We refer the readers to that paper for a detailed description of the numerical model. Here we only describe the changes made specifically for the current simulation. As in Fan (2017), we assume for the thermodynamics an ideal gas of fully ionized hydrogen, with $\gamma = 5/3$, and with the internal energy equation taking into account the following non-adiabatic effects that include the field aligned thermal conduction, optically thin radiative cooling, and heating due to numerical diffusion. We no longer include an empirical coronal heating (eq. (14) in Fan, 2017) for the heating term in the internal energy equation (term H in Eq. (5) of Fan, 2017), but only include the heating resulting from the dissipation of the kinetic and magnetic energies due to the numerical diffusion (see description in the first paragraph on p.3 of Fan, 2017). As described below, for this simulation, we add to the lower boundary a random electric field representing the effect of turbulent convection that drives field line braiding, and the resultant (numerical) resistive and viscous heating provides the necessary heating of the corona. Compared with an empirical coronal heating, this heating varies spatially and temporally more self-consistently with the formation of strong current layers in the given 3D magnetic field.

The simulation domain is a spherical wedge domain with the lower boundary centered on the tracked active region, with a latitudinal width of 17.2 degrees, and a longitudinal width of 18.8 degrees, and with a radial range of 1 to 1.43 solar radius. Fig. 9 shows a view of the simulation domain box from the earth perspective. The simulation grid is $360(r) \times 288(\theta) \times 315(\phi)$. It is stretched in the radial direction (with Δr being a geometric series) and uniform in the horizontal directions. The peak radial resolution is 300 km near the bottom, and the horizontal resolution is 724 km at the bottom.

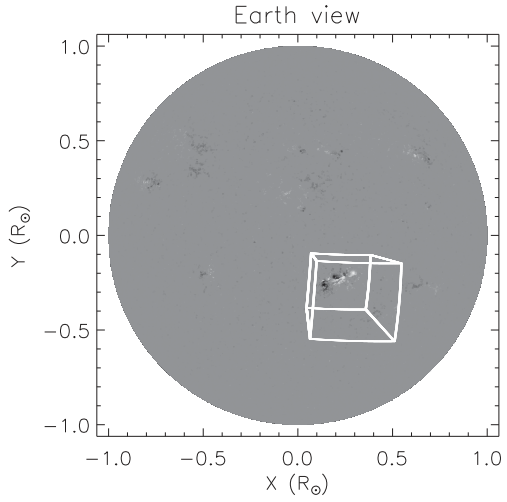

Fig. 9. The local spherical wedge simulation domain (the white box) as viewed from the earth perspective.

For the lower boundary, even though the driving electric field is derived from the photosphere magnetograms, we impose a fixed chromosphere temperature of 20,000 K and density of $10^{12}\,\mathrm{cm}^{-3}$. We also impose a time dependent horizontal electric field $\mathbf{E}_h$ that is composed of 3 parts:

$$\mathbf{E}_h = \mathbf{E}_h^P + \mathbf{E}_h^{\mathrm{Tw}} + \mathbf{E}_h^{\mathrm{random}}. \tag{6}$$

The first part $\mathbf{E}_h^P$ corresponds to the horizontal component of the "PTD" (Poloidal-Toroidal-Decomposition) electric field derived in Fisher et al. (2020) (the horizontal component of Eq. (8) in that paper):

$$c\mathbf{E}_h^P = -\nabla \times \left(\dot{P}\hat{\mathbf{r}}\right) \tag{7}$$

where $\dot{P}$ is determined from the observed normal magnetic field B_r evolution on the photosphere by solving the 2D Poisson equation (eq. (9) in Fisher et al., 2020):

$$\nabla_h^2 \dot{P} = -\dot{B}_r, \tag{8}$$

due to Faraday's law. Thus imposing $\mathbf{E}_h^P$ reproduces the observed photospheric normal magnetic field evolution on the lower boundary. The second electric field $\mathbf{E}_h^{\mathrm{Tw}}$ on the right hand side of Eq. (6) is given as the horizontal gradient of a potential such that it does not alter the observed B_r evolution (already produced by imposing the $\mathbf{E}_h^P$ component), and is assumed to correspond to the vertical transport of a horizontal magnetic field into the domain, i.e.

$$c\mathbf{E}_h^{\mathrm{Tw}} = -\nabla_h \psi^{\mathrm{Tw}} = -v_0 \hat{r} \times \mathcal{B}_h \tag{9}$$

where v_0 is the vertical speed of transport, which we assume to be a constant, and $\mathcal{B}_h$ is a horizontal magnetic field

(which is not the same as the observed horizontal field). Taking the divergence of Eq. (9) yields:

$$\nabla_h^2 \psi^{\rm Tw} = -v_0 (\nabla_h \times \mathcal{B}_h)_r, \tag{10}$$

and we let $(\nabla_h \times \mathcal{B}_h)_r$ be the same as $J_r = (\nabla_h \times \mathbf{B}_h)_r$ which is the measured vertical electric current of the observed horizontal magnetic field at the photosphere:

$$\nabla_h^2 \psi^{\rm Tw} = -v_0 J_r. \tag{11}$$

Thus we determine the potential $\psi^{\rm Tw}$ by solving the above 2D Poisson equation given the measured vertical electric current at the photosphere J_r from the HMI vector magnetograms and specifying v_0, which is an *ad hoc* parameter we can adjust. For the simulation presented here we have used $v_0 = 2.5\,\mathrm{km/s}$. We have experimented with the value of v_0 to some extent, such that it is as small as possible to ensure a quasi-static evolution of the domain during the build-up phase and still strong enough to compete with the numerical diffusion and produce eruptive behaviors similar to the observed eruption. With $\psi^{\rm Tw}$ determined, the twisting electric field $\mathbf{E}_h^{\rm Tw}$ is given by Eq. (9). Imposing $\mathbf{E}_h^{\rm Tw}$ at the lower boundary corresponds to transporting a (divergence-free) horizontal magnetic field with the observed vertical electric current into the domain, without altering the normal magnetic field evolution at the lower boundary. Thus it effectively transports twist into the corona based on the observed vertical electric current. We note that in Fisher et al. (2020), the vertical component of the PTD electric field (the second term on the right hand side of Eq. (8) in that paper) is also determined based on the observed vertical electric current, and may play a similar role of driving twist into the corona. The similarity and difference between the effects of the vertical PTD electric field of Fisher et al. (2020) and the horizontal twisting electric field used here is a subject of future investigation. Another similar way of using a horizontal electric field to drive twist into the corona has been applied in the magneto-frictional modeling of the evolution of AR 11158 (Cheung and DeRosa, 2012). Although in that case, effectively a uniform rotation of all the polarity concentrations is applied to drive the same sign of twist into the corona. Here the twist injection varies spatially based on the distribution of the observed vertical electric current.

Fig. 10 shows snapshots of the observed vertical magnetic field B_r, vertical electric current density J_r, and the derived horizontal twisting electric field $E_\theta^{\rm Tw}, E_\phi^{\rm Tw}$ components at the lower boundary at the time of about 1.9 h before the onset of the observed X-class flare. It can be seen from panels (a) and (b) that strong J_r is present near the central polarity inversion line (PIL), where J_r tends to be of the same sign as B_r in the polarity concentrations P2 and N1. On the other hand, in the polarity concentration N2, we see J_r of predominantly opposite sign as the sign of B_r. Consequently, the derived twisting electric field (panels (c) and (d)) would transport positive twist into the corona at the cental P2, N1 polarity concentrations and

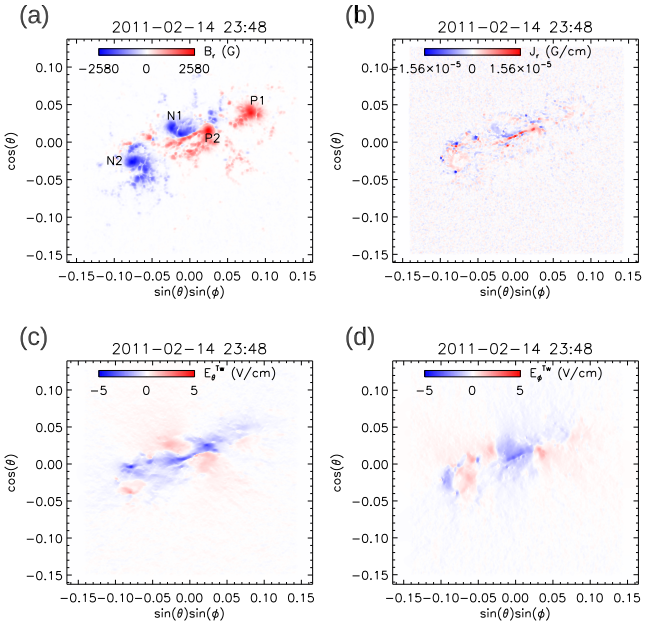

Fig. 10. Snapshots of the oberved vertical magnetic field B_r (a), vertical electric current density J_r (b), and the horizontal twisting electric field components: $E_\theta^{\rm Tw}$ (c), and $E_\phi^{\rm Tw}$ (d) at the lower boundary at 23:48 UT 2011–02-14, about 1.9 h before the onset of the observed X-class flare.

negative twist into the corona at the N2 polarity concentration. At the central PIL $E_\theta^{\rm Tw}$, and $E_\phi^{\rm Tw}$ transport a concentrated horizontal shear magnetic field into the corona. They also effectively drive a clockwise rotation of the footpoints of P2 and N1 flux concentrations and a counter-clockwise rotation of the N2 flux concentration.

The last term on the right hand side of Eq. 6 is a random, horizontal electric field $\mathbf{E}_\mathbf{h}^{\rm random}$ given by:

$$c\mathbf{E}_h^{\rm random} = -\nabla_h(\xi B_r), \tag{12}$$

where ξ is a time dependent field that is made up of a superposition of 15721 randomly placed cells of opposite sign values. Each of the cells is spatially a 2D Gaussian profile with a size scale of 1.74 Mm and a peak amplitude of $4.07 \times 10^{13}\mathrm{cm}^2/\mathrm{s}$, and temporally a sinusoidal function with a period and life time of 11.89 min. A snapshot of the ξ field is illustrated in Fig. 11, showing the random cell pattern. $\mathbf{E}_h^{\rm random}$ effectively drives random rotations of the footpoints of the B_r flux concentrations, with positive (negative) ξ producing clockwise (counter-clockwise) rotation. Since the positive and negative cells in the ξ field are statistically balanced, there is no net twist or helicity driven into the corona by $\mathbf{E}_h^{\rm random}$. Note again, since $\mathbf{E}_h^{\rm random}$ is the gradient of a potential (eq. [12]), it does not alter B_r on the lower boundary and thus preserves the (observed) normal magnetic flux distribution that is reproduced by imposing $\mathbf{E}_h^P$. $\mathbf{E}_h^{\rm random}$ represents the effect of turbulent convection that drives field-line braiding and the consequent resistive and viscous heating in the corona. Similar ways of driving coronal heating by imposing random footpoint motions that represent turbulent convection at the photospheric

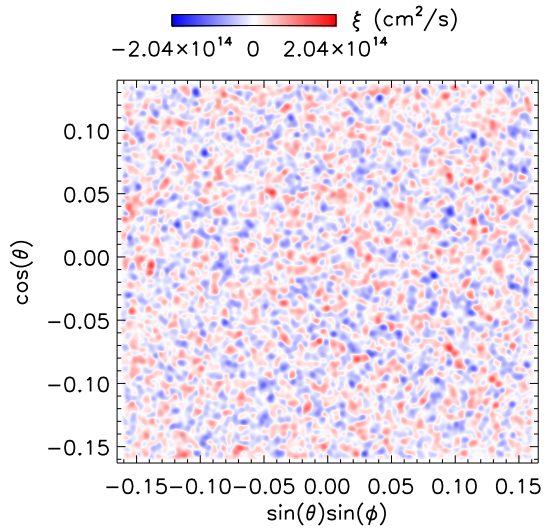

Fig. 11. A snap shot of the ξ field used for the random electric field (see text for description).

lower boundary of MHD simulations have been widely used (e.g. Gudiksen and Nordlund, 2005; Bourdin et al., 2013; Warnecke and Peter, 2019).

We further note that the $\nabla_h(\xi B_r)$ of the random electric field here in Eq. (12) has the same form as the STITCH electric field $\nabla_s(\zeta B_n)$ given in Eq. (13) in Section 6.1 (with ∇_h corresponding to ∇_s, ξ to ζ, and B_r to B_n). The difference is that the STITCH electric field uses a large-scale, like-signed ζ field, whereas here the random electric field uses a collection of small-scale cells of random signs for the ξ field. Thus here we use the random electric field to represent the driving effect of a small-scale turbulent convection with no net helicity transported into the corona, whereas the STITCH electric field represents a large-scale statistical mean effect of a helical convection that transports a net helicity into the corona (see description of the STITCH subgrid model in Section 6.1).

For the side boundaries of the simulation domain, we assume conducting walls with the magnetic field and velocity field parallel to the walls. For the top boundary, a simple outward extrapolation boundary condition is used which allows plasma and magnetic field to flow out. The side and top boundary conditions are the same as those used in Fan (2017).

For the initial state, we start with a potential magnetic field extrapolated from the observed photospheric normal magnetic field B_r at 2011–02-14 23:48 UT (Fig. 10(a)), about 1.9 h before the onset of the observed X-class flare. We first numerically relax the MHD solution by driving at the lower boundary with only the random electric field component $\mathbf{E}_h^{\text{random}}$ until the plasma state reaches a statistical equilibrium with a hot corona. The relaxed state is then used as the initial state (with $t = 0$) for the simulation driven with all three electric fields given in the right hand side of Eq. 6 for over 2.8 h. The resulting evolution is described in the next section:

4.2. Result of the boundary-driven simulation

Fig. 12 shows the evolution of the free magnetic energy E_{free} (panel (a)), which is the excess of the total magnetic energy over the corresponding potential field energy, the evolution of the kinetic energy E_k (panel (b)), and the various contributions to the rate of change of the magnetic energy (panel(c)). We see that during the first 1.5 h period, the E_{free} is built up steadily, while the magnetic field is in quasi-equilibrium with the E_k remaining small. The source of the magnetic energy build up is the Poynting flux input at the lower boundary by the driving electric field (black curve in Fig. 12(c)). There are continuous dissipations of the magnetic energy due to the resistive dissipation (red dash-dotted curve in Fig. 12)) and the Lorentz force work (red solid curve in Fig. 12(c)). But the Poynting flux input is in excess of the dissipations and thus there is a net continuous build up of the magnetic energy (blue curve in Fig. 12 (c)), until about $t = 1.5$ hour, when there is a sharp increase of both the Lorentz force work and resistive dissipation,

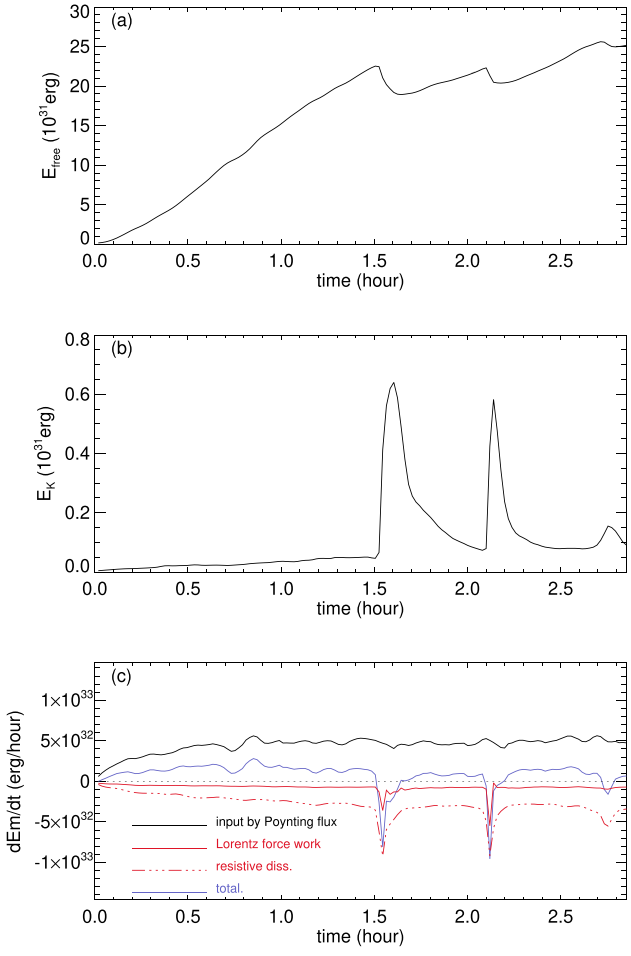

Fig. 12. The evolution of the free magnetic energy E_{free} (a), the evolution of the kinetic energy E_k (b), and the various contributions to the rate of change of the magnetic energy (c), due to the input from the integrated Poynting flux at the boundary (black curve), the total Lorentz force work (red solid curve), the total resistive dissipation (red dash-dotted curve), and the sum of the three (blue curve) which corresponds to the total rate of change of the magnetic energy.

resulting in a sharp release of the magnetic energy and a sharp increase of the kinetic energy. This results in the first eruption. After that, there is another period of steady build up of the magnetic energy for roughly 0.6 h, and then a second abrupt magnetic energy release and eruption develops. The free magnetic energy reaches a peak value of about 2.3×10^{32}erg just before the onset of the first eruption (Fig. 12(a)). This free energy of the pre-eruption magnetic field is consistent with the result obtained in Sun et al. (2012b), who carried out nonlinear force free field extrapolation of the coronal magnetic field of AR 11158 and found that the free magnetic energy reaches a maximum of $\sim 2.6 \times 10^{32}$erg just before the onset of the observed X2.2 flare. We note that it is the twisting electric field that provides the dominant contribution to the Poynting flux and is responsible for the build-up of the free magnetic energy. We have done a separate comparison simulation where we drive the lower boundary with only $\mathbf{E}_h^P$ and $\mathbf{E}_h^{\text{random}}$ in Eq. (6), without the twisting electric field $\mathbf{E}_h^{\text{Tw}}$. We found in that case the Poynting flux input at the lower boundary reduces to about 10% of that in the current case driven with all 3 electric fields, and that there is no build-up of the (free) magnetic energy, with the Poynting flux input balanced by the resistive dissipation and Lorentz force work.

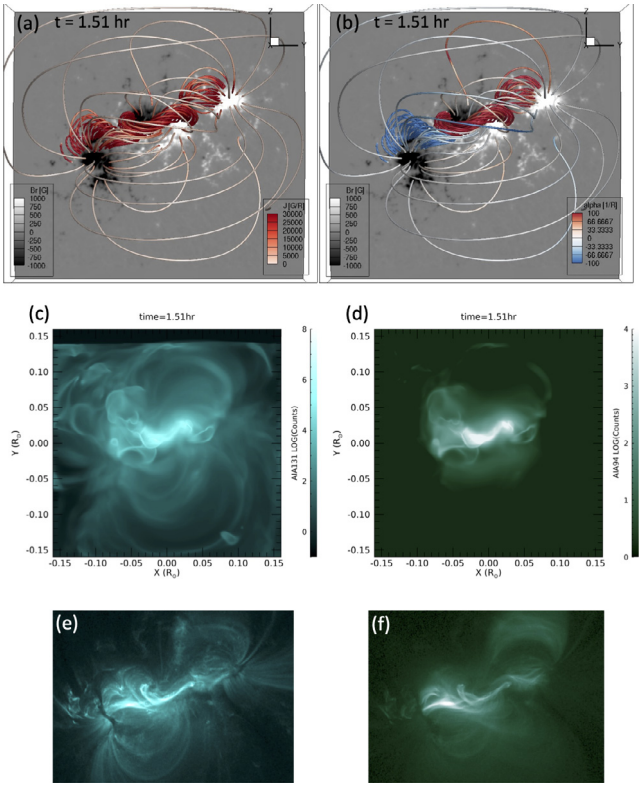

Fig. 13. Top panels show the 3D pre-eruption magnetic field just before the onset of the eruption at $t = 1.51$ hour, with the field lines colored in current density J (a) and in twist rate α (b). The middle row panels show the synthetic AIA 131 Å image (c) and synthetic AIA 94 Å image (d). The bottom panels show in comparison the observed AIA 131 Å image (e) and 94 Å image (f) at 2011-2-15 01:45 UT, about the time of the onset of the X2.2 flare.

Fig. 13 shows the pre-eruption magnetic field just before the onset of the eruption at $t = 1.51$ hour. The top two panels show the 3D magnetic field lines colored with the current density $J = |\nabla \times \mathbf{B}|$ in panel (a) and the twist rate defined as $\alpha \equiv \mathbf{J} \cdot \mathbf{B}/B^2$ in panel (b). Strongly sheared, forward S-shaped (sigmoid) loops with positive (right-handed) twist rates α are found above the central PIL connecting polarities P2, N1 (Fig. 13(b), and see Fig. 10(a) for the identification of the polarity concentrations), and also loops connecting polarities P1, N1 are mainly positive-twisted (right-hand-twisted). However, we find mainly negative-twisted (left-hand-twisted) loops (blue with negative α) connecting P2, N2 polarities, and some higher loops with negative twist connecting P1, N2 polarities. The negative twist is mainly due to the twisting electric field imposed in N2 (due to the observed opposite signs of J_r and B_r), which effectively drives a counter-clockwise rotation and transports negative twist into the corona, opposite to the twisting electric field dominating in the other polarity concentrations that drives positive twist into the corona. We find that the field lines with the strongest current density J (Fig. 13(a)) show morphology in qualitative agreement with the brightening loops in the observed hot channel images of SDO/AIA (Figs. 13(e) and 13(f)). This indicates that the model captures the magnetic field structure of the most non-potential (energized) parts of the field. The synthetic AIA images (Figs. 13(c) and 13(d)) also show some similar emission features as those in the observed ones, i.e. the central forward S-shaped sigmoid emission along the central PIL, and the surrounding large loops connecting the major polarity concentrations. We find that the central sigmoid emission is due to the heating produced by the formation of a strong current layer in the strongly sheared field above the central PIL.

Fig. 14 shows the 3D evolution of a set of magnetic field lines as viewed from 3 different perspectives (top 3 rows) during the first eruption. The field lines are traced from a set of Lagrangian tracer points tracked in the velocity field. We find that the eruption starts with the sudden acceleration of the highly sheared sigmoid field with positive twist above the central PIL (the red field lines in the left column, and the two left panels in the bottom row showing the sudden onset of rise velocity). It is difficult to discern whether this sudden acceleration is triggered by a sudden onset of tether cutting reconnections in the central sigmoid field or that the sigmoid field becomes unstable to the torus instability (e.g. Kliem and Török, 2006).

Fig. 15 shows the distribution of the twist rate α in the central meridional cross-section across the central sigmoid field at the time of the onset of the eruption ($t = 1.51$hour). It can be seen that the top of the sigmoid field region (the patch of positive α indicated by the arrow) is entering above the contour of the decay index $d(\ln B_p)/d(\ln h) = -1.5$, where B_p is the field strength of the corresponding potential field and h denotes the height above the surface. However most of the current of the positive-twisted sig-

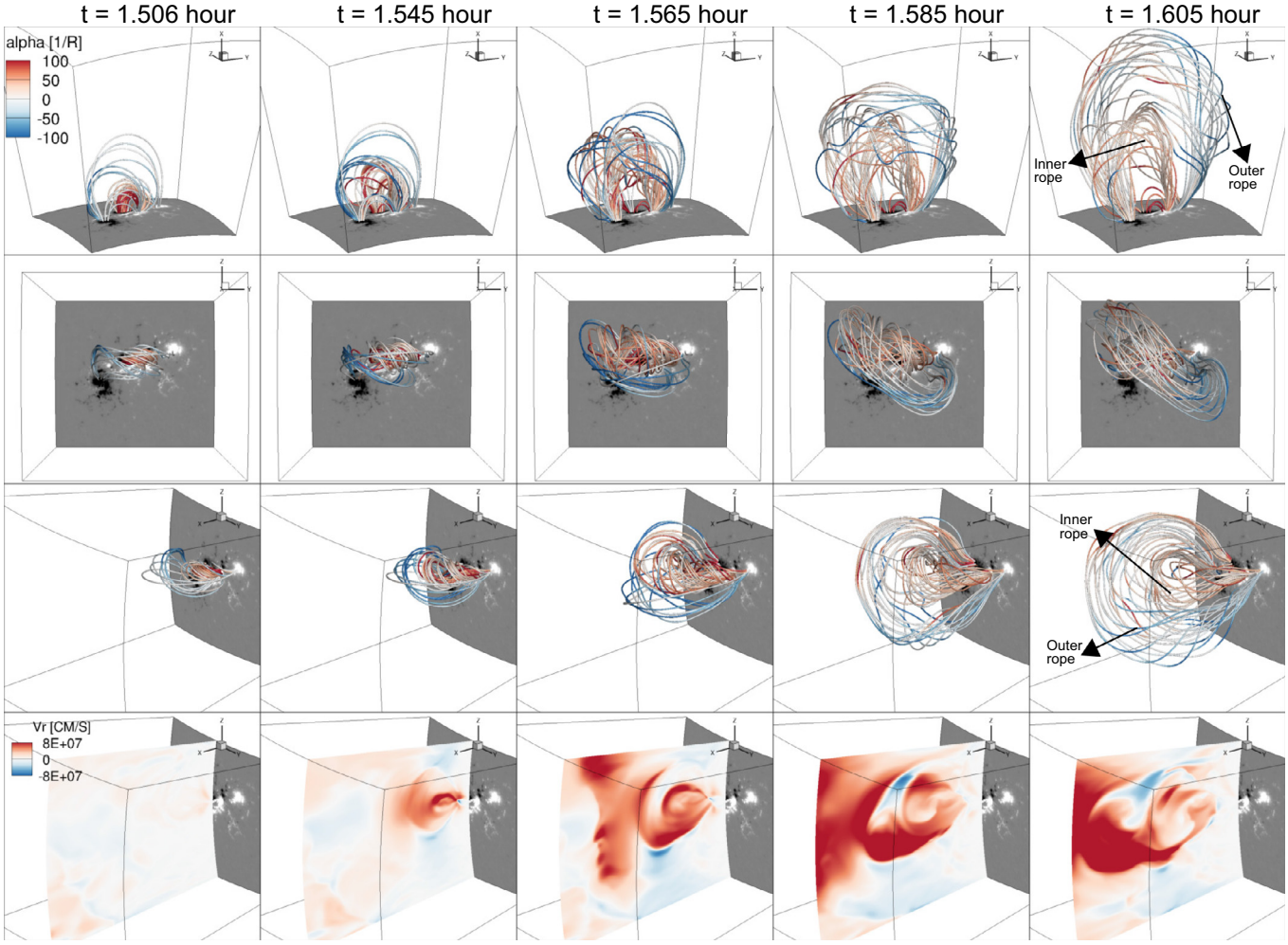

Fig. 14. The top 3 rows show 3D evolution of the erupting magnetic field viewed from 3 different perspectives during the 1st eruption. The field lines are traced from a set of Lagrangian tracer points tracked in the velocity field. The field lines are colored in the twist rate α, whose color bar is shown in the top left panel, with red (blue) corresponding to positive (negative) twist rate. The last row shows the evolution of the radial velocity in the central meridional cross-section, with the same perspective view as the 3rd row. The color bar for the radial velocity is shown in the bottom left panel. The different columns correspond to different time instances with time running from left to right.

moid field remains below the height where the decay index reaches the critical value of -1.5 for the onset of the torus instability (e.g. Kliem and Török, 2006). In the mean time, it can also be seen that a thin current layer (thin layer of strong positive α) is developing in the lower part of the sigmoid field region, which indicates the onset of the tether-cutting reconnection at the current layer may be the trigger of the onset of the eruption. Furthermore, an examination of the field line curvature found that the positive-twisted sigmoidal field over the central PIL (e.g. Figs. 13b) and top left panel of Fig. 14) contains no dipped field lines during the pre-eruption phase, until the onset of the eruption where an erupting magnetic flux rope containing dipped field lines form as a result of the tether-cutting reconnection (see the 2nd and 3rd panels in the top row of Fig. 14). These preliminary results suggest that for this case, the eruption is initiated by the onset of the tether-cutting reconnection which forms a magnetic flux rope that is immediately unstable or out of equilibrium (e.g. Jiang et al., 2021b). More detailed analysis will be carried out in a follow up paper.

As the sigmoid field erupts, it encounters and reconnects with the negative-twisted field above (Fig. 14). Eventually the erupting field consists of an outer flux rope containing mainly negative twist (left-handed twist) and an inner flux rope containing mainly positive twist (right-handed twist) (see the right column of Fig. 14), with the outer flux rope erupting significantly faster, accelerating to a speed of about 800 km/s (see the bottom right panel of Fig. 14), compared to the inner rope which is decelerating.

4.3. Summary of the boundary-driven simulation

We have devised a horizontal electric field ($\mathbf{E}_h$ given in Eq. 6) for driving the lower boundary flux transport in an MHD simulation of AR 11158, based on the observed evolution of the vertical magnetic field B_r and the vertical electric current J_r measured from photosphere vector mag-

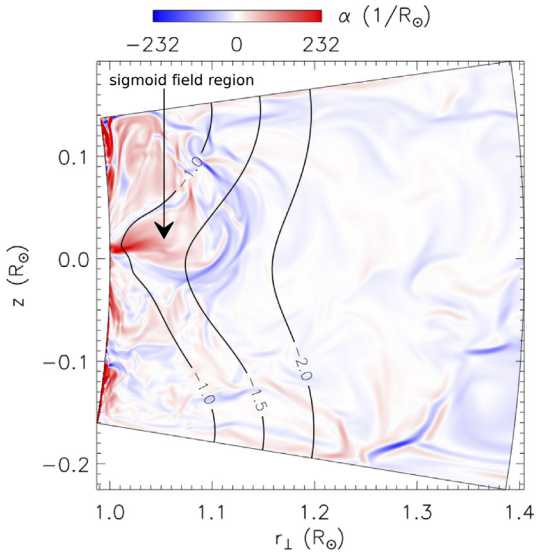

Fig. 15. Distribution of the twist rate α in the central meridional cross-section across the central sigmoid field at the time ($t = 1.51$ hour) of the onset of the first eruption, overlaid with contours of the decay index $d(\ln B_p)/d(\ln h)$, where B_p is the field strength of the corresponding potential field and h denotes the height above the lower boundary surface.

netograms. In particular, the driving electric field includes the horizontal component of the PTD electric field $\mathbf{E}_h^P$ (Eqs. 7 and 8) derived in Fisher et al. (2020) which maintains the observed B_r evolution, combined with a horizontal twisting electric field $\mathbf{E}_h^{\mathrm{Tw}}$ (Eqs. 9 and 11) which continuously transports a horizontal magnetic field with the observed vertical electric current J_r into the domain. In addition, the driving electric field also includes a random electric field $\mathbf{E}_\mathbf{h}^{\mathrm{random}}$ (Eq. 12) that aims to mimic the effect of turbulent convection to drive field line braiding and a consequent background coronal heating.

Our MHD simulation driven with this electric field $\mathbf{E}_h$ at the lower boundary derived from the observed vector magnetograms is found to energize the initial potential field to build up a pre-eruption magnetic field that subsequently produces multiple eruptions. The current carrying, sheared/twisted field lines of the pre-eruption magnetic field show morphology in good qualitative agreement with the brightening loops in the observed SDO/AIA hot channel images at the onset of the observed X2.2 flare. The free magnetic energy built up in the pre-eruption magnetic field reaches a peak value of about 2.3×10^{32}erg just before the onset of the first eruption, which is close to the free energy ($\sim 2.6 \times 10^{32}$erg) obtained based on a non-linear force-free field construction of the pre-eruption field of AR 11158 just before the onset of the X2.2 flare by Sun et al. (2012b). These agreements indicate the potential of using the above observationally derived twisting electric field for data-driven MHD simulations to build up the realistic pre-eruption coronal magnetic field and model its subsequent dynamic eruption to understand the complex magnetic field evolution in the observed event. Specifically, the twisting electric field aims to capture the outcomes of the shearing at the PIL and the rotational/twisting motions at the polarity concentrations as represented by the observed vertical electric current, without having to infer the horizontal motions, which may be difficult (due to the smoothness of the normal magnetic field concentrations) (e.g. Afanasyev et al., 2021). It is a promising way to build up the realistic pre-eruption magnetic field based on the observed vertical electric current, in an accelerated time-scale that is still quasi-static but feasible for the MHD simulations to model self-consistently the transition from the quasi-static phase to the eruption.

5. Investigating the role of flux emergence in initiating coronal mass ejections (Linton Team)

Flux emergence is the primary mechanism for increasing the eruptive capacity of the corona, through the injection of magnetic energy and helicity, and is frequently implicated in triggering filament eruptions and associated flares (see early investigations by Canfield et al., 1974; Heyvaerts et al., 1977). While photospheric motions due to convection and differential rotation can play these roles as well, these mechanisms appear to be irrelevant during the formation of active regions, and are less important than flux emergence during the main phase of active region evolution, when major eruptions typically occur (Schrijver, 2007; Zhang et al., 2008). Surface flows and associated flux cancellation become the dominant factor for energy storage and the triggering of eruptions only during the decay phase of active regions (e.g., Green et al., 2018). Eruptions associated with flux emergence can often be observed during the formation of active regions (e.g., Green et al., 2002; Nindos et al., 2003; Démoulin and Pariat, 2009), indicating that the free magnetic energy or helicity injected into the corona reaches a threshold for eruption while the active-region–producing flux emergence is still ongoing. On the other hand, in already developed source regions, eruptions are often preceded by newly emerging, localized flux, indicating that in such cases flux emergence triggers the eruption of already energized magnetic fields. This was suggested by Feynman and Martin (1995), who found that quiescent filaments were most likely to erupt after new flux emerged in their vicinity in an orientation "favorable for reconnection" with respect to the filament-carrying field (see also Xu et al., 2008). Similarly, flux emergence into strong active region fields is reported to play a critical role in the initiation of many major eruptions (Williams et al., 2005; Schrijver, 2009; Kleint et al., 2015; Chintzoglou et al., 2015). Typically, such flux emergence is brief (~hours; Zhang et al., 2008), but it can be also long-lasting as, for instance, in the 13 December 2006 event (Schrijver et al., 2008). Flux emergence can occur also between active regions, often leading to complex eruptions (e.g., Louis et al., 2015). Flux emergence is apparently an excellent precursor of eruptions. However, many active regions never produce eruptions during their formation,

and localized flux emergence into developed active regions is also regularly observed to occur without eruptions (Zhang et al., 2008). Thus flux emergence is necessary but not sufficient for generating eruptions. Other processes or conditions must be involved, which may not be measurable by present observational platforms. Consequently, numerical simulations are a useful tool for improving our understanding of the association between flux emergence and eruptions. This section will review how MHD simulations have been employed for this purpose, and will review recent progress by team members in initiating eruptions via flux emergence in such simulations.

5.1. Simulations of flux emergence and eruptions: Review

MHD simulations have been widely employed to study the role of flux emergence in eruptions (e.g., Moreno-Insertis and Galsgaard, 2013; Cheung and Isobe, 2014). Such simulations can be divided into two groups, depending on whether they (1) model the emergence of magnetic flux into a non-energized corona and study under which conditions this flux erupts, or whether they (2) model the emergence of magnetic flux into a corona that contains an energized structure and investigate under which conditions this structure erupts. The first scenario corresponds to eruptions from relatively young, isolated active regions (Green et al., 2002), while the second one corresponds to eruptions associated with new, localized flux emergence into developed active regions (Schrijver, 2009) or close to quiescent filaments (Feynman and Martin, 1995).

Simulations of the first group typically incorporate a sub-photospheric domain and "dynamically" model the emergence of a magnetic flux rope from below the surface into a stratified atmosphere that contains a vacuum field or a potential field (e.g., Hood et al., 2012). After the top of the rising rope has breached the photosphere, it expands in the corona, creating an "envelope" field. Within this field a flux rope is formed, either by bodily emergence of the original rope axis (MacTaggart and Hood, 2009) or by reconnection of the emerged sheared fields above the axis (Manchester et al., 2004). It has been shown that such simulations, while being idealized, reproduce the formation of active regions reasonably well (Fan, 2001). Depending on the strength of the emerging flux and/or its interaction with a pre-existing (or envelope) field, the newly formed coronal flux rope may overcome the stabilizing tension of the ambient field and erupt (Archontis and Török, 2008). For eruptive simulations of flux emergence into a vacuum field, evidence for both the torus instability (Kliem and Török, 2006) and tether-cutting reconnection below the rope (Moore et al., 2001) are present, but it has not yet been established which specific eruption mechanism is actually at work in these simulations (Syntelis et al., 2017). In simulations set up to specifically mimic the breakout eruption paradigm of Antiochos et al. (1999), i.e., in which the overlying field is aligned anti-parallel to the emerging flux, so that the two flux systems create a quadrupole configuration, eruptions have been generated for a range of parameters (Galsgaard et al., 2005; Archontis and Török, 2008; Archontis and Hood, 2012; Leake et al., 2014).

Simulations of the second group use localized flux emergence to initiate the eruption of a pre-existing coronal flux rope or arcade. In almost all cases, the sub-photospheric domain is excluded and the flux emergence is modeled "kinematically", that is, formulated analytically (or extracted from dynamic simulations; see Section 5.3) and imposed at the bottom boundary of the simulation domain. This shortcut is required because, in most cases, it is non-trivial (and certainly non-unique) to prescribe the sub-surface morphology of a given energized coronal structure. First calculations of this kind were done for a 2D configuration by Chen and Shibata (2000), who imposed flux emergence below or next to a coronal flux rope and reversed its magnetic orientation for both cases. For a flux emergence orientation "favorable for reconnection" the flux rope erupted, in line with the observations by Feynman and Martin (1995). As proposed by Feynman and Martin (1995), "favorable for reconnection" means that the magnetic fields of the emerging and pre-existing coronal fields form a current sheet, where they can reconnect, between the polarity inversion lines of the two regions. For the "unfavorable" cases, on the other hand, the current sheet forms on the far side of the emerging PIL relative to the pre-existing PIL, and so any ensuing reconnection may have a more stabilizing effect on the pre-existing coronal flux rope. Indeed, for the "unfavorable for reconnection" cases investigated by Chen and Shibata (2000), the flux rope was pulled towards the surface. Ding and Hu (2008) demonstrated that expansion or shrinking of a 2D flux rope occurs even without reconnection, as a result of changing boundary conditions during flux emergence. Using analytical calculations, Lin et al. (2001) showed that the system is more complex – whether the rope erupts or not depends also on parameters such as the strength, location, and area of the flux emergence. This was demonstrated also in subsequent 2D simulations (Dubey et al., 2006; Xu et al., 2008; Zuccarello et al., 2008; Kaneko and Yokoyama, 2014). 3D simulations of this scenario have, until recently, employed only uniformly sheared arcades to model the pre-existing coronal field (Notoya et al., 2007; Kusano et al., 2012). In these simulations, reconnection between the emerging flux and the coronal arcade leads, in some cases, to the formation of a new flux rope that then erupts. In Section 5.3, we describe more recent simulations that used a fully 3D flux-rope model to represent the energized corona.

5.2. Flux emergence and breakout eruptions

To begin our investigation of eruptions initiated by magnetic flux emergence, we studied the emergence of a twisted flux rope into a pre-existing coronal arcade mag-

netic field. This effort was carried out in collaboration with the Antiochos team (see Section 6). The emerging field is centered in each case on the polarity inversion line of the pre-existing field, and the orientation of this emerging field is modified from one simulation to the next to create a variety of combined magnetic field configurations. These configurations varied from an energized quadrupolar field, where the twist field of the emerging flux runs antiparallel to the pre-existing field, to an energized dipolar field, where the emerging twist field and the pre-existing coronal field are parallel, as well as representative configurations between these two limits. The result are reported in Leake et al. (2022) and are summarized below. This investigation was built on earlier simulations of such flux emergence in Leake et al. (2013, 2014), which focused solely on the quadupolar and bipolar configurations. Those studies investigated the effect of the strength of the coronal arcade field as well as the effect of these two relative orientations. Three simulations were run at different coronal field strengths where the emerging azimuthal flux and the coronal arcade field were parallel (dipolar), three where they were anti-parallel (quadrupolar), and one with no coronal field. The simulations with parallel emergence as well as the simulations with emergence into a magnetic field free corona generated a stable coronal flux rope. On the other hand the simulations with antiparallel emergence generated a breakout eruption, as was proposed by Antiochos et al. (1999, see also Section 6), where the quadrupolar field of the breakout eruption was generated by the interaction of the twist field of the emerging flux rope and the pre-existing arcade field, and the energization/ shear field of the breakout was provided by the axial field of the emerging flux rope. Leake et al. (2014) found that reconnection occurred at the interface between the emerging field and the pre-existing field for these antiparallel cases, but that an eruption to the high corona only occurred for the intermediate value of the coronal field strength. They concluded that when the overlying arcade field was too strong relative to the strength of the emerging twist field, it could reconnect away most of that emerging twist field before an eruption went very far. On the other extreme, they concluded that when the overlying arcade field was too weak it did not reconnect away enough of the outer shell of emerging field which tethered the core of the emerging field to the photosphere. This effect that reconnection with an overlying field has in removing the outer shell of emerging flux was demonstrated by Galsgaard et al. (2007), and the critical role that this then plays in allowing the emerging flux to erupt into the high corona was demonstrated by Archontis and Török (2008). The simulations of Leake et al. (2013) and Leake et al. (2014), as well as the new simulations we report on here, were carried out with the visco-resistive magnetohydrodynamic LaRe3D (MHD Lagrangian Remap in 3D, Arber et al., 2001).

In Leake et al. (2022) we improved upon the previous study in a number of ways, the most important being performing a parameter study by varying the relative orientation of the emerging field and the overlying field. This parameter (θ) is defined as the angle between the upper *twist* component of the emerging flux rope and the pre-existing coronal dipole field (which is slightly different than the 3D arcade field used in Leake et al. (2013, 2014)).

The behavior in the simulations with the 8 values of $\theta = [0, 1, 2, 3, 4, 5, 6, 7]\pi/4$ mainly fell into two categories. For simulations such that any amount of *breakout reconnection* between the twist field of the emerging flux rope and the coronal dipole occurred, the partial emergence of the initial flux rope led to a coronal sheared arcade that transitioned into a new flux rope in the corona that appears unstable, as in the eruptive simulations of Leake et al. (2014). This behavior was most obvious for simulations with nearly antiparallel twist versus coronal field, namely those with $\theta = [3, 4, 5]\pi/4$. In addition, this category of simulations also included the values of $\theta = [2, 6]\pi/4$, where the twist and coronal field were orthogonal, but due to writhing of the emergence structure the formation of a breakout current sheet still occurred. The second category consists of those simulations were no breakout reconnection occurred. In these simulations, namely those with $\theta = [0, 1, 7]\pi/4$, a new flux rope was still formed, but it appeared stable. Thus the parameter θ is a potentially useful candidate for predicting eruption in newly emerging ARs. The overall behavior for the simulations with $\theta = [0, 2, 4, 6]$ is shown in Fig. 16.

The use of larger domains in these simulations, compared to previous studies, suggest that all the eruptions were ultimately confined and did not continue to erupt, consistent with changes in the magnetic forces during the eruption, although the effects of boundary conditions cannot be ruled out even for large domains. Further work is needed to determine the forces that drive these eruptions and if they can be sustained.

5.3. Flux emergence and torus instability eruptions

In order to simulate the eruption of pre-existing energized active region fields that is triggered by newly emerging flux, i.e., following the paradigm of the second group of models summarized above, we used the MHD code MAS (“Magnetohydrodynamics Around a Sphere”), developed and maintained at PSI (Mikić et al., 1999; Lionello et al., 2009). MAS uses a 3D spherical grid that can cover the entire corona, allowing one to model both the eruption and propagation of CMEs (e.g., Török et al., 2018). We used the analytical model by Titov et al. (2014, hereafter TDm) to construct coronal configurations that contain a flux rope in a stable equilibrium. We then kinematically emerged a bipolar flux region into these configurations and modeled the resulting evolution. For this kinematic emergence, we used an archived LaRe3D simulation of a flux rope emerging into a field-free corona, similar to the LaRe3D field-free corona simulation discussed above. This method for coupling LaRe3D to MAS has been tested extensively and was successfully applied to model coronal

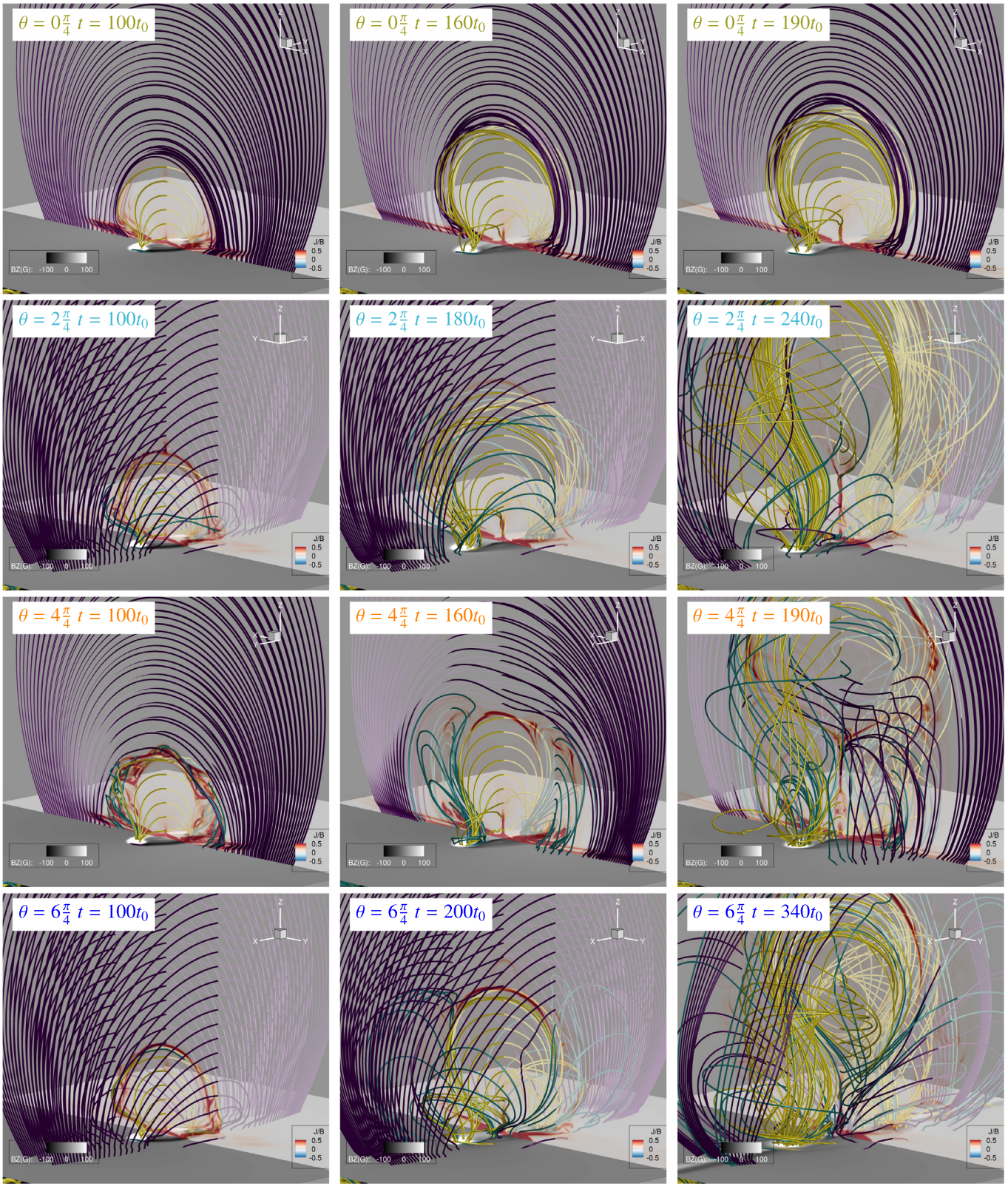

Fig. 16. Snapshots from the parameter study of Leake et al. (2022), where the angle between the right-handed twist of the emerging field and the coronal dipole is $[0, 2, 4, 6]\pi/4$ (top to bottom rows). The coronal dipole is initialized to arch through the corona from the $-x$ side of the emerging region to the $+x$ side of the emerging region (these directions are indicated by the axes in the upper right hand corner of each panel), and the orientation of the emerging region is modified from one simulation to then next to give this changing relative angle. The three columns for each simulation row show successive times after the magnetic field emerges to form a sheared arcade. The fieldlines are colored based on their connectivity. Magenta fieldlines belong to the coronal dipole, yellow fieldlines belong to the emerging and/or erupting flux rope, and cyan lines are initially a result of magnetic reconnection between the two systems at the *breakout* current sheet. Also shown is the photospheric normal field in grayscale and a semi-transparent contour of $|\mathbf{J}|/|\mathbf{B}|$ in the plane normal to the axis of the coronal flux rope that is formed.

jets and their contribution to the solar wind (Török et al., 2016; Lionello et al., 2016).

Our setup extends previous kinematic flux emergence simulations in several respects. (i) We consider a 3D arched coronal flux rope, which introduces line-tying and permits 3D instabilities such as the helical kink and torus. (ii) Our configuration contains a constraining background field that runs perpendicular to the flux-rope axis. In the simulations by Kusano et al. (2012) such a field was not present for the strongly sheared cases, so that the flux rope, once formed, could not be stabilized and was doomed to erupt. (iii) We use boundary conditions extracted from a dynamic flux emergence simulation, which is more realistic than the analytic formulations of flux emergence used in previous simulations.

To carry out this study, we varied the location and magnetic orientation of the emerging flux relative to the pre-existing coronal flux rope and background field. The results are being prepared for publication in Török et al. (2023). Key aspects of these results can be presented with the aid of Figs. 17 and 18, reproduced from Dacie et al. (2018). We focus first on an eruptive case. Fig. 17 shows the flux emergence occurring next to a TDm active region, with an orientation "favorable for reconnection," i.e., a current layer forms between the emerging flux and the TDm rope. Reconnection across this layer, displacing field lines such that they become longer, and the changing boundary condition of the magnetic field (Ding and Hu, 2008) lead to a slow expansion of the stabilizing field overlying the TDm rope. As a result, the rope rises slowly until it reaches the critical height for the onset of the torus instability and erupts, with the eruption driven by both the instability and the "flare" reconnection below the flux rope. This result supports the results by Feynman and Martin (1995) and Chen and Shibata (2000).

However, we then found that when we emerge flux closer to the TDm active region, as shown in Fig. 18, the axial currents in the TDm rope and in the emerging flux (which

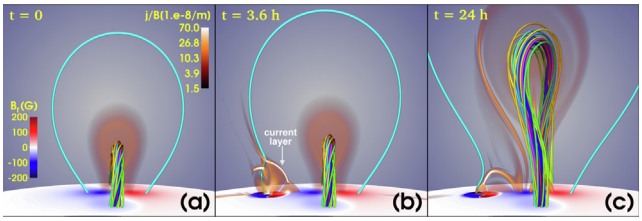

Fig. 17. Kinematic emergence of a twisted flux region into a pre-existing TDm coronal field (panel a), where the emergence is at an intermediate distance from the TDm flux rope (panel b). This setup represents a "favorable" configuration for eruption, based on the observational studies of Feynman and Martin (1995), namely, the orientation is such that a reconnecting current sheet can (and does) form between the emerging and pre-existing regions. Analysis of the simulation shows that the outer magnetic fluxes of both the emerging and pre-existing regions reconnect (see cyan field line), reducing the strength of the confining overlying field of the TDm flux rope and allowing it to erupt (panel c). Reproduced from Dacie et al. (2018), Fig. 7.

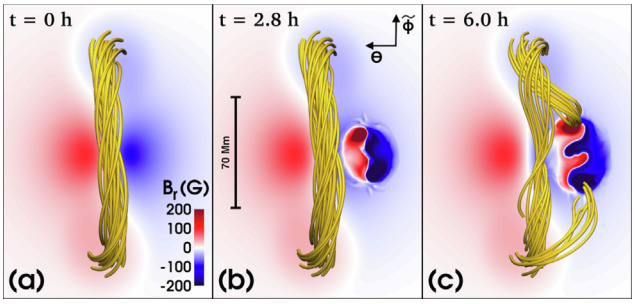

Fig. 18. Kinematic emergence of a twisted flux region into a pre-existing TDm coronal field (panel a), where the emergence is relatively close to the TDm flux rope (panel b). While this configuration is also "favorable" for eruption based on the observational studies of Feynman and Martin (1995), it does not erupt. Analysis of the simulations shows that these regions are so close together that the axial fields reconnect with each other, causing the TDm flux rope to collapse (panel c). Reproduced from Dacie et al. (2018), Fig. 6.

are co-aligned in both Fig. 17 and 18) start to attract each other. Even though the reconnection is now initially more efficient at expanding the overlying flux, the attraction of the currents counteracts the rise of the TDm rope and no eruption takes place, contrary to the findings of Feynman and Martin (1995) and Chen and Shibata (2000). In Török et al. (2023) we propose that this current attraction and subsequent "rope-rope" reconnection is similar to the slingshot reconnection reported in Linton et al. (2001) for flux ropes with parallel axial magnetic field and antiparallel axial current, as is the case here.

Török et al. (2023) extends this study to smaller and larger distances between the emerging and pre-existing flux ropes and, critically, extends it to cases with flux emergence "unfavorable for reconnection." Again, we found that this "unfavorable" classification does help to predict a lack of eruption for certain distances between the two systems, but that for other (in particular closer) distances, an eruption can still happen. In this case, it appears that reconnection between the two systems is not the key factor, but rather a current-channel repulsion between the two systems. This indicates that the orientation alone is not sufficient to predict eruption, but that at a minimum both the distance of the emergence from the pre-existing flux rope as well as its orientation relative to that flux rope play a fundamental role in whether the configuration will generate an eruption.

6. The role of magnetic reconnection in the onset of solar eruptions (Antiochos Team)

A major challenge to understanding CME onset is that the energy release in a CME/eruptive flare generally exhibits several phases: an early slow rise, followed by a transition to a fast "explosive" acceleration/heating phase, finally followed by a long less-energetic decay phase that, nonetheless, can release significant amounts of energy.

Therefore, there is not a single onset, but a sequence of transitions; and this sequence is observed to be essentially the same for most events, especially the large ones.

We have long argued that magnetic reconnection can account for all the observed phases of solar eruptions (Antiochos et al., 1999; Karpen et al., 2012; Wyper et al., 2017). Fig. 19, from Karpen et al. (2012), which shows the time evolution of magnetic and kinetic energy for an ultra-high resolution 2.5D simulation, demonstrates the basic result. The magnetic system consisted of the initially current-free axisymmetric multipolar field of Antiochos et al. (1999) that had a central polarity inversion line (PIL) coincident with the equator. The system was energized by applying a slow boundary shear flow localized about the PIL. This driving flow resulted in the gradual rise in magnetic free energy visible in Fig. 19, along with the minuscule initial rise in kinetic energy. The addition of the magnetic stress led to the formation of a current sheet at the overlying coronal separatrix and null, so that eventually "breakout reconnection" set in there. This produced the first jump in kinetic energy visible in Fig. 19 at time $t \approx 6 \times 10^4$ s.

We identified this onset of breakout reconnection as the onset of eruption in that, once it begins, eruption is inevitable. However, if this is the only reconnection that occurs, then eruption will be slow, because the end state of the system will contain a vertical current sheet that extends down to low altitudes. Reconnection within this current sheet, the so-called flare reconnection, allows the field to relax rapidly toward a nearly potential state while accelerating the CME outward. Our results showed that the onset of explosive energy release in solar eruptive events was due to the onset of fast flare reconnection (Karpen et al., 2012).

The results above are compelling, but they are only for a 2.5D system, which of course is artificial. A true CME/flare is never 2D. Therefore, as part of this LWS Focused Science Team, we extended our study of the role of reconnection in CME onset to the fully 3D case. This study was highly challenging, because it required ultra-high numerical resolution of the reconnecting current sheets, both breakout and flare. For these studies, the adaptive mesh refinement capabilities of our Adaptively Refined Mhd Solver (ARMS) were indispensable. Although we simulated a system that went out to $30R_\odot$, the resolution in the flare current sheet went down to about 300 km. Fig. 20 shows the initial state of our system, which consisted of a potential field due to dipole sources below the photosphere. Note that in order to make the analysis easier, the initial field was chosen so as to be antisymmetric about the equator, so that the eventual flare current sheet would lie along the equatorial plane.

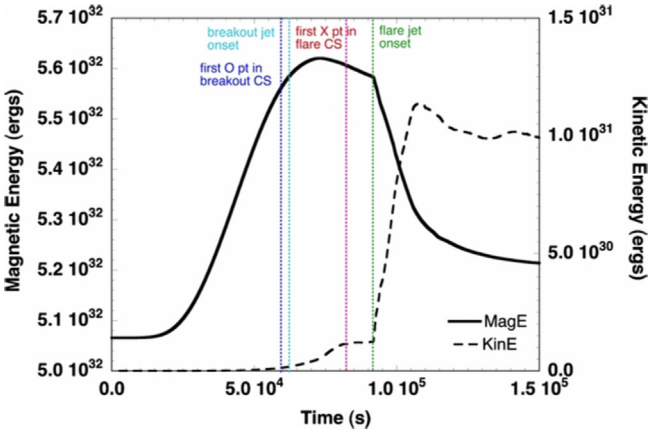

Fig. 19. Volume-integrated total kinetic and magnetic energies vs. time. Vertical lines denote important milestones in the CME/flare evolution. Adapted from Karpen et al. (2012).

6.1. STatistical InjecTion of Condensed Helicity (STITCH)

A key issue for all models of CME onset is the buildup of the free energy that leads to eruption, that is to say, the formation of the filament channel (Patsourakos et al., 2020). Three methods have long been used: flux emergence (e.g., Section 5 and Galsgaard et al., 2005; Archontis and Török, 2008; Leake et al., 2014; Syntelis et al., 2017), photospheric boundary flows either with (e.g. Linker et al., 2003; Amari et al., 2010; Aulanier et al., 2010) or without (e.g. Antiochos et al., 1999; Lynch et al., 2008) flux cancellation, and flux-rope insertion (e.g., van Ballegooijen, 2004; Titov et al., 2014). Flux emergence is a robust, physically self-consistent method for filament channel formation (Leake et al., 2022); however, it is difficult to use for event studies, because it inherently allows for little control over

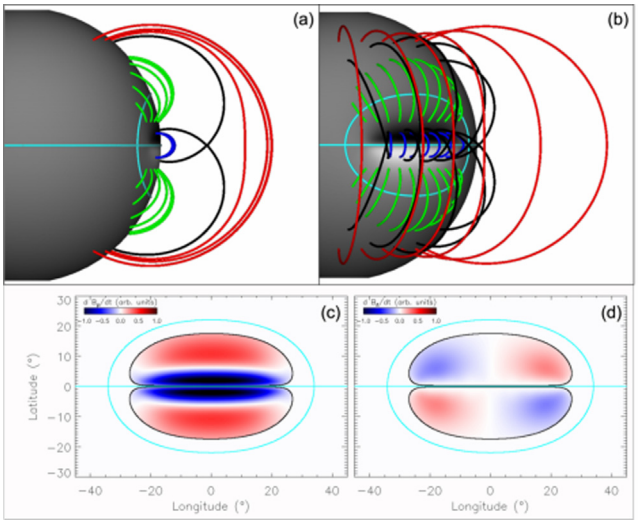

Fig. 20. (a,b) Initial magnetic configuration for the fully three-dimensional eruptive flare calculation. White (black) shading at the inner boundary corresponds to positive (negative) normal polarity. Polarity inversion lines (PILs) are indicated by cyan curves. Four distinct flux regions are indicated in blue, green, and red (northern and southern sets of green field lines represent distinct flux regions). (c,d) Profile of tangential flux injected by the STITCH method (see text for details) at the inner radial boundary, normalized to 0.58 G s^{-1}. The B_ϕ component is shown in (c) and the B_θ component in (d). Adapted from Dahlin et al. (2022a).

the evolution of the photospheric flux. The other two methods are tantamount to assuming particular boundary conditions and/or initial conditions, which have not been proven to capture self-consistently the actual photosphere-corona interaction.

More recently, Antiochos (2013) proposed a mechanism for filament channel formation due to injection of net helicity into the corona by photospheric convective flows including granulation and supergranulation. A system that supports ubiquitous reconnection across numerous small-scale current sheets, as postulated by the well established nanoflare coronal-heating model (Parker, 1987; Klimchuk, 2006), will transfer the helicity to ever-larger scales through an inverse cascade (Berger, 1984; Berger and Oliger, 1984; Finn and Antonsen, 1985; Biskamp, 1993). In the solar context, this cascade "condenses" the small-scale twist injected within a unipolar region at its PIL, where it takes the form of a large-scale shear. Rigorous exploration of the theory via MHD simulations has shown that it forms filament-channel structures whose properties are consistent with solar observations (Zhao et al., 2015; Knizhnik et al., 2015; Knizhnik et al., 2017a; Knizhnik et al., 2017b; Knizhnik et al., 2018) and whose evolution can generate a fast CME accompanied by an eruptive flare (Dahlin et al., 2019). Other work has demonstrated that helicity condensation generates filament channels in accord with the otherwise inexplicable chirality patterns observed on the Sun (Mackay et al., 2014; Mackay et al., 2018).

A major difficulty with the helicity-condensation calculations, however, is that they are computationally very intensive: all of the convective flows, as well as the small-scale reconnection dynamics, that drive the helicity cascade must be resolved. In particular, it would be computationally prohibitive to attempt to capture the long time scales required for the buildup of non-active-region filament channels by helicity condensation. Overlapping the convective flows and the PILs would trigger substantial small-scale diffusion across the resultant grid-scale structures, and this must be avoided when driving highly complex magnetic configurations typical of solar eruptive events. Helicity condensation simulations have shown, however, that the filament channels generated are relatively insensitive to the specific mechanism or spatial scale of the injected helicity (Knizhnik et al., 2017a; Knizhnik et al., 2019). The shear always will be transferred to the PILs, so long as sufficiently complex, turbulent dynamics accompanies a net injection of helicity of one sign or the other. Consequently, while understanding nanoflare-type coronal heating requires resolving the small-scale reconnection processes, the large-scale filament-channel formation and energy buildup ultimately are insensitive to the details of the helicity injection and cascade.

These considerations motivated us to develop a subgrid-scale model, STITCH (STatistical InjecTion of Condensed Helicity), for the helicity condensation process (Mackay et al., 2014; Mackay et al., 2018). STITCH eliminates the small-scale structures and dynamics that accrue to employing the full MHD treatment. This makes it far more efficient numerically in calculations and in memory, as it requires much lower temporal cadence and spatial resolution. The STITCH term, expressed below, is simple to implement and ease to use. Our approach can be applied readily to complex surface-flux distributions that include multiple, meandering PILs because it is so flexible.

Presented by us originally in Mackay et al. (2014), STITCH is a subgrid-scale model expressed in a single new term that appears in the MHD induction equation,

$$\frac{\partial \mathbf{B}}{\partial t} = \nabla \times \frac{\partial \mathbf{A}_s}{\partial t} = -\nabla \times \nabla_s(\zeta B_n). \tag{13}$$

$\mathbf{B}$ is the magnetic field, $\mathbf{A}$ is the vector potential, t is time, subscripts s and n denote components parallel and normal to the surface, respectively, and the parameter ζ characterizes the vortical flows,

$$\zeta = \langle \ell^2 \omega_l \rangle / 2. \tag{14}$$

Here ℓ and ω_l are the radius and angular rotation rate of the cells, respectively, and angle brackets denote a local space/time average. Clearly, the rate of change of $\mathbf{B}$ in Eq. 13 is strongest where the product ζB_n varies most rapidly. This occurs primarily in the vicinity of the PILs, which are the boundaries of the flux systems.

The STITCH term has two key properties. It keeps the magnetic field divergence-free,

$$\frac{\partial}{\partial t} \nabla \cdot \mathbf{B} = -\nabla \cdot [\nabla \times \nabla_s(\zeta B_n)] = 0, \tag{15}$$

everywhere that ζB_n is mathematically smooth (i.e., differentiable). It also preserves the normal magnetic field component, B_n, while injecting twist flux into the corona,

$$\frac{\partial B_n}{\partial t} = -\hat{\mathbf{n}} \cdot \nabla \times \nabla_s(\zeta B_n) = -\hat{\mathbf{n}} \cdot \nabla_s \times \nabla_s(\zeta B_n) \equiv 0. \tag{16}$$

The horizontal field component, $\mathbf{B}_s$, changes according to

$$\frac{\partial \mathbf{B}_s}{\partial t} = -\nabla_n \times \nabla_s(\zeta B_n) = +\nabla_s \times \nabla_n(\zeta B_n). \tag{17}$$

This expression has exactly the same form as that employed to generate randomized twists, with coefficient ξ, which inject no net helicity (Eq. 12) as described in Section 4.1. In contrast, here our coefficient ζ is smooth and everywhere single-signed, so that it injects large-scale magnetic shear.

6.2. STITCH validation

In order to validate that STITCH captures the essence of full helicity-condensation (FHC) dynamics, we performed a numerical simulation of an eruption in a system that was driven by the two processes in turn. The FHC system was simulated by Dahlin et al. (2019) and is described in detail there. The magnetic field consisted of an embedded-bipole topology with a large elliptical PIL in the northern hemisphere.

In the FHC case, we drove the system using 107 tessellated, vortical, B_r-conserving cellular flows within the minority-polarity region. The resulting rates at which horizontal magnetic field components were generated by the motions are shown in Fig. 21a. We ramped up the flows sinusoidally over 1,000 s, then held them fixed at a maximum speed $|V_\perp| \approx 50$ km s^{-1}, which is both subsonic and highly sub-Alfvénic. The magnetic field was line-tied at rest ($\mathbf{V}_\perp = 0$) across the remainder of the surface for the full duration of the simulation. The resultant gradual energy-buildup phase required about 90,000 s of elapsed physical time.

In the STITCH case, we adopted a uniform parameter value, $\zeta_0 = 1.4 \times 10^{16}$ cm^2 s^{-1}, within the minority-polarity region, and a zero value everywhere else. The resulting rates of horizontal magnetic-field injection peaked at about 1 G s^{-1}, as shown in Fig. 21b. To achieve a smooth start-up, we ramped up the flux injection sinusoidally over 1,000 s. In this STITCH calculation, the magnetic field was line-tied at rest ($\mathbf{V}_\perp = 0$) over the entire surface for the full duration of the simulation. The resultant energy-buildup phase was much shorter with STITCH, requiring only about 6,000 s of elapsed physical time.

Snapshots of the filament-channel formation (left) and eruption (right) phases are shown for the FHC (top) and STITCH (bottom) cases in Fig. 22. Highly sheared, low-lying orange field lines – the longest of which stretch more than halfway along the PIL – are restrained by weakly sheared, high-lying red field lines in both cases (Fig. 22a, c). This configuration agrees well with photospheric vector magnetograms, which show that the shear zone is highly localized near the PIL and that the angle that the shear field makes with the PIL can be as low as 15° (Hagyard et al., 1984). In each case, the filament-channel formation phase is approximately two-thirds complete at the time of these snapshots. The entire filament channel subsequently erupts, ejecting a quasi-circular filament at a maximum speed $V > 1000$ km s^{-1} shown by the dark red shading

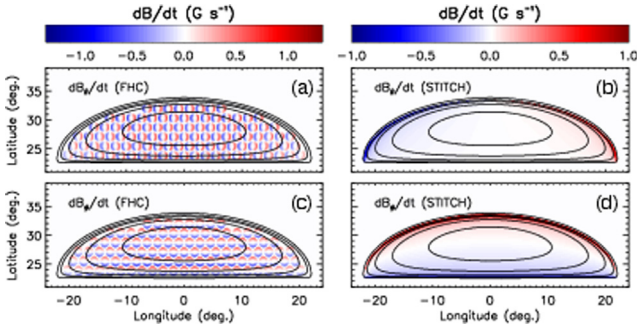

Fig. 21. Helicity injection for the idealized embedded-bipole configuration. (Left) Horizontal components of magnetic field, $\mathbf{B}_s$, that are induced by a horizontal velocity field, $\mathbf{V}_s$, imposed on the boundary to drive the full helicity condensation (FHC) case. (Right) Horizontal components of magnetic field, $\mathbf{B}_s$, that are injected directly into the corona just above the boundary to drive the STITCH case, here with uniform ζ. Black contours indicate radial magnetic field values B_r = [-50,-40,-30,-20,-10,0] G. Adapted from Dahlin et al. (2022b).

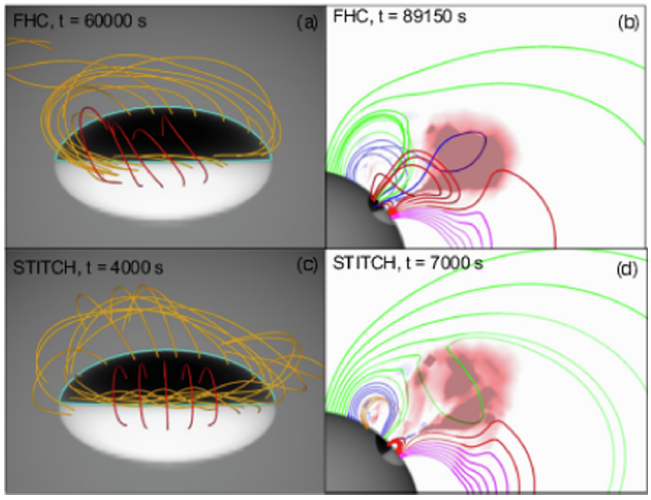

Fig. 22. Filament-channel formation (left) and eruption (right) for full helicity condensation (FHC; top) and STITCH (bottom) with uniform ζ. Magnetic field lines are colored according to whether they close entirely within the active region (red), between the active region and the background magnetic field (blue and magenta), or entirely within the background field (green). Orange lines show the filament-channel field. Color shading in the plane of the sky (right) shows radial velocity V_r. Adapted from Dahlin et al. (2022b).

against the plane of the sky (Fig. 22b,d). In each case, the kinetic energy is near its maximum value at the time of these snapshots.

These results demonstrate that the STITCH formalism effectively captures the physics of helicity condensation and can be used to replace the complex multi-cell convective driving of FHC (see Dahlin et al., 2022b, for a detailed comparison of the two cases). Consequently, STITCH provides substantial utility for physics-based modeling of CMEs and, potentially, great promise as an operational tool for future space-weather prediction capabilities. It possesses several efficiencies and advantages compared to full MHD calculations of the formation and eruption of filament channels:

- Easily implemented in MHD models
- Easily applied to realistic, complex PILs
- Facilitates event modeling by energizing the system without disturbing the normal magnetic field component
- Reduces computational expense by using fast, sub-Alfvénic (flux-injection) driving rather than slow, subsonic (vortical-flow) driving
- Reduces computational expense by using coarse grids that need not resolve small-scale vortical flows and current sheets
- Eliminates complex small-scale structure and dynamics that can obscure the essential large-scale evolution

6.3. Eruption onset and dynamics

With the vast improvement in computational efficiency afforded by STITCH, we were able to perform an ultra-

high-resolution simulation of an eruption in the system shown in Fig. 20. The flux injected by the STITCH driving is shown in the bottom two panels of Fig. 20. The adaptive-mesh capabilities of ARMS allowed us to resolve selectively the important fine-scale structure in the electric current. Refinement and derefinement criteria were based on the local ratio of the grid spacing to the current–density spatial scale (as in Karpen et al., 2012; Masson et al., 2013; Masson et al., 2019). Further details of the simulation are described by Dahlin et al. (2022a).

The energy buildup leading to eruption onset, via the formation and evolution of the filament channel, is illustrated in Fig. 23. Representative filament-channel field lines (a-d) are shown along with $\phi = 0$ cuts of B_ϕ (e-h) and normalized current–density magnitude $|\mathbf{J}|R_s/c$ (i-l). Initially the magnetic field lines run perpendicular to the PIL, forming an unsheared arcade, as the field is potential (current-free) at the outset. The low-lying orange field lines increasingly become stretched along the ϕ direction as shear flux is injected into the system. The high-lying red field lines are more weakly sheared, primarily expanding upward and sideways. Early on, the shear is weak and the overlying flux expands negligibly; hence, the shear-flux distribution at this stage (Fig. 23f) directly reflects the gradients in the STITCH shear injection. This creates a strong current shell coincident with the boundary of the sheared region, as seen in Fig. 23j. The shear flux expands outward as the driving continues, and it eventually takes on an inverted-teardrop shape (Fig. 23g). This expansion causes the shear field to decrease in magnitude (see Fig. 24), so the current shell fades in intensity, but deep within the shear region, a new vertical current sheet forms (Fig. 23k). The current-sheet formation occurs late in the evolution, after $t = 10,000$ s,

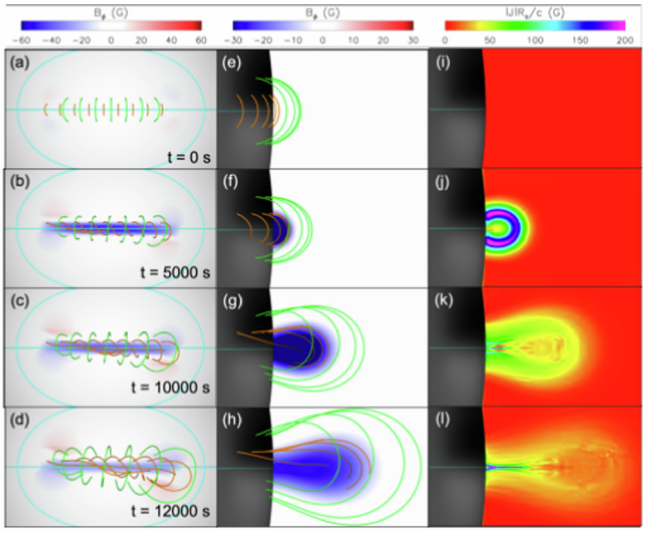

Fig. 23. Energy buildup phase of the eruptive flare. (a-d) Overhead view of the filament channel, with two sets of magnetic field lines corresponding to the low-lying (orange) filament channel and overlying (green) arcade loops. Blue-to-red shading indicates B_ϕ at the inner boundary. (e-h) $\phi = 0$ cut of B_ϕ (shear/guide field), with the same sets of field lines shown in (a-d). (i-l) $\phi = 0$ cut of $|\mathbf{J}|R_s/c$ (normalized current-density magnitude; R_s is the solar radius). Adapted from Dahlin et al. (2022a).

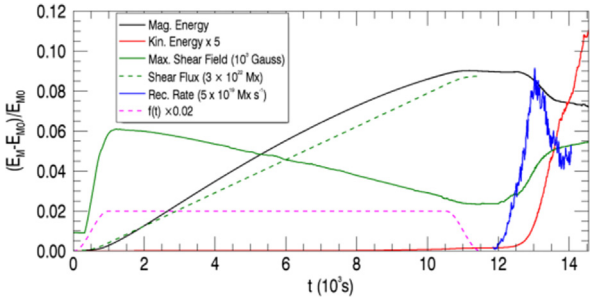

Fig. 24. Global energetics during the energy buildup and the eruptive flare. The dashed magenta curve, $f(t)$, indicates the temporal profile of shear injection, solid (dashed) green the maximum strength (total flux) of the shear field, black the normalized magnetic free energy, red the normalized kinetic energy, and blue the rate of reconnected flux. E_M denotes the total magnetic energy and E_{M0} its initial value. Adapted from Dahlin et al. (2022a).

shortly before the driving is stopped. We point out that, by this time, the breakout reconnection already is well underway and the outward expansion is slowly accelerating, but it is not yet explosive.

These fully 3D results match very well those of the 2.5D case; both the filament-channel (energy buildup) and current-sheet formation processes are quite similar. Several global quantities that characterize the CME/eruptive flare are plotted versus time in Fig. 24. The gradual phase of energy buildup lasts until $t = 11,500$ s; the impulsive phase of energy release due to eruptive-flare onset begins at $t \approx 12,000$ s. The total magnetic free energy in the system (solid black curve) closely tracks the total shear flux in the filament channel (dashed green curve). Much like our findings in a previous eruptive-flare study (Dahlin et al., 2019), the maximum shear-field strength (solid green curve) rises rapidly to a peak early in the energy-buildup phase; thereafter, it decreases gradually until eruption onset. This evolution results from an increase in the cross-sectional area of the filament channel, as the shear flux expands upward and outward in response to the buildup of internal magnetic pressure. Such behavior is predicted by the Aly-Sturrock (Aly, 1984; Sturrock, 1991) principle: they argued that, in both the minimum-energy (closed potential) and maximum-energy (fully open) states, the shear field must vanish. Consequently, the strength of the shear-field component must peak somewhere between those energy extrema.

The time dependence of the reconnection rate $d\Phi_{rec}/dt$, where Φ_{rec} is the reconnected flux (solid blue curve, Fig. 24), reveals the rapid onset and fast dynamics of the eruptive flare. We calculated the rate by tracking changes of the magnetic-field connectivity within the erupting region at high cadence (as in Dahlin et al., 2019). The onset of fast reconnection clearly precedes the rapid conversion of magnetic energy into kinetic energy, as we have noted in our previous studies (Karpen et al., 2012; Dahlin et al., 2019). (Our results also are consistent with an analytical model that relates the reconnected flux to the CME

acceleration; see Welsch, 2018). Following flare onset, the maximum shear-field strength in our simulation begins to increases again; this is due to retraction and compression of flare loops that retain a portion of the shear flux. We emphasize, however, that the majority (approximately 80%) of the shear flux in the filament channel is ejected by the eruption, thereby allowing the system to relax back toward a nearly potential state. The reduction in the magnetic free energy is relatively small because the erupting flux rope, which contains most of the shear flux, remains within the simulation domain for the entire time shown.

6.4. Conclusions

The results presented here have critical implications for understanding CME onset. We have noted in Fig. 24 that the fast flare reconnection turns on *before* eruption onset. In fact, the explosive acceleration of the CME is due to this fast reconnection. An important point is that the reconnection rate (blue curve in Fig. 24) quickly reaches a maximum and starts to turn down, but the kinetic energy keeps rising. This indicates that the reconnection is truly the onset mechanism: once the eruption is well underway, it can be self-sustaining due to the expansion of the CME flux rope.

We find no evidence of ideal instability, either kink or torus, in our simulation. On the other hand, our filament channel has no twist, so such an instability would not be expected. The key point, however, is that the process of helicity condensation, coupled with reconnection, naturally results in a fast eruption without the need to invoke any particular parameters for the active-region system. We conclude, therefore, that reconnection is the mechanism for CME onset: the breakout reconnection enables the flare current sheet to form, and the reconnection in the flare current sheet is the mechanism for CME onset. The same conclusion has been reached from detailed simulations presented in Section 5 of the flux-emergence mechanism for filament channel formation (Leake et al., 2014; Leake et al., 2022). This understanding now needs to be tested against rigorous simulations of observed events.

We expect that STITCH will prove to be indispensable for performing such event studies. An important finding from our work is that the STITCH formalism is a robust and flexible procedure for building up the free energy that leads to eruption. STITCH is one of our primary deliverables for this LWS FST, and it may well turn out to be a major contribution of LWS science toward advances in space weather capabilities.

7. Observational and modeling case studies of CME-related reconnection (Lynch Team)

7.1. Observations and modeling of flare reconnection during the eruption of an extended mid-latitude filament

There is a quantitative relationship between the reconnection flux in the corona and the magnetic flux swept by the flare ribbons (Forbes and Priest, 1983; Qiu et al., 2007; Kazachenko et al., 2017). Magnetic reconnection rapidly adds poloidal magnetic flux to the CME structure during the eruption process, resulting in the formation of a coherent, twisted flux rope (e.g., Lynch et al., 2009; Welsch, 2018; Jiang et al., 2021a; Jiang et al., 2021b; Yan et al., 2022), largely in agreement with remote-sensing and in situ CME observations (e.g. Bothmer and Schwenn, 1998; Vourlidas et al., 2013; Hu et al., 2014). In addition to the connection between eruptive flare reconnection and CME acceleration (Jing et al., 2005; Qiu et al., 2010), properties of the magnetic field—handedness, orientation, and magnetic flux content—are routinely used to make the CME–ICME connection (e.g. Palmerio et al., 2017; Gopalswamy et al., 2017; Gopalswamy et al., 2018).

The Lynch team, in collaboration with the Antiochos team (see Section 6), ran a data-inspired MHD simulation of the 2015 July 9–10 mid-latitude filament eruption which eventually impacted Earth on 2015 July 13 with a flux rope ICME morphology, measured in situ by the Wind and ACE spacecraft (Lynch et al., 2021). In this section, we review some features of the "eruptive flare reconnection" that occurred during the filament eruption and the resulting CME morphology in the extended solar corona.

Fig. 25(a) shows the $\partial B_\phi/\partial t$ component of the STITCH profile (see Section 6.1; also Dahlin et al., 2022a; Dahlin et al., 2022b) for the filament channel energization (left panel) and the global magnetic free energy (ΔE_M) and kinetic energy (ΔE_K) evolution during the simulation's filament energization phase and the activation and eruption phase (right panel). The yellow shaded region, $175 \lesssim t \lesssim 184$ hr, denotes the "impulsive" phase of the eruption where 4.90×10^{31} erg of the magnetic free energy that was stored in the sheared filament channel fields is rapidly released. During this interval, approximately 70% of the magnetic free energy release is converted into the kinetic energy of the CME eruption.

Fig. 25(b), left panel, shows a calculation of the cumulative flare ribbon area swept out during the MHD simulation's filament eruption, color-coded by reconnection time. We use a large change in field line length ($\Delta L \leqslant -2R_\odot$) between output files as a proxy for whether the field line footpoint has experienced reconnection. Fig. 25(b), upper and lower right panels, show a portion of the HMI $B_{\rm LOS}$ full disk magnetogram during the time of the modeled event with the red contour showing the spatial extent of the observed flare ribbon area and the color shading showing the time evolution of the ribbon area structure, respectively. While uncertainties in the HMI magnetogram measurements can become significant as one approaches the limb, we note that the majority of the east–west portion of the filament channel PIL occurs at ~45° south where $B_{\rm LOS}$ and the average magnetic flux over the extended ribbon area are reasonably well resolved. In both the observations and the simulation results, the flare reconnection starts near the east limb and rapidly travels

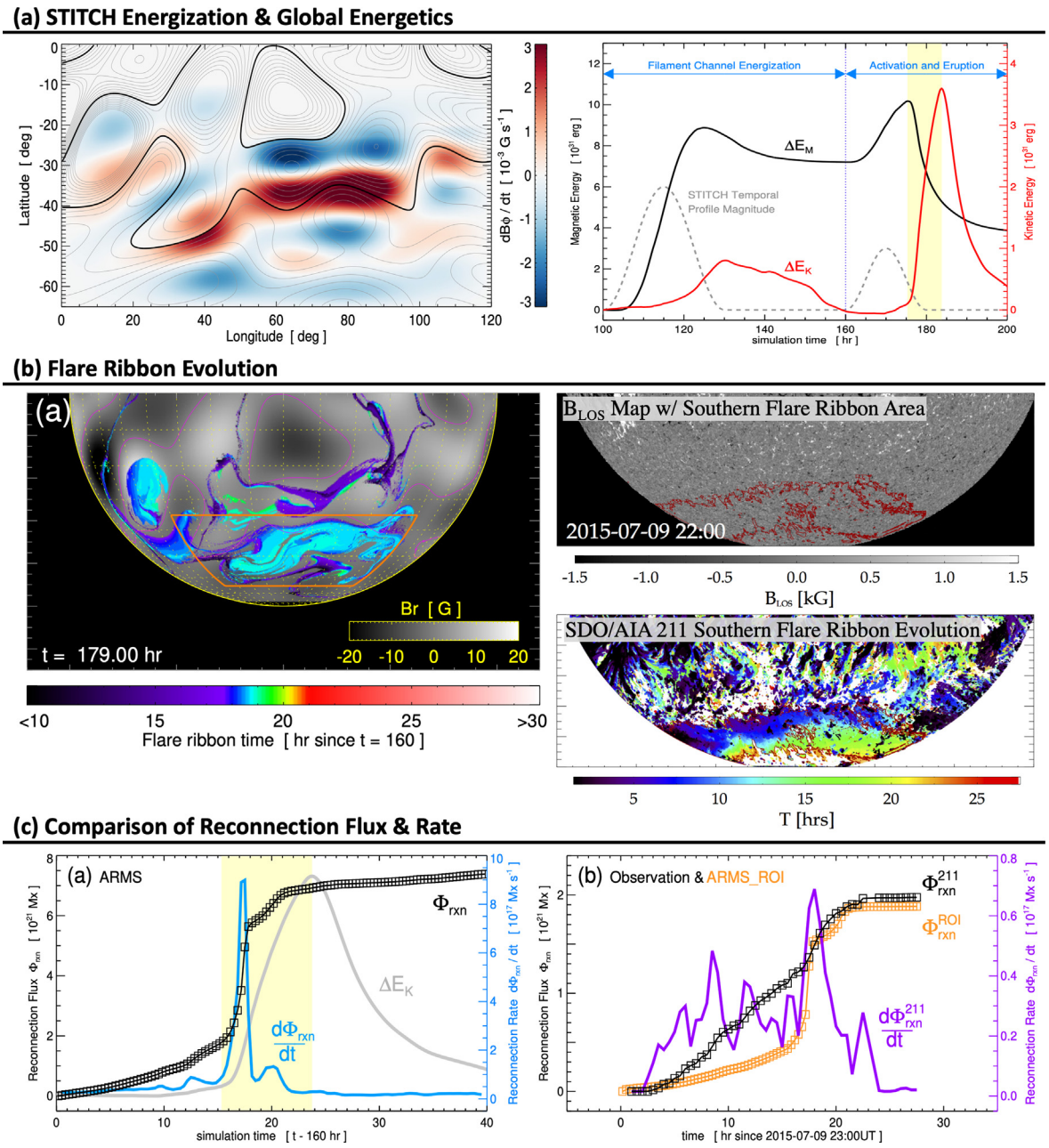

Fig. 25. (a) Left panel: $\partial B_\phi/\partial t$ component of the STITCH energization used to create the mid-latitude filament channel. Right panel: Global magnetic energy (ΔE_M) and kinetic energy (ΔE_K) evolution during the filament channel energization phase and activation/eruption phase. (b) Left panel: Flare ribbon area representing reconnection flux in the MHD simulation. Right panels: Magnetic field and flare ribbon area from SDO/HMI and AIA observations for the 2015 July 9–10 filament eruption. (c) Left panel: Simulation reconnection flux (Φ_{rxn}) and reconnection rate ($d\Phi_{rxn}/dt$) derived from the flare ribbon area. Right panel: Comparison between observed reconnection flux (Φ^{211}_{rxn}) and the simulation's reconnection flux in an equivalent "region of interest" (Φ^{ROI}_{rxn}). Adapted from Lynch et al. (2021).

along the PIL toward the west, as in the "zipper" configuration described by Priest and Longcope (2017, 2020), followed by the slower "main phase" of sweeping away from the PIL. The flare reconnection imparts poloidal/twist flux all along the erupting sheared field structure. The magnetic complexity of the active region near the east limb causes the initial eruptive flare reconnection to also be complex (i.e. involving quasi-separatrix regions), however, as the eruption travels westward, it proceeds in more of a classic bipolar streamer-blowout CME fashion (e.g. Lynch et al., 2016).

Fig. 25(c) compares the reconnection flux in the MHD model (left panel) with the derived reconnection flux from the observations (right panel). The total reconnection flux in the MHD model was $\Phi_{rxn} = 7.4 \times 10^{21}$ Mx by the end of the simulation run, whereas the total reconnection flux estimate derived from the post-eruption arcade area in SDO/AIA 211Å observations was $\sim 2 \times 10^{21}$ Mx. In the

right panel of Fig. 25(c) we also show the MHD reconnection flux in a region of interest (ROI), denoted in 25(b) as the orange boundary of a 30° × 90° area in latitude by longitude. The total ROI reconnection flux matches the observational value almost exactly.

Fig. 26, top row, shows the view from Earth of representative magnetic field lines that illustrate the structure of the mid-latitude filament eruption. The bottom row of Fig. 26 plots synthetic white-light coronagraph emission derived via Thomson-scattering from a 3D electron density structure (Billings, 1966) based on the MHD simulation proton density ($n_e = n_p$) for each of the corresponding times in the top row. We have plotted the total brightness intensity ratio $I(t)/I(0)$ where $I(0)$ is the intensity of the simulation's initial, $t = 0$ hr spherically-symmetric density profile (as in Lynch et al., 2016; Lynch, 2020; Parenti et al., 2021). We note that despite the complex and distorted 3D magnetic flux rope structure of the CME ejecta, the derived synthetic white light signatures have all of the morphological features typically identified with flux rope CMEs in coronagraph observations (bright leading edge, dark circular cavity, bright central core; e.g. Illing and Hundhausen, 1985; Illing and Hundhausen, 1986; Vourlidas et al., 2013).

In addition to providing insight into how various photospheric and coronal magnetic configurations can lead to CME eruptions, and allowing for detailed investigations of the role that magnetic reconnection can play in these events, global MHD simulations of CME eruptions can provide important context and test-cases for heliospheric remote sensing methods. For example, two of the Tier 1 papers included in this special issue make use of global MHD simulations of CME eruptions to aid their remote sensing analyses. From the white light remote sensing perspective, Verbeke et al. (2022) analyzed the Lionello et al. (2013) simulation of a CME eruption into the heliosphere, run with the MAS (Magnetohydrodynamic Algorithm outside a Sphere; Riley et al., 2012) code, in order to quantify the uncertainties involved in reconstructing CME parameters from white light images using the GCS (Graduated Cylindrical Shell, Thernisien et al., 2006) method. From the interplanetary scintillation (IPS) perspective, Fallows et al. (2022) compared the density and velocity structures inferred from IPS observations of a CME event with those from an MHD simulation of the same CME performed with the SUSANOO-MHD code (Iwai et al., 2019).

7.2. Analysis of sympathetic eruptions resulting in a streamer blowout CME and its heliospheric evolution

In this section we summarize the analysis by Palmerio et al. (2021a) and Pal et al. (2022) of multi-spacecraft, remote-sensing and in situ observations of a streamer blowout CME that erupted on 2020 June 21 towards Earth and Parker Solar Probe. Parker Solar Probe was in its fifth orbit around the Sun, 20° west of the Sun–Earth line and at a distance of ∼ 0.52 AU when it measured the passage of this coherent, flux rope CME that lasted approximately 18 h, from 16:00UT June 25 until 10:00UT June 26. The STEREO-A spacecraft was located ∼ 70° east of the Sun–Earth line on June 21st, at a near optimal viewing geometry for off-limb EUV and white-light coronagraph observations of three sequential, and most likely sympathetic, eruptions. This sequence of eruptive events resulted in the total blowout of the overlying helmet streamer material.

CMEs result from the gradual accumulation of free magnetic energy and subsequent disruption of the

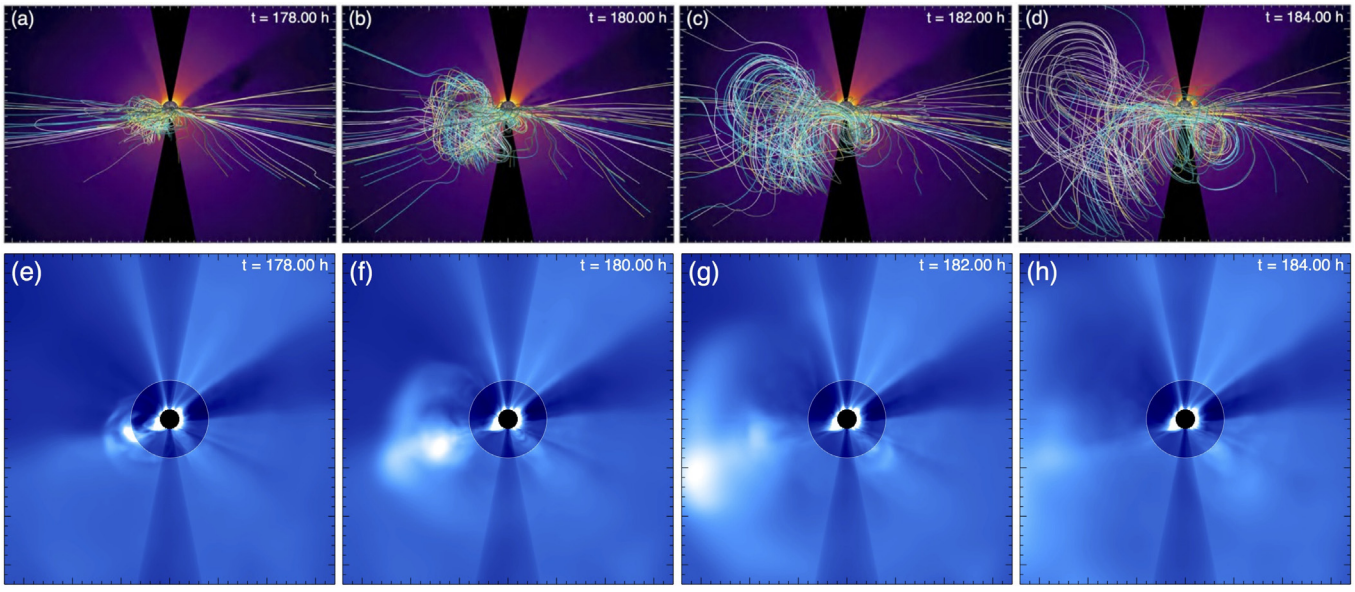

Fig. 26. Comparison between the CME's magnetic field structure and derived line-of-sight integrated white-light emission from Thomson scattering. Top row: Magnetic field lines depicting MHD simulation erupting flux rope structure. Bottom row: Synthetic white-light coronagraph images from the same viewpoint. Adapted from Lynch et al. (2021).

quasi-equilibrium of the pre-eruption energized magnetic structure (Forbes, 2000; Klimchuk, 2001). This accumulated free energy can power consecutive, sympathetic eruptions (e.g. Schrijver et al., 2013). In multipolar flux systems, CMEs may initiate via the magnetic breakout mechanism (Antiochos et al., 1999), where the breakout reconnection at an overlying, stressed null point gives rise to an increasing expansion of the energized arcade that eventually triggers explosive, eruptive flare reconnection below the rising sheared/twisted flux rope field. Under certain conditions, this topology has been shown to support consecutive eruptions from the same flux system (homologous CMEs; e.g., DeVore and Antiochos, 2008) and consecutive eruptions from adjacent flux systems (sympathetic CMEs; e.g., Török et al., 2011; Lynch and Edmondson, 2013; Dahlin et al., 2019).

Fig. 27(a) shows the on-disk and off-limb locations for the origin of three, consecutive eruptions (CMEs #0, #1, and #2) on 2020 June 21 in SDO/AIA and STEREO-A/EUVI and COR1 data. In addition, representative magnetic field lines from a PFSS extrapolation of the photospheric magnetic field are shown, colored by their connectivity and depicting the multipolar flux system of the sequential CMEs' source regions. The top row of Fig. 27(a) shows the SDO/AIA 211Å EUV image and the AIA 211Å image in base-difference to highlight the location of the on-disk signature associated with the first of the sequential eruptions, CME #0. This region (marked in pink) is located outside and to the northwest of the equatorial multipolar flux system, right on the boundary between the closed helmet streamer flux and the open flux of the polar coronal hole.

The bottom row of Fig. 27(a) shows the limb view of the multipolar flux system where the side-lobes are cyan, the small, central arcade is blue, the overlying streamer flux is orange, and open field lines are magenta. We also indicate the off-limb STEREO-A/EUVI emission features identified as the progenitors for the second (CME #1) and third (CME #2) eruptions of the sequence. The comparison of the large-scale PFSS topology and the locations of the high-altitude progenitors for CMEs #1 and #2 clearly indicate that the second and third eruptions in this sequence originate in the (energized) northern and southern side-lobes of the multipolar flux system, respectively.

Fig. 27(b) illustrates the sequence of each of the coronal eruptive transients. The left column of 27(b) shows STEREO-A/COR1 data which has been processed with a sliding, 45-min averaging window and has had a minimum intensity background removed. The low coronal trajectories for CMEs #1 and #2 are shown in cyan and yellow

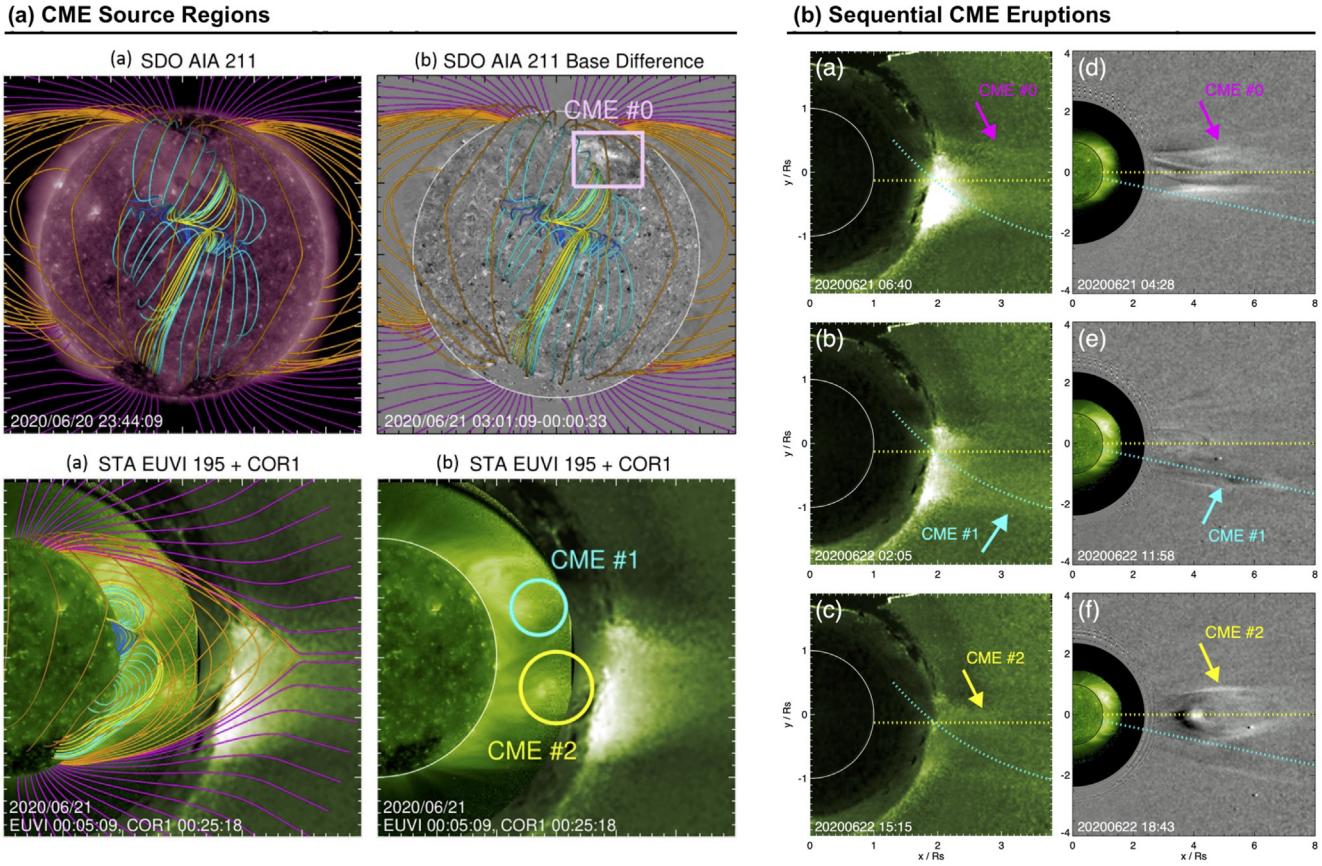

Fig. 27. Sequential, sympathetic CME eruptions resulting in a full streamer blowout on 2020 Jun 20–21 from a multipolar source region that was observed with Parker Solar Probe at ~0.5 AU. (a) Identification of the source region origins of the sequential CMEs. (b) Coronagraph signatures of the eruption sequence. Adapted from Pal et al. (2022).

dotted lines, respectively, while the transient white light intensity features associated with each eruption are annotated. The right column of 27(b) shows each corresponding CME in the STEREO-A/COR2 field of view using the standard running-difference processing (e.g. Sheeley et al., 1999). The COR2 signatures of each eruption are also annotated here, along with the COR2 trajectories for CMEs #1 and #2. The (plane-of-the-sky) velocities derived from the height-time profiles are 350 km/s, 173 km/s, and 246 km/s at $r = 20R_{\odot}$ for CMEs #0, #1, and #2, respectively.

The most noticeable aspect of the eruption sequence is the multi-stage/multi-eruption removal (i.e. blowout) of the overlying helmet streamer. The spatiotemporal proximity between the sequence of three eruptions observed over STEREO-A's west limb, combined with the large-scale geometry of the PFSS coronal field extrapolation, strongly suggest a direct and causal magnetic coupling between the eruptions (Schrijver et al., 2013). In the Török et al. (2011) MHD simulation, their coupled, sympathetic eruptions from the adjacent flux systems of a coronal pseudostreamer were triggered by a prior eruption that was *external* to the pseudostreamer arcades. In this scenario, CME #0 plays an analogous role, removing a portion of the overlying (restraining) helmet streamer flux and disrupting the quasi-equilibrium force-balance of the energized, multipolar flux system. CMEs #1 and #2 then erupt sympathetically, in succession. CME #1 starts in the northern side-lobe arcade and is seen to deflect south while CME #2 starts in the southern side-lobe and deflects northward (Palmerio et al., 2021a). As discussed in Lynch and Edmondson (2013), sympathetic CME eruptions can contain significant non-radial deflections, and these tend to be toward their overlying breakout current sheet. The breakout current sheet corresponds to a local magnetic pressure minimum, i.e., a natural path of least resistance for CME propagation (Shen et al., 2011; Gui et al., 2011; Kay and Opher, 2015). More generally, there are many examples of mid- to high-latitude eruptions deflecting towards the heliospheric current sheet (HCS) as they become streamer blowout CMEs (Cremades and Bothmer, 2004; Kilpua et al., 2009; Panasenco et al., 2013; Zheng et al., 2020; Getachew et al., 2022).

Despite their relatively modest speed, streamer blowout CMEs can still deflect and compress the ambient upstream solar wind plasma. This causes draping of the interplanetary magnetic field (IMF) around the CME, where the specific geometry of the draping depends on the size and shape of the CME, as well as its speed (Gosling and McComas, 1987). This CME–solar wind interface region can be the location of dynamic interaction, including magnetic reconnection (McComas et al., 1994; Dasso et al., 2006) between the CME and the upstream magnetic field, which can significantly erode the CME's magnetic flux and helicity (e.g. Dasso et al., 2006; Ruffenach et al., 2015; Pal et al., 2020). In fact, the statistical analysis by Ruffenach et al. (2015) found that the azimuthal flux imbalance expected from erosion by magnetic reconnection implied an average erosion of ~40% of the total poloidal/azimuthal flux by 1 AU. Additionally, roughly 30% of their flux rope CME boundaries showed in situ signatures of reconnection.

Fig. 28 depicts the in situ Parker Solar Probe observations of CME #2 and its surrounding heliospheric solar wind structures. From top-to-bottom, Fig. 28 plots the magnetic field magnitude, its RTN components (a spacecraft-centric coordinate system where R is a unit vector from the Sun to the spacecraft, $T = \Omega \times R/|\Omega \times R|$ where Ω is the solar rotation axis, and $N = R \times T$), the $\boldsymbol{B}$-field's azimuthal angle in the R–T plane, radial velocity, proton density, proton temperature, the pitch angle distribution (PAD) of 283–359 eV suprathermal electrons, and the plasma beta. The yellow-shaded region indicates the coherent flux rope CME and the light gray-shaded regions indicate encounters with the heliospheric current sheet and/or its surrounding plasma sheet. Pal et al. (2022) performed Minimum Variance Analysis (MVA; Sonnerup et al., 1967) on Regions 2 and 8 (indicated in the suprathermal electron panel) to find that the absolute latitude of the unit vector normals to these current sheet crossings were $\theta_n = 49°$ for Region 2 and $\theta_n = 61°$ for Region 8—consistent with the picture of the IMF and HCS being draped around the CME flux rope. The CME–solar wind interface is shown as the salmon-colored regions on either side of the magnetic ejecta. Region 5 shows some indication of reconnection signatures while Region 6' depicts the interval of unbalanced azimuthal flux, i.e. the portion of the CME that has eroded. Using the methodology outlined by Dasso et al. (2005), Dasso et al. (2006), Dasso et al. (2007), Pal et al. (2022) calculated that $18 \pm 11\%$ of the total azimuthal flux had reconnected by the time of the Parker Solar Probe encounter at 0.52 AU, and determined the erosion reconnection most likely started at a heliospheric distance of $r \approx 0.35$ AU. We note that many previous numerical simulations of magnetic breakout-initiated CMEs show indication of continued reconnection at the breakout current sheet during propagation through the extended corona and inner heliosphere (e.g. MacNeice et al., 2004; van der Holst et al., 2009; Karpen et al., 2012; Hosteaux et al., 2018).

7.3. Estimating CME flux rope structure, orientation, and flux content in the extended corona

Complementary remote-sensing and in situ observations of the same solar wind and transient structures, as well as in situ measurements over a range of angular separations and radial distances, are now possible with the launch of Parker Solar Probe and Solar Orbiter (e.g. Velli et al., 2020; Hadid et al., 2021; Möstl et al., 2022). In its first several encounters, Parker Solar Probe has observed a number of streamer blowout CME events that exhibit flux rope morphology in the remote-sensing observations (Howard et al., 2019; Hess et al., 2020; Wood et al., 2020; Liewer

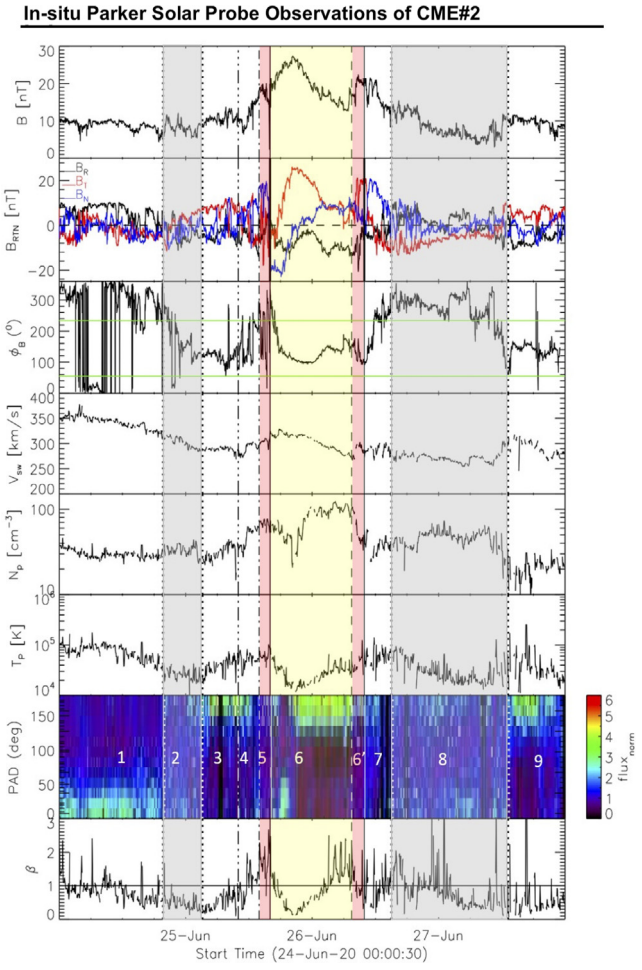

Fig. 28. In-situ Parker Solar Probe observations of the 2020 Jun 25–26 ICME identified with CME #2 in Fig. 27. The vertical yellow shading indicates the magnetic flux rope ejecta, the vertical pink shading shows the flux rope boundary interaction regions, and the the vertical gray shading denotes the surrounding draped IMF and HCS/HPS regions. See text for details. Adapted from Pal et al. (2022).

et al., 2021) and/or in the in situ measurements (Korreck et al., 2020; Lario et al., 2020; Nieves-Chinchilla et al., 2020; Palmerio et al., 2021a). There has also been a recent, concerted effort to emphasize the importance of multi-spacecraft observations throughout the inner heliosphere, ranging from in situ ICME case studies (Kilpua et al., 2019; Davies et al., 2021; Palmerio et al., 2021b; Palmerio et al., 2022a; Palmerio et al., 2022b), to statistical studies and event catalogs (Winslow et al., 2015; Good et al., 2019; Vršnak et al., 2019; Salman et al., 2020; Davies et al., 2022; Möstl et al., 2022; Scolini et al., 2022), and detailed comparisons between heliospheric simulation results and multiple synthetic observers (Scolini et al., 2019; Scolini et al., 2023).

Here we review the Lynch et al. (2022) analysis of MHD simulation data of a global, streamer-blowout CME (Lynch et al., 2019) with a focus on the 3D magnetic structure that would be seen by synthetic spacecraft observers with radial distances $r < 30R_\odot$ that had time-dependent, Parker-Solar-Probe-like trajectories. The spatial coordinates of the eight moving synthetic spacecraft are derived from the Parker Solar Probe ephemeris for orbits 7, 9, and 23. The encounter 7 perihelion was at a radial distance of $20.36R_\odot$ and occurred on January 17th, 2021 at 17:35 UT. The encounter 9 perihelion was at $15.98R_\odot$ on August 9th, 2021 at 19:10 UT. The encounter 23 perihelion is currently scheduled to reach a distance of $9.86R_\odot$ on March 22nd, 2025 at 21:55 UT.

Fig. 29 shows four representative encounters of synthetic spacecraft on Parker-Solar-Probe-like trajectories through different sections of the Lynch et al. (2019) global streamer blowout eruption. The top row of Fig. 29 presents the global context for each of the representative synthetic observer trajectories, as viewed from above the equatorial plane. Synthetic observers P3, P4, and P5 are on trajectories derived from Parker Solar Probe's encounter 9 orbit, whereas observer P8 is based on future encounter 23's orbit ephemeris. The middle row of Fig. 29 plots 3D visualizations of the spacecraft positions (the yellow sphere that is instantaneously sampling the yellow field line), a set of adjacent field lines (dark gray) traced at $0.25R_\odot$ intervals in radius on each side of the spacecraft, and a set of light gray field lines indicating the approximate MHD flux rope boundary. The planar cut with the red-to-blue colorscale shows the twist component of the flux rope field whereas the planar cut with the rainbow colorscale (mostly purple-blue) shows the log of mass density through the flux rope cross-section.

We have applied several common in situ flux rope models and their fitting techniques (Al-Haddad et al., 2013; Al-Haddad et al., 2018) to this set of synthetic simulation time series to determine whether the in situ flux rope models commonly used at 1 AU can be used to *successfully* estimate and reconstruct the 3D flux rope structure, orientation, and flux content of CMEs in the outer corona. The three in situ flux rope models we investigate are: the Lundquist (1950) constant-α, linear force-free cylinder model (LFF; Burlaga, 1988; Lepping et al., 1990), the Gold and Hoyle (1960) uniform-twist model (GH; Farrugia et al., 1999), and a non-force free circular cross-section model (CCS; Hidalgo et al., 2000; Nieves-Chinchilla et al., 2016). We note these simple flux rope models are highly idealized, cylindrically-symmetric configurations. More sophisticated flux rope models exist (e.g. Mulligan et al., 2013; Hu et al., 2014; Nieves-Chinchilla et al., 2018; Weiss et al., 2022) however there is a natural trade off between model complexity and the number of free parameters, and even the simple models tend to be under-constrained during most single-spacecraft ICME encounters.

The bottom row of Fig. 29 shows the synthetic time series of the magnetic field components of $\boldsymbol{B}_{\mathrm{RTN}}$. From left-to-right, each column corresponds to a different encounter type: Type 1—classic bipolar orientation (low inclination); Type 2—classic unipolar orientation (high inclination); Type 3—the problematic large azithumal angle ϕ_0 orienta-

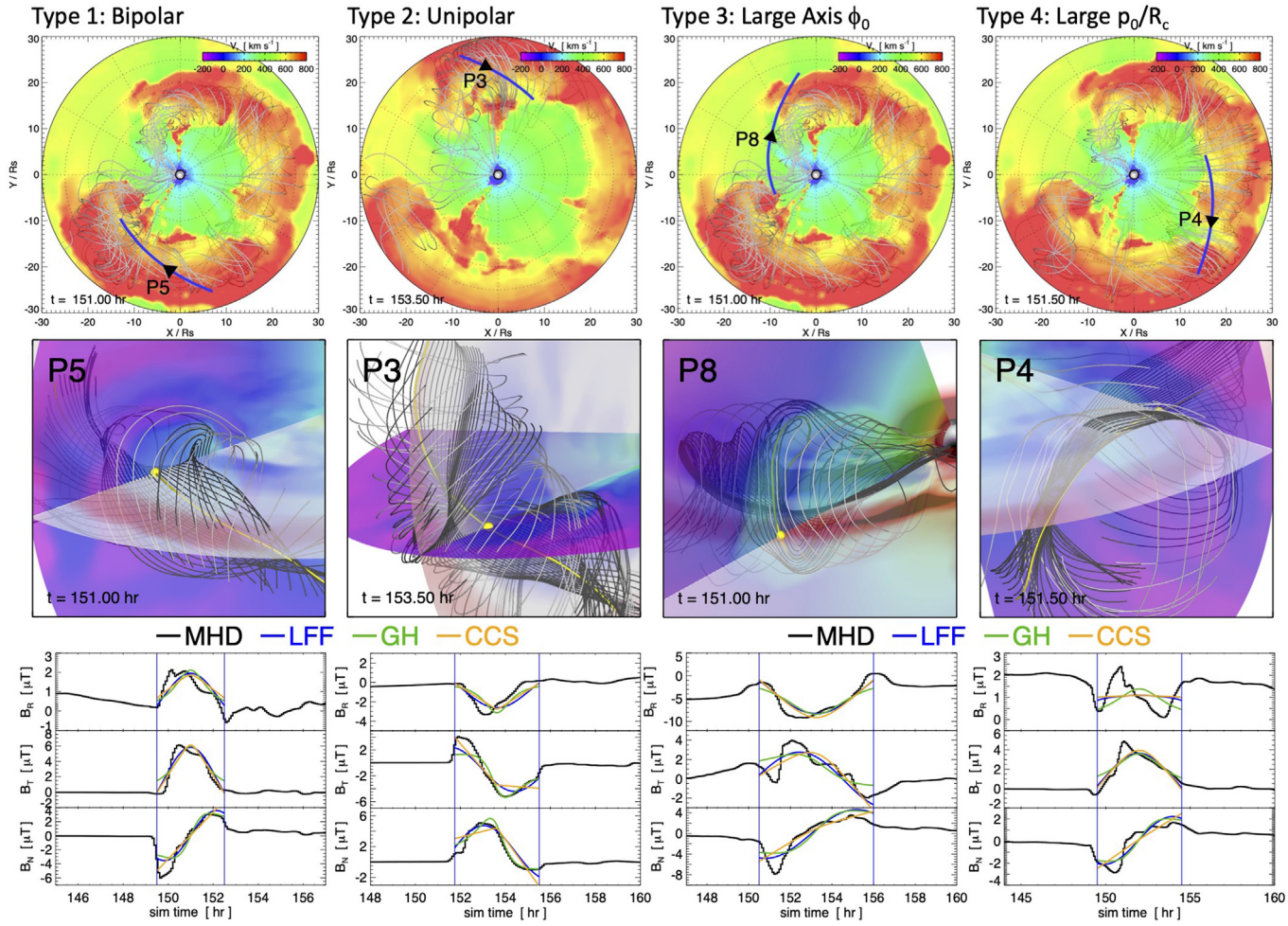

Fig. 29. Four examples of synthetic spacecraft observers on Parker-Solar-Probe-like trajectories flying through the Lynch et al. (2019) MHD simulation data of a global-scale streamer blowout CME. Top row: Global context for the synthetic observer positions within the 3D data cube. The P3, P4, and P5 trajectories are derived from Parker Solar Probe's encounter 9 orbit while the P8 trajectory is derived from future encounter 23. Middle row: Instantaneous position of the observer (yellow sphere) with representative magnetic field lines. Bottom row: $\boldsymbol{B}_{\mathrm{RTN}}(t)$ time series with three different flux rope model fits (LFF, GH, and CCS) to the coherent MHD field rotations. Adapted from Lynch et al. (2022).

tion (i.e spacecraft trajectory includes a significant component along the flux rope axis); and Type 4—the problematic large impact parameter trajectory (i.e. spacecraft passes far from the axis of symmetry). For each of the synthetic time series, the CME boundaries are marked with vertical blue lines and the MHD flux ropes are fit with the LFF, GH, and CCS in situ flux rope models shown as blue, green, and orange lines, respectively.

In addition to the magnetic field component fits shown above, Lynch et al. (2022) compared a number of geometric parameters for the cylindrical flux rope models with their corresponding MHD values—specifically, the axis orientation, impact parameter, and flux rope radius R_c. These parameters are used, along with the analytic description of the in situ flux rope model magnetic field structure, to calculate the toroidal/axial flux (Φ_t) and the poloidal/twist flux per unit length (Φ_p/L) for each model fit. The equivalent flux components are calculated directly from the MHD data cube at the times and locations of the set of 16 total synthetic observers. We found that the peak of the in situ flux rope model distribution of $(\Phi_t, \Phi_p/L)$ lies below the peak of the MHD distribution in both toroidal and poloidal flux (per unit length) coordinates. This suggests that the in situ flux rope (FR) models are underestimating both components of the CME flux content: the toroidal/axial flux by ~60%, i.e., $\langle \Phi_t^{\mathrm{MHD}} \rangle \approx 1.63 \langle \Phi_t^{\mathrm{FR}} \rangle$, and the poloidal/twist flux by ~25%, i.e., $\left\langle (\Phi_p/L)^{\mathrm{MHD}} \right\rangle \approx 1.26 \left\langle (\Phi_p/L)^{\mathrm{FR}} \right\rangle$.

We also examined the internal structure of the $\boldsymbol{j} \times \boldsymbol{B}$ misalignment angle ϑ, defined as $\vartheta = \sin^{-1} |\boldsymbol{j} \times \boldsymbol{B}| / (|\boldsymbol{j}||\boldsymbol{B}|)$. We determined that the MHD ejecta intervals, while not force-free, appear to be *more* force-free than the best-fit CCS flux rope solutions (at least statistically) and *less* force free than the Kumar and Rust (1996) assumption that the magnetic field structure is only a small departure from the LFF cylinder model. Given the typical values obtained for the percentage of the MHD flux rope intervals that fall

below the "approximately force free" threshold of $\vartheta \approx 17^{\circ}$ (Möstl et al., 2009; Nieves-Chinchilla et al., 2016), we characterized the MHD ejecta as having dissipated somewhere between 30–60% of the excess magnetic energy responsible for the non-zero Lorentz force. In principle, this reinforces the Lynch et al. (2004) suggestion that a significant amount of the excess magnetic energy *within* the CME flux rope can be dissipated by $\sim 15 R_{\odot}$.

Overall, we found that, despite the idealized nature of the simplest, cylindrically symmetric in situ flux rope models, many of the trajectories through the 3D magnetic structure of the Lynch et al. (2019) CME simulation were reasonably well approximated by each of the in situ flux rope models. Unsurprisingly, the Type 1 and Type 2 events—corresponding to the classic bipolar and unipolar flux rope configurations with a very small impact parameter—yield the most robust fitting results. The problematic encounters—those with a significant radial component of the flux rope axis or a large impact parameter—were less successful as a whole but still had the occasional individual fit that matched the MHD orientation properties.

The cylindrical flux rope models tended to underestimate the MHD CME's toroidal/axial flux much more than the poloidal/twist flux. These results will have some impact on the *quantitative* comparisons between observed reconnection flux in the solar atmosphere and the poloidal/twist flux inferred via flux rope model fits to in situ magnetic field and plasma observations (e.g. Qiu et al., 2007; Hu et al., 2014; Gopalswamy et al., 2017). However, we also note that the cylinder model uncertainties are large (on the order of 30%), so the discrepancy between the MHD poloidal/twist flux average and the in situ model average is comfortably within 1σ of the $\left(\Phi_p/L\right)^{\mathrm{FR}}$ distribution. There is certainly more work that needs to be done to fully understand and appreciate the limitations of in situ flux rope modeling, but we do find it encouraging that, as an analysis tool, the in situ flux rope models appear to be no worse at describing CME's internal structure at $r \lesssim 30 R_{\odot}$ than at $\sim$1 AU.

8. Discussion of outstanding questions and recommendations for research on CME onset

Why Is Understanding Eruption Onset Important? Space weather forecasting would be significantly improved if the understanding of eruption onset mechanisms were advanced enough to use this understanding to accurately predict eruptions prior to their occurrence. Such an advanced understanding of the mechanism or mechanisms that cause eruption onset would provide more lead time in forecasting eruption effects at Earth, without the need to wait for coronal observations. Ideally, a broad understanding of eruption onset causes would provide guidance, even without running simulations, on whether a particular solar magnetic configuration were favorable to eruptions. For example, this could provide the means for making all clear forecasts. Furthermore, while the effects of CME magnetic fields, densities, and velocities can to some extent now be predicted with a day or more advance notice once the CME is observed to erupt, the same cannot be said for the effects of high energy (ionizing) flare radiation and Solar Energetic Particle (SEP) events, which arrive at Earth much more quickly following an eruption. Using knowledge of eruption onset mechanisms to enable early predictions that an eruption is likely is critically important for SEP forecasts.

What Key Information are We Still Missing? The modeling efforts summarized here rely on a broad range of energization mechanisms to build towards an eruption onset, including the generation of an energized magnetic flux rope in the corona, shear flows driven at the photosphere, and magnetic flux emerging through the photosphere. Each of these, as demonstrated here, can lead to an eruption - but many are difficult to predict. How much energy has been stored in a filament channel or flux rope that is observed in the corona? How much more flux emergence or shear flow would be needed to energize this structure such that it erupts? Would either mechanism suffice to drive eruption onset for a particular coronal structure, or are both flux emergence and shear flows needed for some scenarios? How important is flux cancellation, which was not represented in the mechanisms explored here? How much of the stored magnetic energy will be released in an eruption, and how will that released energy be distributed between kinetic, particle, and thermal energy? The work here provides promising suggestions as to the answers to these questions, but further work needs to be done to clearly determine the current state of the magnetic field in an active region or prominence, and further work needs to be done to constrain the driving conditions which could cause different classes of coronal magnetic structures to erupt.

How Do We Make Progress? The broad scope of the flare/CME onset problem requires teamwork. In particular, a combination of theory, modeling, and observational expertise is needed to solve this problem. New observatories are now providing promising information which can help solve the problem of determining the pre-eruptive structure of coronal magnetic fields as well as the structure of CMEs shortly after eruption. In particular, DKIST (Rast et al., 2021) promises new capabilities for measuring coronal fields off the limb of the sun, which would providing new information about the state of the coronal magnetic field in prominences and active regions. Solar Orbiter (Müller et al., 2020) promises, for example, new capabilities for measuring the magnetic field of the photosphere on the side of the sun not visible from Earth, and therefore providing improved inputs, for example, for potential field source surface models and for tracking energy and helicity injection into active regions. Parker Solar Probe (Fox et al., 2016) is now periodically flying through the outer corona during perihelia, and therefore providing both in situ and remote sensing insight into the structure of CMEs early in their ejection from the Sun.

In this LWS team, each group was focused on one or more aspects of the problem, but even so, not all aspects could be represented. The work of each group, however, benefited enormously from the interactions and collaborations with the rest of the LWS team. We, therefore, recommend continuing such team investigations of this problem, but allowing for a broader, and in particular an international, scientific participation. For example, setting up an international scientific center of excellence on flare/CME onset and eruption would provide a promising means to bring together the necessary expertise from the international community and foster strong collaboration on the difficult questions that remain.

Declaration of Competing Interest

The authors declare that they have no known competing financial interests or personal relationships that could have appeared to influence the work reported in this paper.

Acknowledgments

The work reported on here was primarily supported by the NASA Living with a Star Focused Science Team on "Understanding the Onset of Major Solar Eruptions." M.G.L. and team members acknowledge support by NASA LWS grant 80HQTR19T0084. M.G.L. acknowledges support from the Office of Naval Research. T.T. acknowledges additional support by NASA grants 80NSSC19K0263 and 80NSSC20K1274, and by NSF grant ICER-1854790. S.K.A. and team members acknowledge support by a NASA LWS grant to NASA Goddard Space Flight Center. G.B. acknowledges support by NASA LWS grant 80NSSC19K0087 to NorthWest Research Associates. Y.F. acknowledges support by the NASA LWS grant 80NSSC19K0070 and by the National Center for Atmospheric Research (NCAR), which is a major facility sponsored by the National Science Foundation under Cooperative Agreement No. 1852977. B.J.L. acknowledges support from NASA LWS 80NSSC19K0088 and NSF AGS-1851945. Y.L., B.T.W., and team members acknowledge support from NASA LWS 80NSSC19K0072.

Resources supporting this work were provided by the NASA High-End Computing (HEC) Program through the NASA Advanced Supercomputing (NAS) Division at Ames Research Center and the NASA Center for Climate Simulation (NCCS) at Goddard Space Flight Center. Y.F. also acknowledges high-performance computing support from Cheyenne (doi:10.5065/D6RX99HX) provided by NCAR's Computational and Information Systems Laboratory, sponsored by the National Science Foundation.

References

Afanasyev, A.N., Kazachenko, M.D., Fan, Y., et al., 2021. Validation of the PDFI_SS method for electric field inversions using a magnetic flux emergence simulation. ApJ 919 (1), 7. https://doi.org/10.3847/1538-4357/ac0d01, arXiv:2106.10579.

Al-Haddad, N., Nieves-Chinchilla, T., Savani, N.P., et al., 2018. Fitting and reconstruction of thirteen simple coronal mass ejections. SoPh 293 (5), 73. https://doi.org/10.1007/s11207-018-1288-3, arXiv:1804.02359.

Al-Haddad, N., Nieves-Chinchilla, T., Savani, N.P., et al., 2013. Magnetic field configuration models and reconstruction methods for interplanetary coronal mass ejections. SoPh 284, 129–149. https://doi.org/10.1007/s11207-013-0244-5, arXiv:1209.6394.

Aly, J.J., 1984. On some properties of force-free magnetic fields in infinite regions of space. ApJ 283, 349–362. https://doi.org/10.1086/162313.

Amari, T., Aly, J., Mikic, Z., et al., 2010. Coronal mass ejection initiation: on the nature of the flux cancellation model. ApJL 717, L26–L30. https://doi.org/10.1088/2041-8205/717/1/L26, arXiv:1005.4669.

Amari, T., Aly, J.J., Canou, A., et al., 2013. Reconstruction of the solar coronal magnetic field in spherical geometry. A&A 553, A43. https://doi.org/10.1051/0004-6361/201220787.

Antiochos, S.K., 2013. Helicity condensation as the origin of coronal and solar wind structure. ApJ 772, 72. https://doi.org/10.1088/0004-637X/772/1/72.

Antiochos, S.K., DeVore, C.R., Klimchuk, J.A., 1999. A model for solar coronal mass ejections. ApJ 510, 485–493. https://doi.org/10.1086/306563.

Arber, T.D., Longbottom, A.W., Gerrard, C.L., et al., 2001. A staggered grid, lagrangian-eulerian remap code for 3-D MHD simulations. J. Comput. Phys. 171, 151–181. https://doi.org/10.1006/jcph.2001.6780.

Archontis, V., Hood, A.W., 2012. Magnetic flux emergence: a precursor of solar plasma expulsion. A&A 537, A62. https://doi.org/10.1051/0004-6361/201116956.

Archontis, V., Török, T., 2008. Eruption of magnetic flux ropes during flux emergence. A&A 492, L35–L38. https://doi.org/10.1051/0004-6361:200811131, arXiv:0811.1134.

Arge, C.N., Henney, C.J., Hernandez, I.G. et al., 2013. Modeling the corona and solar wind using ADAPT maps that include far-side observations. In: Zank, G.P., Borovsky, J., Bruno, R., Cirtain, J., Cranmer, S., Elliott, H., Giacalone, J., Gonzalez, W., Li, G., Marsch, E., Moebius, E., Pogorelov, N., Spann, J., Verkhoglyadova, O. (Eds.), American Institute of Physics Conference Series, volume 1539 of American Institute of Physics Conference Series, pp. 11–14, https://doi.org/10.1063/1.4810977.

Arge, C.N., Henney, C.J., Koller, J. et al., 2010. Air force data assimilative photospheric flux transport (ADAPT) model. in: Twelfth International Solar Wind Conference, vol. 1216, pp. 343–346. https://doi.org/10.1063/1.3395870.

Arge, C.N., Luhmann, J.G., Odstrcil, D., et al., 2004. Stream structure and coronal sources of the solar wind during the may 12th, 1997 CME. J. Atmos. Solar Terr. Phys. 66, 1295–1309. https://doi.org/10.1016/j.jastp.2004.03.018.

Arge, C.N., Odstrcil, D., Pizzo, V.J. et al., 2003. Improved method for specifying solar wind speed near the sun. In: Velli, M., Bruno, R., Malara, F., Bucci, B. (Eds.), Solar Wind Ten, volume 679 of American Institute of Physics Conference Series, pp. 190–193, https://doi.org/10.1063/1.1618574.

Arge, C.N., Pizzo, V.J., 2000. Improvement in the prediction of solar wind conditions using near-real time solar magnetic field updates. JGR 105, 10465–10480. https://doi.org/10.1029/1999JA000262.

Aulanier, G., Török, T., Démoulin, P., et al., 2010. Formation of torus-unstable flux ropes and electric currents in erupting sigmoids. ApJ 708 (1), 314–333. https://doi.org/10.1088/0004-637X/708/1/314.

Barnes, G., DeRosa, M.L., Jones, S.I., et al., 2023. Implications of different solar photospheric flux-transport models for global coronal and heliospheric modeling. ApJ 946, 105. https://doi.org/10.3847/1538-4357/acba8e.

Berger, M.A., 1984. Rigorous new limits on magnetic helicity dissipation in the solar corona. Geophys. Astrophys. Fluid Dyn. 30 (1), 79–104. https://doi.org/10.1080/03091928408210078.

Berger, M.A., 1997. Magnetic helicity in a periodic domain. JGR 102 (A2), 2637–2644. https://doi.org/10.1029/96JA01896.

Berger, M.A., Ruzmaikin, A., 2000. Rate of helicity production by solar rotation. JGR 105 (A5), 10481–10490. https://doi.org/10.1029/1999JA900392.

Berger, M.J., Oliger, J., 1984. Adaptive mesh refinement for hyperbolic partial differential equations. J. Comput. Phys. 53, 484–512. https://doi.org/10.1016/0021-9991(84)90073-1.

Berger, T.E., Loefdahl, M.G., Shine, R.S., et al., 1998. Measurements of solar magnetic element motion from high-resolution filtergrams. ApJ 495, 973–983. https://doi.org/10.1086/305309.

Billings, D.E., 1966. A guide to the solar corona. Academic Press, New York.

Biskamp, D., 1993. Current sheet profiles in two-dimensional magneto-hydrodynamics. Phys. Fluids B 5, 3893–3896. https://doi.org/10.1063/1.860612.

Bobra, M.G., Sun, X., Hoeksema, J.T., et al., 2014. The Helioseismic and Magnetic Imager (HMI) vector magnetic field pipeline: SHARPs - space-weather HMI active region patches. SoPh 289 (9), 3549–3578. https://doi.org/10.1007/s11207-014-0529-3, arXiv:1404.1879.

Bothmer, V., Schwenn, R., 1998. The structure and origin of magnetic clouds in the solar wind. AnGeo 16, 1–24. https://doi.org/10.1007/s00585-997-0001-x.

Bourdin, P.A., Bingert, S., Peter, H., 2013. Observationally driven 3D magnetohydrodynamics model of the solar corona above an active region. A&A 555, A123. https://doi.org/10.1051/0004-6361/201321185, arXiv:1305.5693.

Burlaga, L.F., 1988. Magnetic clouds and force-free fields with constant alpha. JGR 93, 7217–7224. https://doi.org/10.1029/JA093iA07p07217.

Canfield, R.C., Priest, E.R., Rust, D.M., 1974. A model for the solar flare. In: Nakagawa, Y., Rust, D.M. (Eds.), Flare-related Magnetic Field Dynamics. Boulder CO, NCAR, p. 361.

Chen, F., Cheung, M.C.M., Rempel, M. et al., 2023. Data-Driven Radiative Magnetohydrodynamics Simulations with the MURaM code. arXiv e-prints, p. arXiv:2301.07621, https://doi.org/10.48550/arXiv.2301.07621. arXiv:2301.07621.

Chen, P.F., 2011. Coronal mass ejections: models and their observational basis. Living Rev. Sol. Phys. 8 (1), 1. https://doi.org/10.12942/lrsp-2011-1.

Chen, P.F., Shibata, K., 2000. An emerging flux trigger mechanism for coronal mass ejections. ApJ 545, 524–531. https://doi.org/10.1086/317803.

Cheung, M.C.M., DeRosa, M.L., 2012. A method for data-driven simulations of evolving solar active regions. ApJ 757 (2), 147. https://doi.org/10.1088/0004-637X/757/2/147, arXiv:1208.2954.

Cheung, M.C.M., Isobe, H., 2014. Flux Emergence (Theory). Living Rev. Sol. Phys. 11, 3. https://doi.org/10.12942/lrsp-2014-3.

Chintzoglou, G., Patsourakos, S., Vourlidas, A., 2015. Formation of magnetic flux ropes during a confined flaring well before the onset of a pair of major coronal mass ejections. ApJ 809, 34. https://doi.org/10.1088/0004-637X/809/1/34, arXiv:1507.01165.

Cremades, H., Bothmer, V., 2004. On the three-dimensional configuration of coronal mass ejections. A&A 422, 307–322. https://doi.org/10.1051/0004-6361:20035776.

Dacie, S., Török, T., Démoulin, P., et al., 2018. Sequential eruptions triggered by flux emergence: observations and modeling. ApJ 862 (2), 117. https://doi.org/10.3847/1538-4357/aacce3, arXiv:1807.00020.

Dahlin, J.T., Antiochos, S.K., DeVore, C.R., 2019. A model for energy buildup and eruption onset in coronal mass ejections. ApJ 879, 96. https://doi.org/10.3847/1538-4357/ab262a.

Dahlin, J.T., Antiochos, S.K., Qiu, J., et al., 2022a. Variability of the reconnection guide field in solar flares. ApJ 932, 94. https://doi.org/10.3847/1538-4357/ac6e3d.

Dahlin, J.T., DeVore, C.R., Antiochos, S.K., 2022b. STITCH: a subgrid-scale model for energy buildup in the solar corona. ApJ 941 (1), 79. https://doi.org/10.3847/1538-4357/ac9e5a.

Dasso, S., Gulisano, A.M., Mandrini, C.H., et al., 2005. Model-independent large-scale magnetohydrodynamic quantities in magnetic clouds. Adv. Space Res. 35 (12), 2172–2177. https://doi.org/10.1016/j.asr.2005.03.054.

Dasso, S., Mandrini, C.H., Démoulin, P., et al., 2006. A new model-independent method to compute magnetic helicity in magnetic clouds. A&A 455 (1), 349–359. https://doi.org/10.1051/0004-6361:20064806.

Dasso, S., Nakwacki, M.S., Démoulin, P., et al., 2007. Progressive transformation of a flux rope to an ICME. Comparative analysis using the direct and fitted expansion methods. SoPh 244 (1–2), 115–137. https://doi.org/10.1007/s11207-007-9034-2, arXiv:0706.2889.

Davies, E.E., Möstl, C., Owens, M.J., et al., 2021. In situ multi-spacecraft and remote imaging observations of the first CME detected by Solar Orbiter and BepiColombo. A&A 656, A2. https://doi.org/10.1051/0004-6361/202040113, arXiv:2012.07456.

Davies, E.E., Winslow, R.M., Scolini, C., et al., 2022. Multi-spacecraft observations of the evolution of interplanetary coronal mass ejections between 0.3 and 2.2 au: conjunctions with the juno spacecraft. ApJ 933 (2), 127. https://doi.org/10.3847/1538-4357/ac731a, arXiv:2205.09472.

Démoulin, P., Janvier, M., Dasso, S., 2016. Magnetic flux and helicity of magnetic clouds. SoPh 291 (2), 531–557. https://doi.org/10.1007/s11207-015-0836-3, arXiv:1509.01068.

Démoulin, P., Pariat, E., 2009. Modelling and observations of photospheric magnetic helicity. Adv. Space Res. 43, 1013–1031. https://doi.org/10.1016/j.asr.2008.12.004.

Deng, N., Xu, Y., Yang, G., et al., 2006. Multiwavelength study of flow fields in flaring super active region NOAA 10486. ApJ 644, 1278–1291. https://doi.org/10.1086/503600.

DeVore, C.R., Antiochos, S.K., 2008. Homologous confined filament eruptions via magnetic breakout. ApJ 680, 740–756. https://doi.org/10.1086/588011.

Ding, J.Y., Hu, Y.Q., 2008. Coronal flux rope catastrophe caused by photospheric flux emergence. ApJ 674, 554–559. https://doi.org/10.1086/524937.

Dubey, G., van der Holst, B., Poedts, S., 2006. Initiation of CMEs by magnetic flux emergence. J. Astrophys. Astron. 27, 159–166. https://doi.org/10.1007/BF02702518.

Fallows, R.A., Iwai, K., Jackson, B.V., et al., 2022. Application of novel interplanetary scintillation visualisations using lofar: A case study of merged cmes from september 2017. Adv. Space Res. https://doi.org/10.1016/j.asr.2022.08.076 (in press).

Fan, Y., 2001. The Emergence of a Twisted Ω-Tube into the Solar Atmosphere. ApJL 554, L111–L114. https://doi.org/10.1086/320935.

Fan, Y., 2017. MHD simulations of the eruption of coronal flux ropes under coronal streamers. ApJ 844 (1), 26. https://doi.org/10.3847/1538-4357/aa7a56, arXiv:1706.06076.

Farrugia, C.J., Janoo, L.A., Torbert, R.B. et al., 1999. A uniform-twist magnetic flux rope in the solar wind. In: Habbal, S.R., Esser, R., Hollweg, J.V., Isenberg, P.A., (Eds.), Solar Wind Nine, volume 471 of American Institute of Physics Conference Series, pp. 745–748, https://doi.org/10.1063/1.58724.

Feigelson, E.D., Babu, G.J., 2012. Modern Statistical Methods for Astronomy with R Applications. The Edinburgh Building, Cambridge, CB2 8RU, UK: Cambridge University Press.

Feynman, J., Martin, S.F., 1995. The initiation of coronal mass ejections by newly emerging magnetic flux. JGR 100, 3355–3367. https://doi.org/10.1029/94JA02591.

Finn, J., Antonsen, 1985. Magnetic helicity: what is it, and what is it good for? Commments Plasma Phys. Controll. Fus. 9, 111.

Fisher, G.H., Kazachenko, M.D., Welsch, B.T., et al., 2020. The PDFI_SS electric field inversion software. ApJS 248 (1), 2. https://doi.org/10.3847/1538-4365/ab8303, arXiv:1912.08301.

Forbes, T.G., 2000. A review on the genesis of coronal mass ejections. JGR 105, 23153–23166. https://doi.org/10.1029/2000JA000005.

Forbes, T.G., Priest, E.R., 1983. A numerical experiment relevant to line-tied reconnection in two-ribbon flares. SoPh 84, 169–188. https://doi.org/10.1007/BF00157455.

Fox, N.J., Velli, M.C., Bale, S.D., et al., 2016. The solar probe plus mission: humanity's first visit to our star. SSRv 204 (1–4), 7–48. https://doi.org/10.1007/s11214-015-0211-6.

Freed, M.S., Longcope, D.W., McKenzie, D.E., 2015. Three-year global survey of coronal null points from potential-field-source-surface (pfss) modeling and solar dynamics observatory (sdo) observations. SoPh 290, 467–490. https://doi.org/10.1007/s11207-014-0616-5.

Galsgaard, K., Archontis, V., Moreno-Insertis, F., et al., 2007. The effect of the relative orientation between the coronal field and new emerging flux. I. Global properties. ApJ 666 (1), 516–531. https://doi.org/10.1086/519756, arXiv:0705.1097.

Galsgaard, K., Moreno-Insertis, F., Archontis, V., et al., 2005. A Three-dimensional study of reconnection, current sheets, and jets resulting from magnetic flux emergence in the sun. ApJL 618 (2), L153–L156. https://doi.org/10.1086/427872, arXiv:astro-ph/0410057.

Gauß, C.F., 1839. Allgemeine theorie des erdmagnetismus. In: Gauss, C. F., Weber, W. (Eds.), Resultate aus den Beobachtungen des magnetischen Vereins im Jahre 1838. Weidmannsche Buchhandlung, Leipzig, pp. 1–57.

Georgoulis, M.K., Yardley, S., Guerrae, J.A. et al., 2023. Prediction of Solar Eruptive Events Impacting Space Weather Conditions. Advances in Space Research, submitted.

Getachew, T., McComas, D.J., Joyce, C.J., et al., 2022. PSP/IS⊙IS observation of a solar energetic particle event associated with a streamer blowout coronal mass ejection during encounter 6. ApJ 925 (2), 212. https://doi.org/10.3847/1538-4357/ac408f, arXiv:2112.04671.

Gold, T., Hoyle, F., 1960. On the origin of solar flares. MNRAS 120, 89. https://doi.org/10.1093/mnras/120.2.89.

Gombosi, T.I., van der Holst, B., Manchester, W.B., et al., 2018. Extended MHD modeling of the steady solar corona and the solar wind. Living Rev. Sol. Phys. 15 (1), 4. https://doi.org/10.1007/s41116-018-0014-4, arXiv:1807.00417.

Good, S.W., Kilpua, E.K.J., LaMoury, A.T., et al., 2019. Self-Similarity of ICME flux ropes: observations by radially aligned spacecraft in the inner heliosphere. JGR 124 (7), 4960–4982. https://doi.org/10.1029/2019JA026475, arXiv:1905.07227.

Gopalswamy, N., Akiyama, S., Yashiro, S. et al., 2018. A New Technique to Provide Realistic Input to CME Forecasting Models. In: Foullon, C., Malandraki O.E. (Eds.), Space Weather of the Heliosphere: Processes and Forecasts, volume 335 of IAU Symposium, pp. 258–262, https://doi.org/10.1017/S1743921317011048. arXiv:1709.03160.

Gopalswamy, N., Yashiro, S., Akiyama, S., et al., 2017. Estimation of reconnection flux using post-eruption arcades and its relevance to magnetic clouds at 1 AU. SoPh 292, 65. https://doi.org/10.1007/s11207-017-1080-9, arXiv:1701.01943.

Gosling, J.T., McComas, D.J., 1987. Field line draping about fast coronal mass ejecta: A source of strong out-of-the-ecliptic interplanetary magnetic fields. GRL 14 (4), 355–358. https://doi.org/10.1029/GL014i004p00355.

Green, L.M., López fuentes, M.C., Mandrini, C.H., et al., 2002. The magnetic helicity budget of a cme-prolific active region. SoPh 208, 43–68. https://doi.org/10.1023/A:1019658520033.

Green, L.M., Thalmann, J.K., Valori, G., et al., 2022. Magnetic helicity evolution and eruptive activity in NOAA active region 11158. ApJ 937 (2), 59. https://doi.org/10.3847/1538-4357/ac88cb.

Green, L.M., Török, T., Vršnak, B., et al., 2018. The origin, early evolution and predictability of solar eruptions. SSRv 214 (1), 46. https://doi.org/10.1007/s11214-017-0462-5, arXiv:1801.04608.

Gudiksen, B.V., Nordlund, Å., 2005. An ab initio approach to the solar coronal heating problem. ApJ 618 (2), 1020–1030. https://doi.org/10.1086/426063, arXiv:astro-ph/0407266.

Gui, B., Shen, C., Wang, Y., et al., 2011. Quantitative analysis of CME deflections in the corona. SoPh 271 (1–2), 111–139. https://doi.org/10.1007/s11207-011-9791-9, arXiv:1105.3382.

Hadid, L.Z., Génot, V., Aizawa, S., et al., 2021. BepiColombo's cruise phase: unique opportunity for synergistic observations. FrASS 8, 154. https://doi.org/10.3389/fspas.2021.718024.

Hagyard, M.J., Teuber, D., West, E.A., et al., 1984. A quantitative study relating observed shear in photospheric magnetic fields to repeated flaring. SoPh 91, 115–126. https://doi.org/10.1007/BF00213618.

Haynes, A.L., Parnell, C.E., 2007. A trilinear method for finding null points in a three-dimensional vector space. Phys. Plasmas 14 (8). https://doi.org/10.1063/1.2756751 082107.

Hess, P., Rouillard, A.P., Kouloumvakos, A., et al., 2020. WISPR imaging of a pristine CME. ApJS 246 (2), 25. https://doi.org/10.3847/1538-4365/ab4ff0, arXiv:1912.02255.

Heyvaerts, J., Priest, E.R., 1984. Coronal heating by reconnection in DC current systems - A theory based on Taylor's hypothesis. A&A 137 (1), 63–78.

Heyvaerts, J., Priest, E.R., Rust, D.M., 1977. An emerging flux model for the solar phenomenon. ApJ 216, 123–137. https://doi.org/10.1086/155453.

Hickmann, K.S., Godinez, H.C., Henney, C.J., et al., 2015. Data assimilation in the ADAPT photospheric flux transport model. SoPh 290 (4), 1105–1118. https://doi.org/10.1007/s11207-015-0666-3, arXiv:1410.6185.

Hidalgo, M.A., Cid, C., Medina, J., et al., 2000. A new model for the topology of magnetic clouds in the solar wind. SoPh 194 (1), 165–174. https://doi.org/10.1023/A:1005206107017.

Hoeksema, J.T., Liu, Y., Hayashi, K., et al., 2014. The Helioseismic and Magnetic Imager (HMI) vector magnetic field pipeline: overview and performance. SoPh 289, 3483–3530. https://doi.org/10.1007/s11207-014-0516-8, arXiv:1404.1881.

Hood, A.W., Archontis, V., MacTaggart, D., 2012. 3D MHD flux emergence experiments: idealised models and coronal interactions. SoPh 278, 3–31. https://doi.org/10.1007/s11207-011-9745-2, arXiv:1103.3685.

Hosteaux, S., Chané, E., Decraemer, B., et al., 2018. Ultrahigh-resolution model of a breakout CME embedded in the solar wind. A&A 620, A57. https://doi.org/10.1051/0004-6361/201832976.

Howard, R.A., Vourlidas, A., Bothmer, V., et al., 2019. Near-Sun observations of an F-corona decrease and K-corona fine structure. Natur 576 (7786), 232–236. https://doi.org/10.1038/s41586-019-1807-x.

Hu, Q., Qiu, J., Dasgupta, B., et al., 2014. Structures of interplanetary magnetic flux ropes and comparison with their solar sources. ApJ 793, 53. https://doi.org/10.1088/0004-637X/793/1/53, arXiv:1408.1470.

Illing, R.M.E., Hundhausen, A.J., 1985. Observation of a coronal transient from 1.2 to 6 solar radii. JGR 90 (A1), 275–282. https://doi.org/10.1029/JA090iA01p00275.

Illing, R.M.E., Hundhausen, A.J., 1986. Disruption of a coronal streamer by an eruptive prominence and coronal mass ejection. JGR 91, 10951–10960. https://doi.org/10.1029/JA091iA10p10951.

Iwai, K., Shiota, D., Tokumaru, M., et al., 2019. Development of a coronal mass ejection arrival time forecasting system using interplanetary scintillation observations. Earth, Planets Space 71 (1), 39. https://doi.org/10.1186/s40623-019-1019-5.

Jiang, C., Chen, J., Duan, A. et al., 2021a. Formation of magnetic flux rope during solar eruption. I. Evolution of toroidal flux and reconnection flux. Front. Phys. 9, 575. https://doi.org/10.3389/fphy.2021.746576. arXiv:2109.08422.

Jiang, C., Feng, X., Guo, Y., et al., 2022. Data-driven modeling of solar coronal magnetic field evolution and eruptions. Innovat. 3 (3). https://doi.org/10.1016/j.xinn.2022.100236 100236.

Jiang, C., Feng, X., Liu, R., et al., 2021b. A fundamental mechanism of solar eruption initiation. Nat. Astron. 5, 1126–1138. https://doi.org/10.1038/s41550-021-01414-z, arXiv:2107.08204.

Jing, J., Qiu, J., Lin, J., et al., 2005. Magnetic reconnection rate and flux-rope acceleration of two-ribbon flares. ApJ 620, 1085–1091. https://doi.org/10.1086/427165.

Kaneko, T., Yokoyama, T., 2014. Simulation study of solar plasma eruptions caused by interactions between emerging flux and coronal arcade fields. ApJ 796, 44. https://doi.org/10.1088/0004-637X/796/1/44, arXiv:1410.0189.

Karpen, J.T., Antiochos, S.K., DeVore, C.R., 2012. The mechanisms for the onset and explosive eruption of coronal mass ejections and eruptive flares. ApJ 760, 81. https://doi.org/10.1088/0004-637X/760/1/81.

Kay, C., Opher, M., 2015. The heliocentric distance where the deflections and rotations of solar coronal mass ejections occur. ApJL 811 (2), L36. https://doi.org/10.1088/2041-8205/811/2/L36, arXiv:1509.04948.

Kazachenko, M.D., Fisher, G.H., Welsch, B.T., et al., 2015. Photospheric electric fields and energy fluxes in the eruptive active region NOAA 11158. ApJ 811, 16. https://doi.org/10.1088/0004-637X/811/1/16, arXiv:1505.05974.

Kazachenko, M.D., Lynch, B.J., Welsch, B.T., et al., 2017. A database of flare ribbon properties from the solar dynamics observatory. I. Reconnection flux. ApJ 845, 49. https://doi.org/10.3847/1538-4357/aa7ed6, arXiv:1704.05097.

Kilpua, E.K.J., Good, S.W., Palmerio, E., et al., 2019. Multipoint observations of the june 2012 interacting interplanetary flux ropes. Front. Astron. Space Sci. 6, 50. https://doi.org/10.3389/fspas.2019.00050.

Kilpua, E.K.J., Pomoell, J., Vourlidas, A., et al., 2009. STEREO observations of interplanetary coronal mass ejections and prominence deflection during solar minimum period. AnGeo 27 (12), 4491–4503. https://doi.org/10.5194/angeo-27-4491-2009.

Kleint, L., Battaglia, M., Reardon, K., et al., 2015. The fast filament eruption leading to the X-flare on 2014 March 29. ApJ 806, 9. https://doi.org/10.1088/0004-637X/806/1/9, arXiv:1504.00515.

Kliem, B., Török, T., 2006. Torus instability. Phys. Rev. Lett. 96 (25). https://doi.org/10.1103/PhysRevLett.96.255002, 255002–+. arXiv:arXiv:physics/0605217.

Klimchuk, J.A., 2001. Theory of coronal mass ejections. Geophys. Monogr. Ser. 125, 143. https://doi.org/10.1029/GM125p0143.

Klimchuk, J.A., 2006. On solving the coronal heating problem. SoPh 234, 41–77. https://doi.org/10.1007/s11207-006-0055-z, arXiv:arXiv:astro-ph/0511841.

Knizhnik, K.J., Antiochos, S.K., DeVore, C.R., 2015. Filament channel formation via magnetic helicity condensation. ApJ 809, 137. https://doi.org/10.1088/0004-637X/809/2/137.

Knizhnik, K.J., Antiochos, S.K., DeVore, C.R., 2017a. The role of magnetic helicity in structuring the solar corona. ApJ 835, 85. https://doi.org/10.3847/1538-4357/835/1/85.

Knizhnik, K.J., Antiochos, S.K., DeVore, C.R., et al., 2017b. The mechanism for the energy buildup driving solar eruptive events. ApJL 851, L17. https://doi.org/10.3847/2041-8213/aa9e0a.

Knizhnik, K.J., Antiochos, S.K., Klimchuk, J.A., et al., 2019. The role of magnetic helicity in coronal heating. ApJ 883, 26. https://doi.org/10.3847/1538-4357/ab3afd.

Knizhnik, K.J., Uritsky, V.M., Klimchuk, J.A., et al., 2018. Power-law statistics of driven reconnection in the magnetically closed corona. ApJ 853, 82. https://doi.org/10.3847/1538-4357/aaa0d9.

Korreck, K.E., Szabo, A., Chinchilla, T.N., et al., 2020. Source and propagation of a streamer blowout coronal mass ejection observed by the parker solar probe. ApJS 246 (2), 69. https://doi.org/10.3847/1538-4365/ab6ff9.

Kumar, A., Rust, D.M., 1996. Interplanetary magnetic clouds, helicity conservation, and current-core flux-ropes. JGR 101, 15667–15684. https://doi.org/10.1029/96JA00544.

Kusano, K., Bamba, Y., Yamamoto, T.T., et al., 2012. Magnetic field structures triggering solar flares and coronal mass ejections. ApJ 760, 31. https://doi.org/10.1088/0004-637X/760/1/31.

Lario, D., Balmaceda, L., Alzate, N., et al., 2020. The streamer blowout origin of a flux rope and energetic particle event observed by Parker Solar Probe at 0.5 au. ApJ 897 (2), 134. https://doi.org/10.3847/1538-4357/ab9942.

Leake, J.E., Linton, M.G., Antiochos, S.K., 2014. Simulations of emerging magnetic flux. II. The formation of unstable coronal flux ropes and the initiation of coronal mass ejections. ApJ 787, 46. https://doi.org/10.1088/0004-637X/787/1/46, arXiv:1402.2645.

Leake, J.E., Linton, M.G., Antiochos, S.K., 2022. The role of reconnection in the onset of solar eruptions. ApJ 934 (1), 10. https://doi.org/10.3847/1538-4357/ac74b7, arXiv:2205.12957.

Leake, J.E., Linton, M.G., Török, T., 2013. Simulations of emerging magnetic flux. I. The formation of stable coronal flux ropes. ApJ 778, 99. https://doi.org/10.1088/0004-637X/778/2/99, arXiv:1308.6204.

Lepping, R.P., Burlaga, L.F., Jones, J.A., 1990. Magnetic field structure of interplanetary magnetic clouds at 1 AU. JGR 95, 11957–11965. https://doi.org/10.1029/JA095iA08p11957.

Liewer, P.C., Qiu, J., Vourlidas, A., et al., 2021. Evolution of a streamer-blowout CME as observed by imagers on Parker Solar Probe and the Solar Terrestrial Relations Observatory. A&A 650, A32. https://doi.org/10.1051/0004-6361/202039641, arXiv:2012.05174.

Lin, J., Forbes, T.G., Isenberg, P.A., 2001. Prominence eruptions and coronal mass ejections triggered by newly emerging flux. JGR 106, 25053–25074. https://doi.org/10.1029/2001JA000046.

Linker, J.A., Mikić, Z., Lionello, R., et al., 2003. Flux cancellation and coronal mass ejections. Phys. Plasmas 10, 1971–1978. https://doi.org/10.1063/1.1563668.

Linton, M.G., Dahlburg, R.B., Antiochos, S.K., 2001. Reconnection of twisted flux tubes as a function of contact angle. ApJ 553 (2), 905–921. https://doi.org/10.1086/320974.

Lionello, R., Downs, C., Linker, J.A., et al., 2013. Magnetohydrodynamic simulations of interplanetary coronal mass ejections. ApJ 777 (1), 76. https://doi.org/10.1088/0004-637X/777/1/76.

Lionello, R., Linker, J.A., Mikić, Z., 2009. Multispectral emission of the sun during the first whole sun month: Magnetohydrodynamic simulations. ApJ 690 (1), 902–912. https://doi.org/10.1088/0004-637X/690/1/902.

Lionello, R., Török, T., Titov, V.S., et al., 2016. The contribution of coronal jets to the solar wind. ApJL 831, L2. https://doi.org/10.3847/2041-8205/831/1/L2.

Liu, Y., Sun, X., Török, T., et al., 2017. Electric-current neutralization, magnetic shear, and eruptive activity in solar active regions. ApJL 846, id. L6. https://doi.org/10.3847/2041-8213/aa861e.

Liu, Y., Welsch, B.T., Valori, G., et al., 2023. Changes of magnetic energy and helicity in solar active regions from major flares. ApJ 942 (1), 27. https://doi.org/10.3847/1538-4357/aca3a6.

Louis, R.E., Kliem, B., Ravindra, B., et al., 2015. Triggering an eruptive flare by emerging flux in a solar active-region complex. SoPh 290, 3641–3662. https://doi.org/10.1007/s11207-015-0726-8, arXiv:1506.08035.

Low, B.C., 2001. Coronal mass ejections, magnetic flux ropes, and solar magnetism. JGR 106, 25141–25164. https://doi.org/10.1029/2000JA004015.

Low, B.C., 2002. Magnetic coupling between the corona and the solar dynamo. In: ESA SP-505: SOLMAG 2002. Proceedings of the Magnetic Coupling of the Solar Atmosphere Euroconference, pp. 35–+.

Lumme, E., Kazachenko, M.D., Fisher, G.H., et al., 2019. Probing the effect of cadence on the estimates of photospheric energy and helicity injections in eruptive active region NOAA AR 11158. SoPh 294 (6), 84. https://doi.org/10.1007/s11207-019-1475-x, arXiv:1907.00367.

Lundquist, S., 1950. Magnetohydrostatic fields. Ark. Fys. 2, 361.

Lynch, B.J., 2020. A model for coronal inflows and in/out pairs. ApJ 905 (2), 139. https://doi.org/10.3847/1538-4357/abc5b3, arXiv:2010.13959.

Lynch, B.J., Airapetian, V.S., DeVore, C.R., et al., 2019. Modeling a carrington-scale stellar superflare and coronal mass ejection from $\kappa^1 Cet$. ApJ 880 (2), 97. https://doi.org/10.3847/1538-4357/ab287e, arXiv:1906.03189.

Lynch, B.J., Al-Haddad, N., Yu, W., et al., 2022. On the utility of flux rope models for CME magnetic structure below 30 Rs. AdSpR 70 (6), 1614–1640. https://doi.org/10.1016/j.asr.2022.05.004, arXiv:2205.02144.

Lynch, B.J., Antiochos, S.K., DeVore, C.R., et al., 2008. Topological evolution of a fast magnetic breakout CME in three dimensions. ApJ 683, 1192–1206. https://doi.org/10.1086/589738.

Lynch, B.J., Antiochos, S.K., Li, Y., et al., 2009. Rotation of coronal mass ejections during eruption. ApJ 697, 1918–1927. https://doi.org/10.1088/0004-637X/697/2/1918.

Lynch, B.J., Antiochos, S.K., MacNeice, P.J., et al., 2004. Observable properties of the breakout model for coronal mass ejections. ApJ 617, 589–599. https://doi.org/10.1086/424564.

Lynch, B.J., Edmondson, J.K., 2013. Sympathetic magnetic breakout coronal mass ejections from pseudostreamers. ApJ 764, 87. https://doi.org/10.1088/0004-637X/764/1/87, arXiv:1212.6677.

Lynch, B.J., Masson, S., Li, Y., et al., 2016. A model for stealth coronal mass ejections. JGR 121 (11), 10677–10697. https://doi.org/10.1002/2016JA023432, arXiv:1612.08323.

Lynch, B.J., Palmerio, E., DeVore, C.R., et al., 2021. Modeling a coronal mass ejection from an extended filament channel. I. Eruption and early evolution. ApJ 914 (1), 39. https://doi.org/10.3847/1538-4357/abf9a9, arXiv:2104.08643.

Mackay, D.H., DeVore, C.R., Antiochos, S.K., 2014. Global-scale consequences of magnetic-helicity injection and condensation on the sun. ApJ 784, 164. https://doi.org/10.1088/0004-637X/784/2/164.

Mackay, D.H., DeVore, C.R., Antiochos, S.K., et al., 2018. Magnetic helicity condensation and the solar cycle. ApJ 869, 62. https://doi.org/10.3847/1538-4357/aaec7c.

Mackay, D.H., van Ballegooijen, A.A., 2006. Models of the large-scale corona. I. Formation, evolution, and liftoff of magnetic flux ropes. ApJ 641, 577–589. https://doi.org/10.1086/500425.

Mackay, D.H., Yeates, A.R., 2012. The Sun's global photospheric and coronal magnetic fields: observations and models. Living Rev. Sol. Phys. 9 (1), 6. https://doi.org/10.12942/lrsp-2012-6, arXiv:1211.6545.

MacNeice, P., Antiochos, S.K., Phillips, A., et al., 2004. A numerical study of the breakout model for coronal mass ejection initiation. ApJ 614, 1028–1041. https://doi.org/10.1086/423887.

MacTaggart, D., Hood, A.W., 2009. On the emergence of toroidal flux tubes: general dynamics and comparisons with the cylinder model. A&A 507, 995–1004. https://doi.org/10.1051/0004-6361/200912930, arXiv:0909.3987.

Manchester IV, W., Gombosi, T., DeZeeuw, D., et al., 2004. Eruption of a buoyantly emerging magnetic flux rope. ApJ 610, 588–596. https://doi.org/10.1086/421516.

Masson, S., Antiochos, S.K., DeVore, C.R., 2013. A model for the escape of solar-flare-accelerated particles. ApJ 771, 82. https://doi.org/10.1088/0004-637X/771/2/82.

Masson, S., Antiochos, S.K., DeVore, C.R., 2019. Escape of flare-accelerated particles in solar eruptive events. ApJ 884, 143. https://doi.org/10.3847/1538-4357/ab4515.

McComas, D.J., Gosling, J.T., Hammond, C.M., et al., 1994. Magnetic reconnection ahead of a coronal mass ejection. GRL 21 (17), 1751–1754. https://doi.org/10.1029/94GL01077.

McGregor, S.L., Hughes, W.J., Arge, C.N., et al., 2008. Analysis of the magnetic field discontinuity at the potential field source surface and schatten current sheet interface in the wang-sheeley-arge model. JGR 113, A08112. https://doi.org/10.1029/2007JA012330.

Metcalf, T.R., Leka, K.D., Barnes, G., et al., 2006. An overview of existing algorithms for resolving the 180° ambiguity in vector magnetic fields: quantitative tests with synthetic data. SoPh 237, 267–296. https://doi.org/10.1007/s11207-006-0170-x.

Mikić, Z., Linker, J.A., Schnack, D.D., et al., 1999. Magnetohydrodynamic modeling of the global solar corona. Phys. Plasmas 6, 2217–2224. https://doi.org/10.1063/1.873474.

Moore, R.L., Sterling, A.C., Hudson, H.S., et al., 2001. Onset of the magnetic explosion in solar flares and coronal mass ejections. ApJ 552, 833–848. https://doi.org/10.1086/320559.

Moreno-Insertis, F., Galsgaard, K., 2013. Plasma jets and eruptions in solar coronal holes: a three-dimensional flux emergence experiment. ApJ 771 (1), 20. https://doi.org/10.1088/0004-637X/771/1/20, arXiv:1305.2201.

Möstl, C., Farrugia, C.J., Biernat, H.K., et al., 2009. Optimized Grad - Shafranov reconstruction of a magnetic cloud using STEREO- wind observations. SoPh 256 (1–2), 427–441. https://doi.org/10.1007/s11207-009-9360-7.

Möstl, C., Weiss, A.J., Reiss, M.A., et al., 2022. Multipoint interplanetary coronal mass ejections observed with solar orbiter, BepiColombo, Parker Solar Probe, Wind, and STEREO-A. ApJL 924 (1), L6. https://doi.org/10.3847/2041-8213/ac42d0, arXiv:2109.07200.

Müller, D., St. Cyr, O.C., Zouganelis, I., et al., 2020. The Solar Orbiter mission. Science overview. A&A 642, A1. https://doi.org/10.1051/0004-6361/202038467, arXiv:2009.00861.

Mulligan, T., Reinard, A.A., Lynch, B.J., 2013. Advancing in situ modeling of ICMEs: New techniques for new observations. JGR 118 (4), 1410–1427. https://doi.org/10.1002/jgra.50101, arXiv:1208.5107.

Nieves-Chinchilla, T., Linton, M.G., Hidalgo, M.A., et al., 2018. Elliptic-cylindrical analytical flux rope model for magnetic clouds. ApJ 861 (2), 139. https://doi.org/10.3847/1538-4357/aac951.

Nieves-Chinchilla, T., Linton, M.G., Hidalgo, M.A., et al., 2016. A Circular-cylindrical Flux-rope Analytical Model for Magnetic Clouds. ApJ 823 (1), 27. https://doi.org/10.3847/0004-637X/823/1/27.

Nieves-Chinchilla, T., Szabo, A., Korreck, K.E., et al., 2020. Analysis of the internal structure of the streamer blowout observed by the Parker Solar Probe during the first solar encounter. ApJS 246 (2), 63. https://doi.org/10.3847/1538-4365/ab61f5.

Nindos, A., Zhang, J., Zhang, H., 2003. The magnetic helicity budget of solar active regions and coronal mass ejections. ApJ 594, 1033–1048. https://doi.org/10.1086/377126.

Notoya, S., Yokoyama, T., Kusano, K. et al., 2007. Three-Dimensional Filament Eruption Driven by an Emerging Flux. In: Shibata, K., Nagata, S., Sakurai T. (Eds.), New Solar Physics with Solar-B Mission, volume 369 of Astronomical Society of the Pacific Conference Series, p. 381.

Olsen, N., Glassmeier, K.H., Jia, X., 2010. Separation of the magnetic field into external and internal parts. SSRv 152 (1–4), 135–157. https://doi.org/10.1007/s11214-009-9563-0.

Owens, M.J., Nichols, J.D., 2021. Using in situ solar-wind observations to generate inner-boundary conditions to outer-heliosphere simulations - i. dynamic time warping applied to synthetic observations. MNRAS 508, 2575–2582. https://doi.org/10.1093/mnras/sTable 2512.

Pal, S., Dash, S., Nandy, D., 2020. Flux erosion of magnetic clouds by reconnection with the Sun's open flux. GRL 47 (8). https://doi.org/10.1029/2019GL086372, arXiv:2103.05990 e86372.

Pal, S., Lynch, B.J., Good, S.W., et al., 2022. Eruption and interplanetary evolution of a stealthy streamer-blowout CME observed by PSP at ∼0.5 AU. FrASS 9. https://doi.org/10.3389/fspas.2022.903676 903676.

Palmerio, E., Kay, C., Al-Haddad, N. et al., 2021a. Predicting the Magnetic Fields of a Stealth CME Detected by Parker Solar Probe at 0.5 au. ApJ, 920(2), 65. https://doi.org/10.3847/1538-4357/ac25f4. arXiv:2109.04933.

Palmerio, E., Kilpua, E.K.J., James, A.W., et al., 2017. Determining the intrinsic CME flux rope type using remote-sensing solar disk observations. SoPh 292, 39. https://doi.org/10.1007/s11207-017-1063-x, arXiv:1701.08595.

Palmerio, E., Lee, C.O., Mays, M.L. et al., 2022a. CMEs and SEPs During November-December 2020: a challenge for real-time space weather forecasting. Space Weather, 20(5), e2021SW002993. https://doi.org/10.1029/2021SW002993. arXiv:2203.16433.

Palmerio, E., Lee, C.O., Richardson, I.G. et al., 2022b. CME evolution in the structured heliosphere and effects at earth and mars during solar minimum. Space Weather, 20(9), e2022SW003215. https://doi.org/10.1029/2022SW003215. arXiv:2209.05760.

Palmerio, E., Nieves-Chinchilla, T., Kilpua, E.K.J. et al., 2021b. Magnetic structure and propagation of two interacting CMEs from the sun to saturn. JGR, 126(11), e2021JA029770. https://doi.org/10.1029/2021JA029770. arXiv:2110.02190.

Panasenco, O., Martin, S.F., Velli, M., et al., 2013. Origins of rolling, twisting, and non-radial propagation of eruptive solar events. SoPh 287 (1–2), 391–413. https://doi.org/10.1007/s11207-012-0194-3, arXiv:1211.1376.

Parenti, S., Chifu, I., Del Zanna, G., et al., 2021. Linking the Sun to the heliosphere using composition data and modelling. SSRv 217 (8), 78. https://doi.org/10.1007/s11214-021-00856-1, arXiv:2110.06111.

Parker, E.N., 1987. Stimulated dissipation of magnetic discontinuities and the origin of solar flares. SoPh 111, 297–308. https://doi.org/10.1007/BF00148522.

Patsourakos, S., Vourlidas, A., Török, T., et al., 2020. Decoding the pre-eruptive magnetic field configurations of coronal mass ejections. SSRv 216, 131. https://doi.org/10.1007/s11214-020-00757-9.

Perri, B., Leitner, P., Brchnelova, M., et al., 2022. COCONUT, a novel fast-converging MHD model for solar corona simulations: I. Benchmarking and optimization of polytropic solutions. ApJ 936 (1), 19. https://doi.org/10.3847/1538-4357/ac7237, arXiv:2205.03341.

Pesnell, W.D., Thompson, B.J., Chamberlin, P.C., 2012. The Solar Dynamics Observatory (SDO). SoPh 275, 3–15. https://doi.org/10.1007/s11207-011-9841-3.

Pontin, D.I., Priest, E.R., 2022. Magnetic reconnection: MHD theory and modelling. Living Rev. Sol. Phys. 19 (1), 1. https://doi.org/10.1007/s41116-022-00032-9.

Priest, E.R., Longcope, D.W., 2017. Flux-rope twist in eruptive flares and CMEs: due to zipper and main-phase reconnection. SoPh 292, 25. https://doi.org/10.1007/s11207-016-1049-0, arXiv:1701.00147.

Priest, E.R., Longcope, D.W., 2020. The creation of twist by reconnection of flux tubes. SoPh 295 (3), 48. https://doi.org/10.1007/s11207-020-01608-0.

Qiu, J., Hu, Q., Howard, T.A., et al., 2007. On the magnetic flux budget in low-corona magnetic reconnection and interplanetary coronal mass ejections. ApJ 659, 758–772. https://doi.org/10.1086/512060.

Qiu, J., Liu, W., Hill, N., et al., 2010. Reconnection and energetics in two-ribbon flares: a revisit of the bastille-day flare. ApJ 725, 319–330. https://doi.org/10.1088/0004-637X/725/1/319.

Rast, M.P., Bello González, N., Bellot Rubio, L., et al., 2021. Critical science plan for the Daniel K. Inouye Solar Telescope (DKIST). SoPh 296 (4), 70. https://doi.org/10.1007/s11207-021-01789-2, arXiv:2008.08203.

Riley, P., Linker, J.A., Lionello, R., et al., 2012. Corotating interaction regions during the recent solar minimum: The power and limitations of global MHD modeling. J. Atmos. Solar Terr. Phys. 83, 1–10. https://doi.org/10.1016/j.jastp.2011.12.013.

Ruffenach, A., Lavraud, B., Farrugia, C.J., et al., 2015. Statistical study of magnetic cloud erosion by magnetic reconnection. JGR 120 (1), 43–60. https://doi.org/10.1002/2014JA020628.

Salman, T.M., Winslow, R.M., Lugaz, N., 2020. Radial evolution of coronal mass ejections between MESSENGER, Venus Express, STEREO, and L1: catalog and analysis. JGR 125 (1). https://doi.org/10.1029/2019JA027084, arXiv:1912.11731 e27084.

Samara, E., Laperre, B., Kieokaew, R., et al., 2022. Dynamic time warping as a means of assessing solar wind time series. ApJ 927, 187. https://doi.org/10.3847/1538-4357/ac4af6.

Scherrer, P.H., Schou, J., Bush, R.I., et al., 2012. The Helioseismic and Magnetic Imager (HMI) Investigation for the Solar Dynamics Observatory (SDO). SoPh 275, 207–227. https://doi.org/10.1007/s11207-011-9834-2.

Schou, J., Scherrer, P.H., Bush, R.I., et al., 2012. Design and Ground Calibration of the Helioseismic and Magnetic Imager (HMI) Instrument on the Solar Dynamics Observatory (SDO). SoPh 275, 229–259. https://doi.org/10.1007/s11207-011-9842-2.

Schrijver, C.J., 2001. Simulations of the photospheric magnetic activity and outer atmospheric radiative losses of cool stars based on characteristics of the solar magnetic field. ApJ 547 (1), 475–490. https://doi.org/10.1086/318333.

Schrijver, C.J., 2007. A characteristic magnetic field pattern associated with all major solar flares and its use in flare forecasting. ApJL 655, L117–L120. https://doi.org/10.1086/511857.

Schrijver, C.J., 2009. Driving major solar flares and eruptions: A review. Adv. Space Res. 43, 739–755. https://doi.org/10.1016/j.asr.2008.11.004, arXiv:0811.0787.

Schrijver, C.J., Aulanier, G., Title, A.M., et al., 2011. The 2011 February 15 X2 Flare, ribbons, coronal front, and mass ejection: interpreting the three-dimensional views from the solar dynamics observatory and STEREO Guided by magnetohydrodynamic flux-rope modeling. ApJ 738 (2), 167. https://doi.org/10.1088/0004-637X/738/2/167.

Schrijver, C.J., De Rosa, M.L., Metcalf, T., et al., 2008. Nonlinear force-free field modeling of a solar active region around the time of a major flare and coronal mass ejection. ApJ 675, 1637–1644. https://doi.org/10.1086/527413, arXiv:0712.0023.

Schrijver, C.J., Title, A.M., Yeates, A.R., et al., 2013. Pathways of large-scale magnetic couplings between solar coronal events. ApJ 773, 93. https://doi.org/10.1088/0004-637X/773/2/93, arXiv:1305.0801.

Schuck, P.W., 2008. Tracking vector magnetograms with the magnetic induction equation. ApJ 683, 1134–1152. https://doi.org/10.1086/589434.

Schuck, P.W., Linton, M.G., Knizhnik, K.J., et al., 2022. On the origin of the photospheric magnetic field. ApJ 936 (1), 94. https://doi.org/10.3847/1538-4357/ac739a.

Scolini, C., Rodriguez, L., Mierla, M., et al., 2019. Observation-based modelling of magnetised coronal mass ejections with EUHFORIA. A&A 626, A122. https://doi.org/10.1051/0004-6361/201935053, arXiv:1904.07059.

Scolini, C., Winslow, R.M., Lugaz, N., et al., 2023. Characteristic scales of complexity and coherence within interplanetary coronal mass ejections: insights from spacecraft swarms in global heliospheric simulations. ApJ 944 (1), 46. https://doi.org/10.3847/1538-4357/aca893, arXiv:2212.01308.

Scolini, C., Winslow, R.M., Lugaz, N., et al., 2022. Causes and consequences of magnetic complexity changes within interplanetary coronal mass ejections: a statistical study. ApJ 927 (1), 102. https://doi.org/10.3847/1538-4357/ac3e60, arXiv:2111.12637.

Sheeley, N.R., Walters, J.H., Wang, Y.M., et al., 1999. Continuous tracking of coronal outflows: Two kinds of coronal mass ejections. JGR 104 (A11), 24739–24768. https://doi.org/10.1029/1999JA900308.

Shen, C., Wang, Y., Gui, B., et al., 2011. Kinematic evolution of a slow CME in corona viewed by STEREO-B on 8 October 2007. SoPh 269 (2), 389–400. https://doi.org/10.1007/s11207-011-9715-8, arXiv:1101.3205.

Sonnerup, B.U.O., Cahill, J., L.J., 1967. Magnetopause structure and attitude from explorer 12 observations. JGR, 72, 171. https://doi.org/10.1029/JZ072i001p00171.

Sturrock, P.A., 1991. Maximum energy of semi-infinite magnetic field configurations. ApJ 380, 655. https://doi.org/10.1086/170620.

Sun, X., Hoeksema, J.T., Liu, Y., et al., 2012a. Evolution of magnetic field and energy in a major eruptive active region based on SDO/HMI observation. ApJ 748, 77. https://doi.org/10.1088/0004-637X/748/2/77, arXiv:1201.3404.

Sun, X., Hoeksema, J.T., Liu, Y., et al., 2012b. Evolution of magnetic field and energy in a major eruptive active region based on SDO/HMI observation. ApJ 748 (2), 77. https://doi.org/10.1088/0004-637X/748/2/77, arXiv:1201.3404.

Syntelis, P., Archontis, V., Tsinganos, K., 2017. Recurrent CME-like eruptions in emerging flux regions. I. On the mechanism of eruptions. ApJ 850, 95. https://doi.org/10.3847/1538-4357/aa9612, arXiv:1711.10249.

Temmer, M., Scolini, C., Richardson, I.G., et al., 2023. CME propagation through the ambient solar wind: status and future of observations and model development. Adv. Space Res. (submitted)

Thalmann, J.K., Georgoulis, M.K., Liu, Y., et al., 2021. Magnetic helicity estimations in models and observations of the solar magnetic field. IV. Application to solar observations. ApJ 922 (1), 41. https://doi.org/10.3847/1538-4357/ac1f93, arXiv:2108.08525.

Thernisien, A.F.R., Howard, R.A., Vourlidas, A., 2006. Modeling of flux rope coronal mass ejections. ApJ 652 (1), 763–773. https://doi.org/10.1086/508254.

Titov, V.S., 2007. Generalized squashing factors for covariant description of magnetic connectivity in the solar corona. Astrophys. J. 660, 863. https://doi.org/10.1086/512671.

Titov, V.S., Mikic, Z., Linker, J.A., et al., 2011. Magnetic topology of coronal hole linkages. Astrophys. J. 731, 111. https://doi.org/10.1088/0004-637X/731/2/111.

Titov, V.S., Török, T., Mikic, Z., et al., 2014. A method for embedding circular force-free flux ropes in potential magnetic fields. ApJ 790, 163. https://doi.org/10.1088/0004-637X/790/2/163.

Török, E., T, Linton, M.G., Leake, J.E. et al., 2023. Solar Eruptions Triggered by Flux Emergence. ApJ, in review.

Török, T., Downs, C., Linker, J.A., Lionello, R., Titov, V.S., Mikić, Z., Riley, P., Caplan, R.M., Wijaya, J., 2018. Sun-to-Earth MHD Simulation of the 2000 July 14 "Bastille Day" Eruption. ApJ 856 (1), 75. https://doi.org/10.3847/1538-4357/aab36d.

Török, T., Lionello, R., Titov, V.S. et al., 2016. Modeling Jets in the Corona and Solar Wind. In: Dorotovic, I, Fischer, C.E., Temmer, M. (Eds.), Coimbra Solar Physics Meeting: Ground-based Solar Observations in the Space Instrumentation Era, volume 504 of Astronomical Society of the Pacific Conference Series, p. 185.

Török, T., Panasenco, O., Titov, V.S., et al., 2011. A model for magnetically coupled sympathetic eruptions. ApJL 739, L63. https://doi.org/10.1088/2041-8205/739/2/L63, arXiv:1108.2069.

Valori, G., Pariat, E., Anfinogentov, S., et al., 2016. Magnetic helicity estimations in models and observations of the solar magnetic field. Part I: finite volume methods. SSRv 201 (1–4), 147–200. https://doi.org/10.1007/s11214-016-0299-3, arXiv:1610.02193.

van Ballegooijen, A.A., 2004. Observations and modeling of a filament on the Sun. ApJ 612, 519–529. https://doi.org/10.1086/422512.

van Ballegooijen, A.A., Priest, E.R., Mackay, D.H., 2000. Mean field model for the formation of filament channels on the Sun. ApJ 539, 983–994. https://doi.org/10.1086/309265.

van der Holst, B., Manchester, I., W., Sokolov, I.V. et al., 2009. Breakout coronal mass ejection or streamer blowout: the bugle effect. ApJ, 693 (2), 1178–1187. https://doi.org/10.1088/0004-637X/693/2/1178.

Velli, M., Harra, L.K., Vourlidas, A., et al., 2020. Understanding the origins of the heliosphere: integrating observations and measurements from Parker Solar Probe, Solar Orbiter, and other space- and ground-based observatories. A&A 642, A4. https://doi.org/10.1051/0004-6361/202038245.

Verbeke, C., Mays, L., Kay, C. et al., 2022. Quantifying errors in 3d cme parameters derived from synthetic data using white-light reconstruction techniques. Adv. Space Res. https://doi.org/10.1016/j.asr.2022.08.056 (in press).

Vourlidas, A., Lynch, B.J., Howard, R.A., et al., 2013. How Many CMEs Have Flux Ropes? Deciphering the signatures of shocks, flux ropes, and prominences in coronagraph observations of CMEs. SoPh 284, 179–201. https://doi.org/10.1007/s11207-012-0084-8, arXiv:1207.1599.

Vršnak, B., Amerstorfer, T., Dumbović, M., et al., 2019. Heliospheric evolution of magnetic clouds. ApJ 877 (2), 77. https://doi.org/10.3847/1538-4357/ab190a, arXiv:1904.08266.

Wang, H., Liu, C., 2010. Observational evidence of back reaction on the solar surface associated with coronal magnetic restructuring in solar eruptions. ApJL 716, L195–L199. https://doi.org/10.1088/2041-8205/716/2/L195, arXiv:1005.4137.

Wang, J., Liu, S., Luo, B., 2022. Analyzing deflection of multiple solar coronal mass ejections from the same active region. Adv. Space Res. https://doi.org/10.1016/j.asr.2022.06.017 (in press).

Wang, Y.-M., Sheeley Jr., N.R., 1995. Solar implications of ulysses interplanetary field measurements. ApJ 447, L143. https://doi.org/10.1086/309578.

Warnecke, J., Peter, H., 2019. Data-driven model of the solar corona above an active region. A&A 624, L12. https://doi.org/10.1051/0004-6361/201935385, arXiv:1903.00455.

Weiss, A.J., Nieves-Chinchilla, T., Möstl, C., et al., 2022. Writhed analytical magnetic flux rope model. JGR 127 (12). https://doi.org/10.1029/2022JA030898, arXiv:2202.10096 e2022JA030898.

Welsch, B.T., 2018. Flux accretion and coronal mass ejection dynamics. SoPh 293, 113. https://doi.org/10.1007/s11207-018-1329-y.

Welsch, B.T., Fisher, G.H., Sun, X., 2013. A magnetic calibration of photospheric doppler velocities. ApJ 765, 98. https://doi.org/10.1088/0004-637X/765/2/98, arXiv:1201.2451.

Welsch, B.T., Kusano, K., Yamamoto, T.T., et al., 2012. Decorrelation times of photospheric fields and flows. ApJ 747 (2), 130. https://doi.org/10.1088/0004-637X/747/2/130, arXiv:1110.6117.

Wiegelmann, T., 2007. Computing nonlinear force-free coronal magnetic fields in spherical geometry. SoPh 240 (2), 227–239. https://doi.org/10.1007/s11207-006-0266-3, arXiv:astro-ph/0612124.

Williams, D.R., Török, T., Démoulin, P., et al., 2005. Eruption of a Kink-unstable Filament in NOAA Active Region 10696. ApJL 628, L163–L166. https://doi.org/10.1086/432910, arXiv:arXiv:astro-ph/0507661.

Winslow, R.M., Lugaz, N., Philpott, L.C., et al., 2015. Interplanetary coronal mass ejections from MESSENGER orbital observations at Mercury. JGR 120 (8), 6101–6118. https://doi.org/10.1002/2015JA021200.

Wood, B.E., Hess, P., Howard, R.A., et al., 2020. Morphological reconstruction of a small transient observed by Parker solar probe on 2018 November 5. ApJS 246 (2), 28. https://doi.org/10.3847/1538-4365/ab5219, arXiv:2001.08716.

Wyper, P.F., Antiochos, S.K., DeVore, C.R., 2017. A universal model for solar eruptions. Natur 544, 452–455. https://doi.org/10.1038/nature22050.

Xu, X.-Y., Fang, C., Chen, P.-F., 2008. A statistical study on the filament eruption caused by new emerging flux. ChA&A 32, 56–64. https://doi.org/10.1016/j.chinastron.2008.01.008.

Yan, X., Xue, Z., Jiang, C., et al., 2022. Fast plasmoid-mediated reconnection in a solar flare. Nat. Commun. 13, 640. https://doi.org/10.1038/s41467-022-28269-w.

Zhang, Y., Zhang, M., Zhang, H., 2008. On the relationship between flux emergence and CME Initiation. SoPh 250, 75–88. https://doi.org/10.1007/s11207-008-9150-7.

Zhao, L., DeVore, C.R., Antiochos, S.K., et al., 2015. Numerical simulations of helicity condensation in the solar corona. ApJ 805, 61. https://doi.org/10.1088/0004-637X/805/1/61.

Zheng, R., Chen, Y., Wang, B., 2020. The initiation of a solar streamer blowout coronal mass ejection arising from the streamer flank. ApJL 897 (2), L21. https://doi.org/10.3847/2041-8213/ab9ebd, arXiv:2007.00896.

Zuccarello, F.P., Soenen, A., Poedts, S., et al., 2008. Initiation of coronal mass ejections by magnetic flux emergence in the framework of the breakout model. ApJL 689, L157–L160. https://doi.org/10.1086/595821.